Report
R-21-17
March 2022

Evaluation and modelling report of Task 9D regarding safety assessment calculations based on gained knowledge within Task 9

Task 9 of SKB Task Force GWFTS – Increasing the realism in solute transport modelling based on the field experiments REPRO and LTDE-SD

James Crawford
Josep M Soler
Paolo Trinchero
Milan Hokr
Václava Havlová
Aleš Vetešník
Libor Gvoždík
Martin Milický
Michal Polák
Dan Reimitz
Jakub Říha
Dagmar Trpkošová
Jakub Višňák
Dušan Vopálka
Shuo Meng
Luis Moreno
Longcheng Liu
Urban Svensson

SVENSK KÄRNBRÄNSLEHANTERING AB

SWEDISH NUCLEAR FUEL
AND WASTE MANAGEMENT CO

Box 3091, SE-169 03 Solna
Phone +46 8 459 84 00
skb.se

SVENSK KÄRNBRÄNSLEHANTERING

ISSN 1402-3091
SKB R-21-17
ID 1956867
March 2022

Evaluation and modelling report of Task 9D regarding safety assessment calculations based on gained knowledge within Task 9

Task 9 of SKB Task Force GWFTS – Increasing the realism in solute transport modelling based on the field experiments REPRO and LTDE-SD

James Crawford[1], Josep M Soler[2], Paolo Trinchero[3], Milan Hokr[4], Václava Havlová[5], Aleš Vetešník[6], Libor Gvoždík[7], Martin Milický[7], Michal Polák[7], Dan Reimitz[6], Jakub Říha[4], Dagmar Trpkošová[5], Jakub Višňák[6], Dušan Vopálka[6], Shuo Meng[8], Luis Moreno[8], Longcheng Liu[8], Urban Svensson[9]

1 Kemakta Konsult AB
2 IDAEA-CSIC
3 Amphos 21 Consulting S.L.
4 Technical University of Liberec
5 ÚJV Řež
6 Czech Technical University in Prague
7 PROGEO
8 Royal Institute of Technology, KTH
9 CFE AB

Keywords: Safety Assessment, Solute transport, Modelling, Upscaling.

Abstract

Task 9D is the fourth and final subtask of Task Force GWFTS Task 9. The focus in this subtask was extrapolating results from in situ experimental conditions to something more closely resembling a typical Safety Assessment (SA) scenario. The main aim was to establish whether information obtained in the detailed scale modelling work performed in the first three subtasks 9A-C could provide useful input to modelling over much larger spatial and temporal scales. Specifically, the consequences of including, or neglecting detailed scale heterogeneity for modelling increasingly large spatial domains and longer time scales was sought. Although the option of using the same tools and modelling approaches was left open, the intention was for the participating modelling groups to identify whether features and complexities important for detailed scale modelling become less important or average out at larger scales and if simplification of modelling approaches was possible. The modelling group submissions represent a diverse range of approaches and interpretations of the task description. Some of the modelling groups elected to use similar tools and methods as used in the previous subtasks, while others chose completely novel approaches. Not all groups were able to produce results for the specified tracers and in some cases, the consequences of material property heterogeneity for scale-up to Safety Assessment relevant path lengths and temporal scales was difficult to quantify in a non-trivial manner. Although the overall aims of the Task 9D were not fully achieved, some key lessons were learned that point towards how future modelling efforts of this kind may be better formulated to maximise scientific value.

Sammanfattning

Task 9D är den fjärde och sista delmomentet av Task Force GWTFS Task 9. I fokus för denna Task var extrapolation av resultat från experimentella försök till en approximation av ett typiskt säkerhetsanalysliknande (SA) scenario. Målet med detta var att undersöka om informationen som erhölls under de första tre delmoment Task 9A-C kunde utgöra användbart underlag till modellering på större spatial- och tidsskala. Mer specifikt var konsekvenserna av att inkludera eller inte inkludera beskrivningar av heterogenitet på en detaljerade skala eftersökt. Intentionen var att modelleringsgrupperna själv skulle identifiera huruvida de attribut och processer som är viktiga för småskalig modellering blir mindre viktiga eller jämnas ut till ett medelvärde på större avstånd samt om förenklingar var möjliga även om möjligheten att använda sig av samma beräkningsverktyg från tidigare delmoment var tillåtet. Bidragen från modelleringsgrupperna representerade ett mångfacetterat sortiment av angreppssätt och tolkningar av uppgiftsbeskrivningen. Vissa grupper valde att använda samma eller liknande metodik som tidigare medan andra valde helt nya angreppssätt. Inte alla grupper klarade att leverera resultat för samtliga spårämnen som specificerades och i vissa fall var uppskalningen till säkerhetsanalysrelevanta transportskalor svåra att genomföra. Även om huvudmålen med Task 9D inte blev helt uppfyllda erhölls viktiga erfarenheter som kan vägleda till hur liknande och framtida modelleringsförsök bör utformas.

Contents

1 Introduction

Task 9D is the fourth sub-task of the Task Force GWTFS Task 9, where the focus is upon adapting modelling techniques developed previously in Tasks 9A, 9B and 9C to a setting more closely resembling that of a typical Safety Assessment (SA) scenario. Previous sub-tasks produced very complex, pore-scale descriptions of heterogeneity; the principle aim of this sub-task was to investigate how these could be scaled up such that they could be practically used in SA calculations involving long distance transport of migrating radionuclides in the geosphere. A secondary aim of Task 9D was to estimate the effective retention properties of the upscaled system, in order to identify how the complex dynamics modelled on very small scales in Tasks 9A, B, and C are averaged over much larger spatial scales. A related question is whether processes identified as being of great importance for reproducing details of experimental data in small scale in situ (or lab-) experiments are associated with greater or lesser prominence over increasingly large transport distances.

The main scientific questions and objectives of Task 9D can be summarised as follows:

1) How do we condense complex site characterisation models down to something practically useable for SA modelling? (Is it possible on much larger spatial and temporal scales?);
2) How do the more complex behaviours observed in experiments scale to SA conditions and timescales? (i.e., do they "vanish" or become less prominent?);
3) What are the consequences of neglecting microstructural heterogeneity for the Safety Case (confidence building)?

The Task 9D modelling teams were afforded a great deal of flexibility in defining how the different case studies were to be carried out, as it was considered important that the instructions did not introduce bias in favour of particular modelling approaches or types of heterogeneity. However, this makes comparing results obtained by the different modelling groups difficult.

1.1 Overview of Task 9D

The following paragraphs provide a short overview of the main features of Task 9D (the task description is set out in detail in Appendix 5. The primary idea was to take the annular flowpath modelled in Task 9A WPDE (Water Phase Diffusion Experiment) experiments (cf Figure 1-1) and unwrap and extend it to a total length of 1 000 m, while preserving the cross-sectional area of the annulus and specific flow-wetted surface (m^2/m) of the experimental section. The F-factor (hydrodynamic transport resistance) for the SA scenario was specified as 5×10^4 y/m, implying a flow, q (m^3/y) reduction of about a factor of 3 relative to the WDPE-1 experiment and a factor of 1.5 relative to the WPDE-2 experiment. The unwrapped and extended flowpath for the SA scenario was a flow channel of roughly 8.87 cm width, with an average transport aperture of 2.45 mm.

The sub-task was divided into several steps of increasing complexity, as outlined in Table 1-1. The first stages of Task 9D-1 (1a and 1b) were intended as relatively trivial exercises, involving simulation of the scaled-up system assuming constant average material properties. The purpose of this was twofold:

1) To familiarise the modelling groups (MGs) with the modelling requirements of the upscaled system using a simplified description of material properties, before attempting to use highly complex models of matrix and/or hydrodynamic heterogeneity, and;
2) To establish a calculation baseline for the models produced by each of the modelling groups, against which the impact of more complex heterogeneous matrix and/or flowpath descriptions could be quantified.

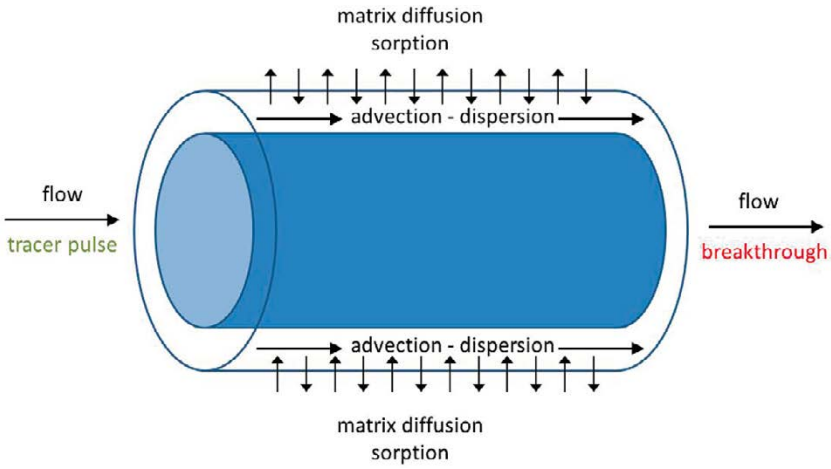

Figure 1-1. *Conceptual illustration of the WPDE experiments. Water (continuous) and tracers (pulse) were injected at one end of the borehole interval. Water flowed along a cylindrical annulus around an inner PEEK[1] dummy and was sampled at the other end of the interval. The length and outer diameter of the interval were 1.905 m and 56.5 mm, respectively. The open cylindrical annulus had an aperture of 1.25 mm.*

Table 1-1. Summary of the Task 9D1 and 9D2 modelling cases.

	Fracture	Matrix	Source term	Solutes	Decay
1a	Moderate dispersion	Constant average properties	Extended 1 ka pulse flux	1 non-sorbing 1 weakly sorbing 1 moderately sorbing 1 strongly sorbing	No
1b	Moderate dispersion	Constant average properties	Constant flux	1 non-sorbing 1 weakly sorbing 1 moderately sorbing 1 strongly sorbing	Yes
1c	Moderate dispersion	Variable properties	Extended 1 ka pulse flux	1 non-sorbing 1 weakly sorbing 1 moderately sorbing 1 strongly sorbing	No
1d	Moderate dispersion	Variable properties	Constant flux	1 non-sorbing 1 weakly sorbing 1 moderately sorbing 1 strongly sorbing	Yes
2a	Moderate dispersion	Constant average properties	Constant flux	^{238}U (4*n*+2 chain)	Yes
2b	Moderate dispersion	Variable properties	Constant flux	^{238}U (4*n*+2 chain)	Yes

[1] PEEK = Polyether ether ketone plastic.

Two separate boundary conditions were defined for cases 1a and 1b, depending on whether radioactive decay was to be included in the simulations. In both cases, the migration of four hypothetical tracer solutes of differing sorptive strength (K_d) was to be simulated. For the non-decay case, a simple extended pulse of 1 ky duration was defined. It was intended that the specification of an extended pulse would facilitate the comparison of MG results, considering both the leading and trailing edges of breakthrough curves to identify salient features related to altered solute retention as modelled by the different MGs. In the radioactive decay case (1b), the use of a constant flux source term was specified so that calculated steady-state breakthrough fluxes could be readily compared with the limiting steady-state solution developed by Sudicky and Frind (1982) to give information concerning effective retention properties evaluated, independently of effective properties calculated by the individual MGs. However, this detail was not communicated to the MGs during Task 9D, since the objective was for each group to develop and motivate their own means of estimating effective retention properties for the system being modelled.

Cases 1c and 1d were specified identically to cases 1a and 1b, except for the additional inclusion of heterogenous matrix properties. The implementation of heterogeneous rock matrix properties was left to the discretion of the MGs, since it depends strongly on the type of heterogeneity being considered and the way in which it is represented in the codes. The only specification was that it should approximately represent the dominant rock type veined gneiss (VGN) as it was previously represented in Task 9A for the purpose of modelling the WPDE experiments. During Task 9D it became clear that the MGs had different approaches to modelling transport retardation heterogeneity that often also included hydrodynamic properties. The descriptions in this evaluation report are therefore amended to reflect this fact, although in the original task description heterogeneity was specified principally for the rock matrix itself.

A similar set up was specified for Task 9D-2, with an initial case assuming constant average material properties (2a), followed by a case incorporating heterogeneous material properties (2b). In Task 9D-2 however, the migration of ^{238}U and its decay chain progeny were to be modelled. Sorption K_d values for uranium and decay progeny in the ^{238}U decay chain were based on the data recommendation given in Hakanen et al. (2014) for Olkiluoto T-series mica gneiss (T-MGN) in contact with brackish reducing high-carbonate groundwater of designated OLBA[2] type (Vuorinen and Snellman 1998).

[2] OLBA – Olkiluoto Brackish Anoxic reference water.

2 Models and parameters

Seven modelling teams participated in Task 9D. Due to the practicalities of adapting very detailed pore-scale models to the much larger spatial and temporal scales in Task 9D, not all teams were able to model the task exactly as specified. The different teams and their modelling approaches are summarised in Table 2-1.

Table 2-1. The modelling teams participating in Task 9D, their concepts, and modelling codes or tools. (note: dimensionality of model concept refers to representation of the rock matrix).

Team	Modelling concept	Code or tool
Amphos 21	2 modelling approaches: 1D parametric continuum model Non-parametric model (time domain random walk)	Analytical solution MARFA
Technical University of Liberec (TUL)	1D fracture and 2D rock matrix	Flow 123D
Nuclear Research Institute (UJV)	1D fracture and 2D rock matrix	Goldsim
Czech Technical University, Prague (CTU)	1D fracture and 2D rock matrix	Analytical solution & Goldsim
PROGEO	1D fracture and 2D rock matrix	MT3DMS
Royal Institute of Technology (KTH), Dept. of Chemical Engineering	Multichannel 1D continuum model (multiple parallel advective flowpaths) with piecewise homogeneous rock matrix	Analytical solution (Laplace)
Computer-Aided Fluid Engineering AB (CFE)	3D discrete fracture network (micro-DFN) with particle tracking (time domain random walk)	DarcyTools

The first six modelling teams considered advective flow along 1D flowpaths with diffusion into the rock matrix giving a 2D dual porosity representation. The fully numerical based modelling tools used by the SURAO-affiliated modelling groups TUL and PROGEO simulated matrix diffusion as a fully 2D isotropic process. The other modelling groups, with the exception of CFE used analytical and numerical approaches based on a 1D orthogonal representation of matrix diffusion (i.e., a "toothcomb" representation). The KTH modelling group additionally considered multiple independent flowpaths with hydrodynamic properties sampled randomly from a statistical flow model. The CFE modelling had by far the most sophisticated treatment of rock matrix heterogeneity with a full 3D pore-scale representation, albeit for a very short flowpath and cm-scale maximum diffusion depth in the rock matrix. A more detailed overview of the modelling approaches adopted by each of the modelling groups and discussion of main findings is given in the following sections.

2.1 Amphos 21

The Amphos 21 modelling group adopted two very different modelling approaches for Task 9D. The first "parametric" modelling approach was based on the analytical solution described by Tang et al. (1981), using effective retardation parameters derived from interpretation of late time breakthrough curves from the REPRO WPDE-1 and WPDE-2 in situ experiments (Löfgren and Nilsson 2019, Soler et al. 2019). The effective retardation parameters for tracers used in the experiment were obtained by comparing the height of normalised breakthrough curves (measured) and the asymptotic form of the Tang analytical solution for a single rate matrix diffusive process in the absence of hydrodynamic dispersion:

$$\lim_{t\to\infty} \gamma(t) = \frac{\beta\kappa}{2\sqrt{\pi}} t^{-3/2} \qquad (2\text{-}1)$$

As demonstrated by Haggerty et al. (2000), the late time solution is relatively insensitive to the presence or absence of hydrodynamic dispersion. Furthermore, in the case of a boundary condition that roughly approximates a Dirac pulse, the breakthrough curve retains little memory of the exact shape of the boundary condition and is largely determined by the magnitude of the input function boundary condition (i.e., the total amount of injected tracer). An underlying assumption of this analysis is that the solute breakthrough has been monitored for sufficient time that onset of the late time breakthrough curve slope of −3/2 is established. The intercept of the line drawn on double logarithmic axes fitted to the late-time breakthrough can then be used to estimate the materials property group κ (m/y^{½}) if the transport resistance parameter β (y/m) is known (β is otherwise referred to as the F-factor in this report). The materials property group, κ (m/y^{½}) is defined as:

$$\kappa = \varepsilon_p \sqrt{D_p R_p} = \sqrt{\varepsilon_p D_e R_p} \qquad (2\text{-}2)$$

Using the effective parameters derived from the in situ experiments, breakthrough curves for the same tracers can be calculated for different F-factors, such as the SA scenario specified for Task 9D. Unfortunately, the effective material properties of the WPDE tracers can only be loosely associated with those specified for Task 9D. The modelling group suggest that HTO should be considered a proxy for tracer A in Task 9D, whereas ^{22}Na and ^{85}Sr might be considered proxies for the weakly sorbing tracer C. The material properties group, κ for tracer C as specified in Task 9D is roughly 80 % of that for ^{85}Sr based on the parameter values assumed by the modelling group in the blind predictions for Task 9A (Soler et al. 2019), which makes it a reasonably close match on that basis. When comparing the Task 9D specification with the effective κ-parameters estimated from the WPDE-2 experiment, however, ^{85}Sr and ^{22}Na are a closer match for a tracer with retardation properties intermediate to those of tracer A and B, reflecting the lower matrix retention observed during the experiment.

Figure 2-1 shows the difference in breakthrough calculated for the original WPDE-2 and WPDE-2 experiments depending on whether the retardation parameters are assigned from independent laboratory experiments (taken from Task 9A) or estimated from the measured breakthrough. The lower level of the measured breakthrough at late times implies a smaller retardation effect on transport of ^{22}Na and ^{85}Sr than predicted by the laboratory derived parameter values (cf Figure 2-1A,C and Figure 2-1B,D).

In the second “non-parametric” approach, the breakthrough curve of solutes from the WPDE experiments was interpreted directly as a residence time distribution and used to estimate the breakthrough curve of a much longer transport flowpath by convolution with itself a sufficient number of times, assuming statistically similar material properties for the upscaled flowpath. This can be done if the input signal (boundary condition) is sufficiently close to a Dirac pulse on the time scale of transport that de-convolution of the residence time distribution (RTD) from the input signal is not necessary. For the F-factor specified in Task 9D this involved convolution of the RTD over 529 repeated flowpath segments. As in the previous parametric approach, a disadvantage of this method is that it is only possible to model breakthrough of solutes that were studied in the WPDE-1 and WPDE-2 experiments.

Although more detailed results can be found in Appendix 1, an example of the calculated breakthrough is shown in Figure 2-2 for ^{85}Sr, ^{22}Na, ^{36}Cl, and HTO. Comparison of results shows a good agreement between the parametric and non-parametric (upscaling) methods for the solutes studied (^{125}I, ^{22}Na, ^{85}Sr, ^{36}Cl, and HTO). The first breakthrough time and peak breakthrough from the non-parametric model are slightly delayed relative to the parametric model when based on the RTD derived from the WPDE-1 experiment. This is attributed to additional in-plane channelling effects which are not considered in the parametric model. The difference is less when basing the upscaling calculation on the RTD from the WPDE-2 experiment. This is attributed to a diminished impact of in-plane flow channelling for flowpaths featuring higher F-factors, since the F-factor of WPDE-2 is nearly double that of WPDE-1. It is not clear whether this result automatically extends to the more general case of persistent, independent flow channels along a transport path, given that an implicit assumption in the non-parametric upscaling procedure is full mixing between flow channels at the end of each flowpath segment.

As shown in Figure 2-2 the breakthrough curves calculated for ^{22}Na and ^{85}Sr using the Tang analytical solution and material properties specified for the blind predictions in Task 9A are delayed in time with reduced peak breakthrough relative to the other models based on fitting to the measured late time behaviour in the in situ experiments. This is due to the decreased sorptive retardation in the in situ experiment relative to that implied by the K_d values determined for crushed materials in supporting laboratory experiments.

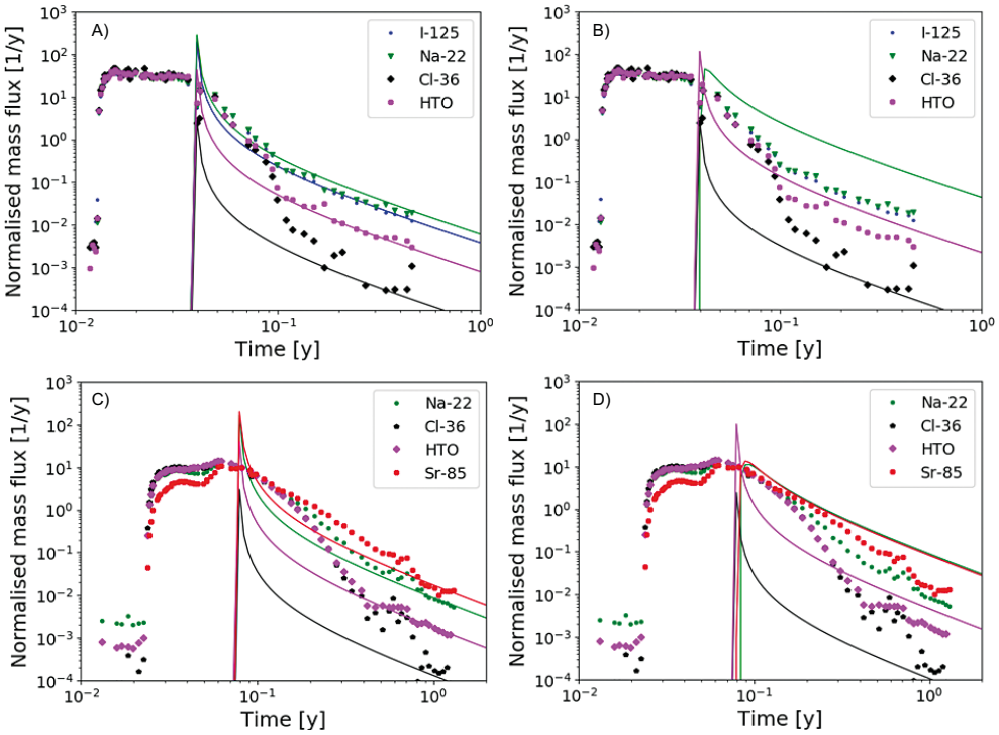

Figure 2-1. *Breakthrough curves (solid curves) calculated for the WPDE experiments using the parametric modelling approach applied to measured breakthrough (markers) from the WPDE-1 (top panels A-B) and WPDE-2 (lower panels, C-D). The plots on the left-hand side (A,C) show results obtained when the material properties group, κ is treated as a fitting parameter based on the height of the late time breakthrough, while plots on the right-hand side (B,D) are "blind" predictions based on parameter values determined in the laboratory characterisation studies.*

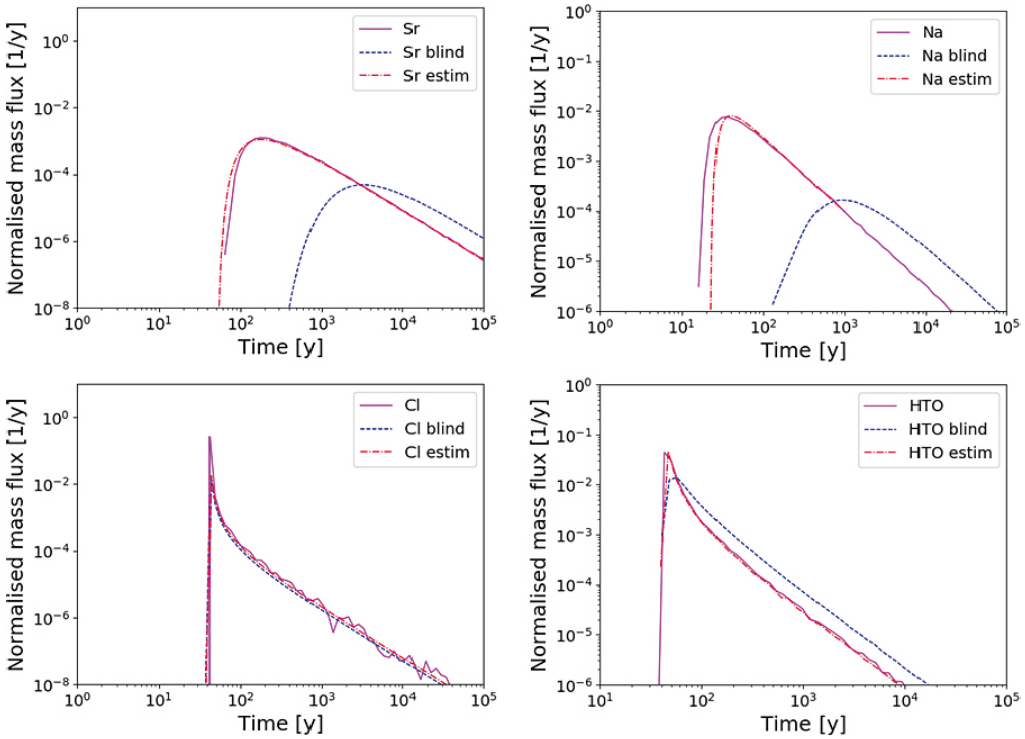

Figure 2-2. *Breakthrough curves calculated for the Task 9D specified flowpath using the parametric modelling approach (broken red curves, labelled "estim"), and non-parametric approach (solid rose-coloured curves), compared to "blind" predictions calculated using parameter values determined in the laboratory characterisation studies (broken blue curves).*

2.2 Modelling groups comprising the Czech SURAO consortium

2.2.1 Technical University of Liberec (TUL)

The modelling group representing the Technical University of Liberec (TUL) chose to model only the reference cases of Task 9D and did not consider the impact of heterogeneity on the SA-scale transport problem. The cases studied were Task 9D-1a,b and 9D-2a and the focus in the reported work was an attempt at inter-group harmonization of results obtained using different numerical codes and a comparison with the analytical solution. The code used was the Flow123d code (TUL 2015)[3] developed in-house at TUL.

In the work performed, the standard processes of advection in a single flow channel featuring Fickian hydrodynamic dispersion, radioactive decay (where appropriate), isotropic 2D matrix diffusive uptake and linear sorption were modelled. Sorption on external fracture surfaces was not included. Fickian dispersion was implemented by defining a 100 m longitudinal and 10 m transverse dispersivity in the model even though the flow domain was formulated in 1D. For the non-chain transport case studies 9D-1a and 9D-1b, comparisons were also made with the Sudicky and Frind (1982) Laplace analytical solution (numerically inverted to the time domain), although without hydrodynamic dispersion. The results obtained using the different modelling tools (see following sections) were used by the modelling group to assess the sensitivity of calculation results to the rock matrix discretisation in the immediate proximity of the fracture surface and modelled matrix depth.

2.2.2 Nuclear Research Institute (ÚJV)

The Nuclear Research Institute, ÚJV Řež used the pipe network model in the commercial GoldSim software (GoldSim 2014) to simulate the Task 9D subtask. The model is based on a standard 1D advective-dispersive flow model coupled to an anisotropic 1D ("toothcomb") description of matrix diffusion including linear sorption and decay processes. Among the different calculation tools employed by the SURAO-affiliated modelling groups, the GoldSim model is considered by the authors to be most accurate since it is partly based on a Laplace model. The model was therefore used as a benchmark against which to compare the performance of the calculation tools used by the other modelling groups. Although material property variability can, in principle, be modelled longitudinally along a flowpath by conjoining multiple pipe elements, the tool can only simulate a homogeneous rock matrix of limited thickness. For this reason, the ÚJV modelling group simulated only the homogeneous cases from Task 9D-1a,b and Task 9D-2a.

2.2.3 Czech Technical University, Faculty of Nuclear Sciences and Physical Engineering, Prague (FJFI/CTU)

Similarly to ÚJV, the modelling group from CTU used the pipe network model in the commercial GoldSim software (GoldSim 2014) to simulate the Task 9D subtask, although complementary calculations were also made using the Laplace analytical solution by Sudicky and Frind (1982) without dispersion. Similarly to the other SURAO-affiliated modelling groups only the Task 9D-1a,b and Task 9D-2a subtasks were modelled. The analytical solution, however, was only applied to the hypothetical tracer cases in Task 9D-1a,b due to the lack of chain decay accounting.

2.2.4 PROGEO

The PROGEO modelling group used the MODFLOW/MT3DMS (Zheng and Wang 1999, Zheng 2010) modelling code to make simulations for Task 9D. The model included advection in a single flow channel featuring Fickian hydrodynamic dispersion, radioactive decay (where appropriate), isotropic 2D matrix diffusive uptake and linear sorption were modelled. The modelling group attempted to define a functionally equivalent model to that produced independently by TUL. Although not stated explicitly in the report this implies that sorption on external fracture surfaces was not included and the same hydrodynamic dispersion parameterisation assuming a 100 m longitudinal and 10 m transverse dispersivity in the model even though the flow domain was formulated in 1D.

[3] http://flow123d.github.io/

2.2.5 Comparsion of modelling results obtained by the SURAO-affiliated groups

Although more detailed results for the SURAO-affiliated groups can be found in Appendix 2, some interesting results for the constant concentration cases including decay (Task 9D-1b) are reproduced in Figure 2-3. The analytical solution calculated by FJFI/CTU has a later arrival time than the other modelling cases presumably due to the neglection of hydrodynamic dispersion. There is also a non-negligible difference between the results calculated by the groups using Goldsim (ÚJV and FJFI/CTU). The difference is particularly clear for tracer A, which is puzzling since they should be identically parameterised models using the same calculation tool. The lower steady-state concentration obtained by FJFI/CTU implies a greater retardation effect than that obtained by ÚJV. According to the authors of the combined SURAO group submission, ÚJV assume a maximum accessible matrix depth of 10 m whereas the other groups assume 1 m. Based on the steady-state form of the Sudicky and Frind (1982) analytical model, however, this should not have any impact on the results for any of the tracers modelled.

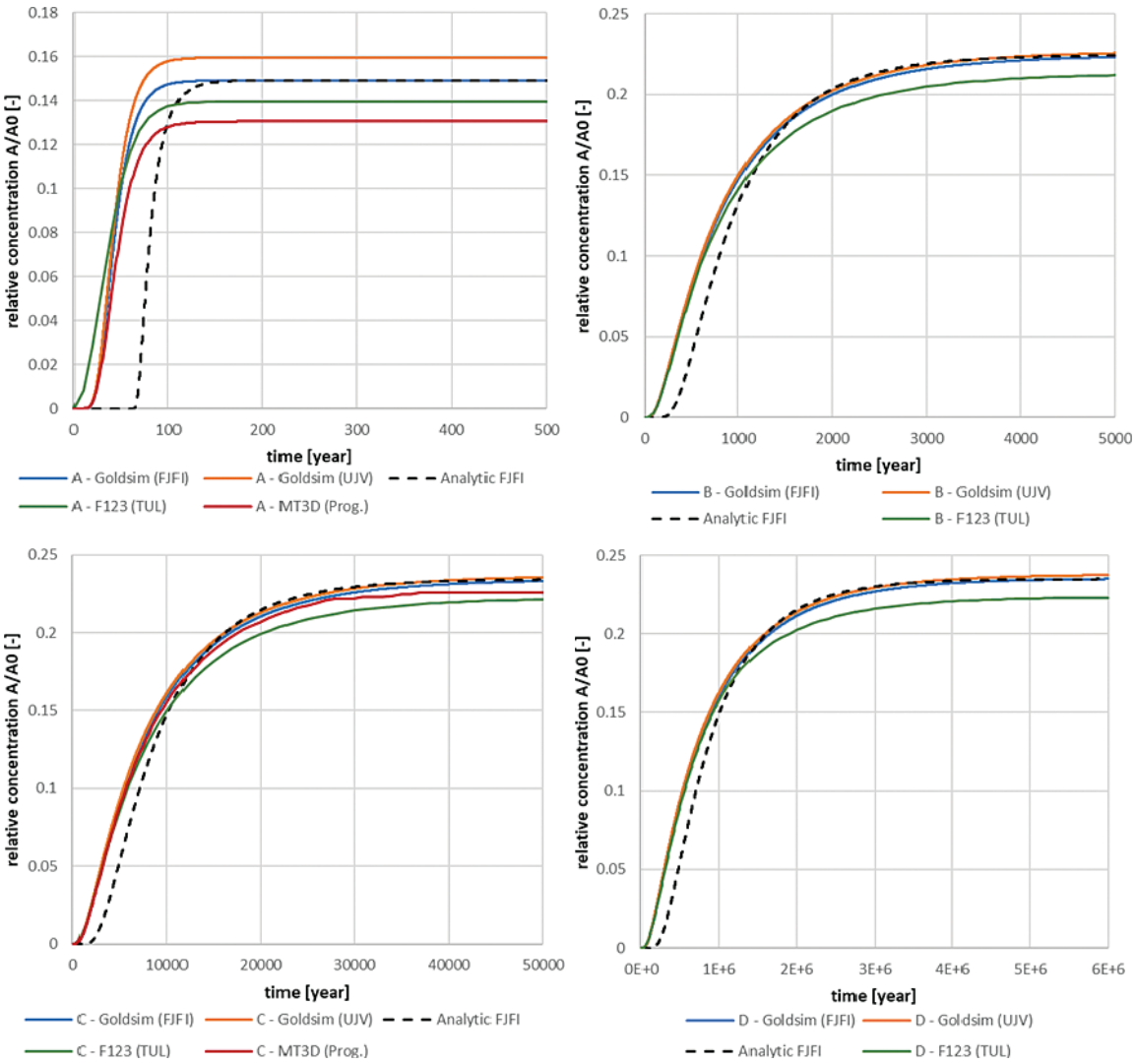

Figure 2-3. *Comparison of breakthrough curves calculated by the SURAO-affiliated modelling groups for the Task 9D-1b subtask for a constant concentration boundary condition with decay. Results are shown clockwise from top left for tracers A through D.*

The steady-state concentration obtained by ÚJV is consistent with an F-factor of 5×10^4 y/m and storage porosity of 4.36×10^{-4}. Although no guidance was given for the effect of anion exclusion on storage in the Task Description, the SURAO consortium agreed to use a 15 times lower effective porosity for tracer A based on that previously used for Cl^- in Task A. The greater retention obtained by FJFI/CTU, however, is consistent with an F-factor exactly half that specified for the problem combined with the water saturation porosity of 6.5×10^{-3} (i.e., the storage porosity corresponding to a cation/neutral species) giving a net increased retardation effect. This suggests that the difference may be due to the combined effect of an improperly specified F-factor and different storage porosity to that used by the other SURAO modelling groups.

The numerical models used by TUL and PROGEO also differ to varying degrees from the ÚJV Goldsim calculations. The GoldSim calculations by ÚJV appear to be the most accurate since they approximately match the steady-state values predicted by the steady-state form of the Sudicky and Frind (1982) analytical model. The results obtained by PROGEO seems to be consistent with an incorrectly specified porosity (i.e., 6.5×10^{-3} rather than 4.36×10^{-4}) with regard to the steady-state concentration of the anionic A-tracer. The deviating results for tracer C obtained by PROGEO, on the other hand, appears to be an artefact of an improperly discretised calculation domain in the MT3D tool for the modelled hydrodynamic conditions in the fracture. This also appears to be the case for the numerical simulation results obtained by TUL using the F123 tool where all modelled tracers appear to exhibit enhanced retardation relative to the ÚJV Goldsim calculations.

2.3 Royal Institute of Technology (KTH)

The KTH Chemical Engineering (KTH-ChE) modelling group took a completely different approach to the other groups and adopted a discrete multichannel approach. The model assumes a large number of independent flow channels of constant width and variable aperture that carry solute without intermixing along the length of the migration path, although with full mixing occurring at the outlet of the modelled domain. In the model, hydrodynamic dispersion arises due to velocity dispersion between discrete flowpaths without the need to invoke a Fickian longitudinal diffusion length. As shown in Liu et al. (2018), the velocity dispersion can be readily estimated if the variance of the aperture field is assumed to be lognormally distributed. For Task 9D the variance of individual flow channel average apertures can be calculated directly from the Péclet number specified for the Task. Similarly, the lognormally distributed flowrate of individual flow channels can be directly calculated from the ensemble mean hydraulic aperture and its variance.

For the heterogeneous matrix cases, the K_d for a flow channel is assumed to be proportional to local mica content in accordance with the task description and described by a Beta distribution. In the task description, the mean mica content of 31.3 % is specified, although the geostatistical representation of heterogeneity was left to the discretion of the modelling groups. The KTH-ChE modelling group explored two separate scenarios for the beta distributed mica fraction, as shown in Figure 2-4. For the heterogeneous cases, the mica content associated with each flow channel was randomly assigned from the Beta distribution. Since the modelling group assumes the Beta distributed mica content to represent the average for the flow channel, rather than local values which are subsequently averaged over a much larger representative elementary volume, there is a relatively extreme variation of mica content between individual flow channels. The variance of K_d as it relates to mica content of the rock may therefore be considered a relatively extreme case of material property heterogeneity. The mica distribution as shown in Figure 2-4 as “base case” (blue curve) was assumed for the base case calculations, while the more extreme variant labelled “variant case” was considered as a sensitivity case study. The model only considers sorption on internal micro-surfaces in the rock matrix and surface sorption on mica exposed at fracture surfaces is neglected.

The case studies incorporating flow channelling together with statistical dispersion in the K_d value for each flow channel result in a spread of first arrival times and differing peak arrival times for individual flow channels, although the late time behaviour is only weakly affected. The statistical dispersion in the breakthrough curves for individual flow channels is greater for smaller numbers of flow channels and approaches the homogeneous case for very large numbers of flow channels. The homogeneous case is calculated using the solution by Tang et al. (1981) for a single migration path with average properties as specified in the task description. When averaged over the multi-channel ensemble in proportion to flow

(i.e., assuming mixing at the outlet), however, most of the differences between the homogeneous and multi-channel cases disappear for the base case calculation. Although not clearly indicated in the report, the ensemble average for the variant case mica distribution also approaches the homogeneous case given a sufficiently large number of independent channels. The impact of including different numbers of independent flow channels on the results is shown in Figure 2-5 for the strongly sorbing tracer D in Task 9D-1a neglecting decay. In the limit of an infinite number of flow channels, the result becomes indistinguishable from the homogenous case assuming average hydrodynamic and material properties.

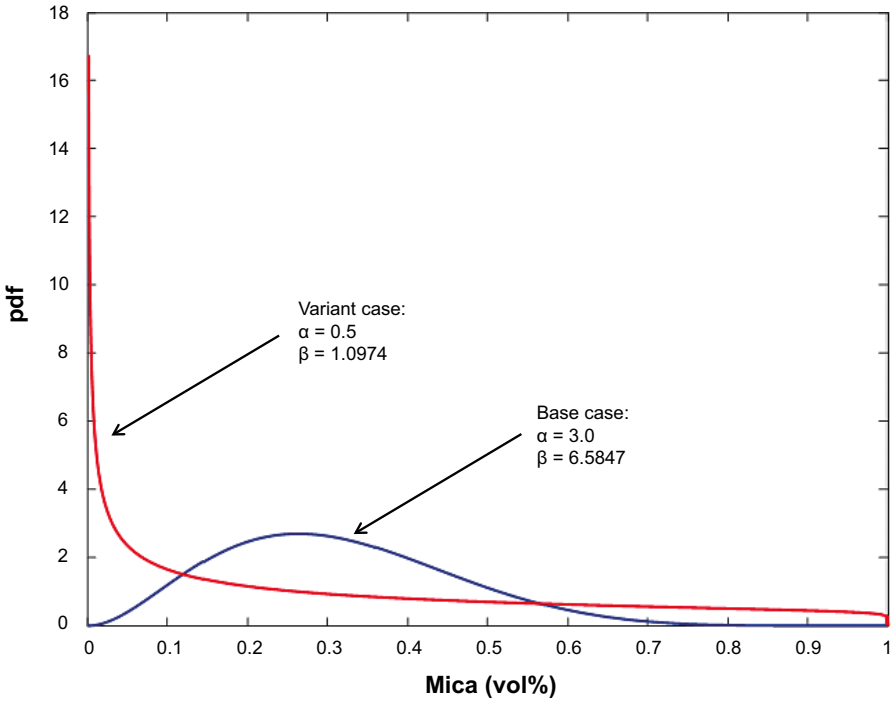

Figure 2-4. *Probability density functions describing mica content of individual migration paths, assuming a Beta-distributed mica volume fraction with an average of 31.3 % as specified in the task description. Two different parametrisations of the Beta-distributed mica content were assumed; one with a relatively low statistical dispersion and median close to the expected average (blue curve); and a more extreme variant with large statistical dispersion and median much lower than the expected average (red curve).*

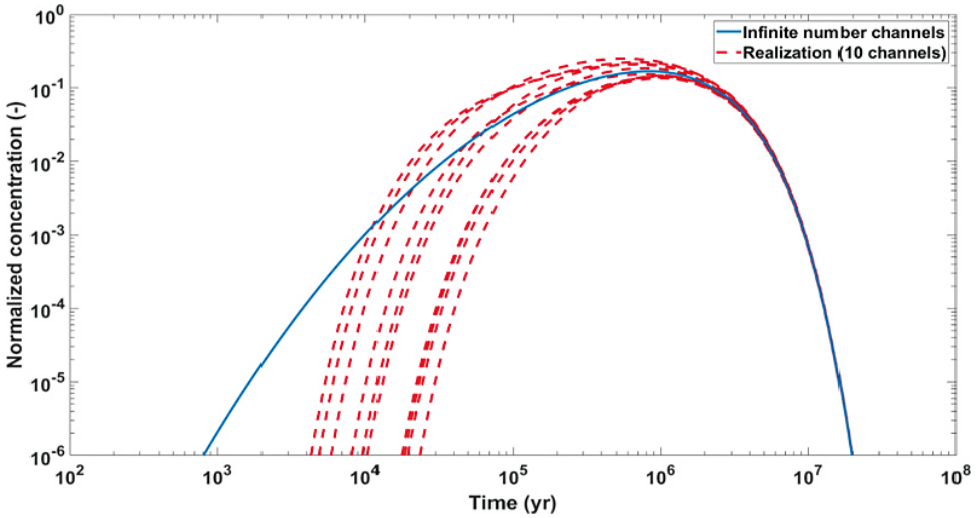

Figure 2-5. *Breakthrough curves for different numbers of independent flow channels in a fracture, for the strongly sorbing tracer D (K_d = 0.1 m^3/kg) in Task 9D-1 (extended pulse boundary condition, no decay).*

2.4 Computer-Aided Fluid Engineering AB (CFE)

The CFE modelling group focused on a very detailed description of rock matrix heterogeneity based on a microscale discrete fracture network (micro-DFN). The methodology is described in more detail in Svensson et al. (2019a) and uses an X-ray micro computed tomography (X-μCT) map of individual mineral grains in a sample of veined gneiss (VGN). A discrete fracture network is then generated with fractures roughly centred on grain boundaries identified in the X-μCT map. The micro-DFN has random fracture orientations and a power law distribution of lengths spanning 50–100 mm. Based on the properties of individual fractures (e.g., aperture, diffusivity) and their spatial intensity, material properties are then assigned to an equivalent porous medium (ECPM) mapped to the network of grain boundaries as described in Svensson (2001). The resulting model is approximately the same as that used previously in Task 9A (Soler et al. 2019) and 9C (Soler et al. 2021).

Solute transport is modelled using a time domain random walk (TDRW) algorithm (Russian et al. 2016) implemented in DarcyTools (Svensson and Ferry 2014). Properties of the micro-DFN fractures used to generate the equivalent porous medium are adjusted to match the mean effective diffusivity and porosity of the rock, as specified in the Task 9D task description. This is achieved by matching breakthrough of particles to an analytical solution in a through-diffusion configuration. The transport model considered advection, diffusion, longitudinal Taylor dispersion (although this was considered to be negligible) and sorption on external fracture surfaces, as well as matrix diffusion and sorption in cells associated with minerals deemed sorbing in the X-μCT map.

The sorption of reactive tracers is formulated in terms of a statistical probability model with characteristic waiting times for sorption and desorption. In this representation, the sorptivity (i.e., K_d) is related to the net transport time of solute transported through the rock matrix. In Svensson et al. (2019a) an empirical relation is derived, giving the K_d value in terms of the characteristic time of desorption, T_d (i.e., $K_d = 2.6 \times 10^{-6} \sqrt{T_d}$). However, the expression is only strictly valid for the VGN sample used in the through-diffusion model used to calibrate the model and the particular grid size used in the discretisation of the modelling domain. The modelling group did not model the tracers specified in the task description, but rather a range of T_d times ranging in decades from 0 to 10 000.

Owing to the complexity of the model, only a very short flowpath could be modelled with length (12.5 mm) and width (10 mm) equal to the corresponding dimensions of the X-μCT grain map used to generate the heterogeneous rock matrix with maximum penetration depth (15 mm). A case study was also carried out in which the smaller model was extended to 100 mm by tessellation of the underlying ECPM. The fracture fluid velocity assumed in the reference case calculations (~10 m/y) also differed from the Task 9D specification (16.6 m/y), giving an F-factor of 12.23 y/m and advective travel time of ~12 h. This is about 4 000 times less than for the 1 000 m flowpath specified in the task description.

In principle, the flowpath could be extended to give the appropriate flowpath F-factor using the tessellation procedure described previously, however this would have been computationally prohibitive given that the rock matrix is modelled with a 27.16 μm grid resolution. Another possibility would be to reduce the flow velocity to give the required F-factor and advective travel time. However, then the sampled heterogeneity in the rock matrix would be disproportional to the true heterogeneity on a 1 000 m scale. In either case, it would be necessary to increase the depth of the rock matrix (presumably using the same tessellation approach) to avoid diffusive saturation of the limited rock matrix.

For the modelled F-factor, the effective penetration depth (Crawford and Löfgren 2019) associated with peak breakthrough can be calculated as roughly 64 μm, with > 90 % of the transported particles penetrating no further than 2 mm into the rock matrix. For the F-factor of 5×10^4 y/m specified in the task description, on the other hand, the effective penetration depth associated with peak breakthrough would be ~4 000 times larger (2.6 cm), with a maximum penetration depth of about 57 cm (i.e., for ~90 % of transported particles).

The modelling group performed sensitivity studies to assess the impact of various underlying modelling assumptions. Reducing the mean fluid velocity or increasing the transport path length increases the interaction with the rock matrix and consequently the effective penetration depth for a given solute recovery fraction. No impact on breakthrough was observed when Taylor dispersion was included, although this was due to the short time associated with diffusion across the fracture aperture (~1 s) relative to the much longer breakthrough times modelled. Sorption on the flow channel wall had a

very strong impact on the modelled solute retardation, due to the easy accessibility of these sorption sites to the advectively transported solute. The peak was very strongly delayed by the inclusion of fracture surface sorption for the modelled hydrodynamic conditions, although there was no impact on the late time tailing. The authors found that neglecting matrix diffusion (i.e., blocking transport within the ECPM matrix elements) had little effect on the peak height and timing and only resulted in disappearance of the matrix diffusive tailing characteristic which is consistent with surface sorptive retardation only. Neglecting molecular diffusion in the flow channel causes a sharpening of the initial breakthrough and increase in the peak height. However, it was found to have no impact on the matrix diffusive tailing, which remained the same.

An interesting sensitivity study that could have been performed would have been to compare results between the short (12.5 mm) and long (100 mm) flowpath, whilst adjusting flow velocity to give the same F-factor in each case. In such a case study, the results would be expected to be indistinguishable if micro-scale heterogeneities are averaged out, and any deviations between breakthrough curves should arise entirely due to the influence of heterogeneity regarding the matrix retention properties. This assumes that the surface retardation factor is identical in both cases, which seems a reasonable assumption for the block-wise tessellated system as it is described in the modelling group report. If the same F-factor were to be used in both cases, then the depth of sampled rock matrix should also be the same, although the scale of micro-scale heterogeneities relative to the modelled migration path length would be 8 times greater for the short flowpath than for the long flowpath.

3 Summary and conclusions

The work performed by the different modelling groups reflected a relatively broad range of approaches to the problem of extending models developed for interpretation of cm-to-m-scale tracer experiments to a km-scale SA setting. The hydrodynamic transport resistance of the upscaled transport problem was roughly 1 000 times that achieved in the REPRO WPDE experiments. The intention was to allow the modelling groups the freedom to define the overall approach and focus of the upscaling problem, which was only minimally constrained by the Task 9D specification.

The Amphos 21 team used two different approaches. One involved interpreting the late time breakthrough in the REPRO WPDE experiments to obtain an effective material property group parameter, which was then used to model the upscaled SA transport problem. The second approach was based on convolution of the residence time distribution quantified in the WPDE experiment. Unfortunately, results obtained using both approaches were restricted to the tracers studied in the WPDE experiments and could not be used to make predictions for the tracers specified in the task description. Nevertheless, using the first approach it was found that the material properties group derived from the late time slope for the weakly sorbing solutes Na-22 and Sr-85 was less by a factor of 5–10, relative to the estimate based on independently obtained laboratory data. For non-sorbing HTO the material properties group was roughly three times less (implying lesser retention in the experiment than expected).

The material properties group is defined as the square root of the product of effective diffusivity, D_e and storage capacity, $\varepsilon_p + K_p\rho_b$. Since retarded travel time for a sorbing solute is proportional to the product of effective diffusivity and storage capacity, this means that an order of magnitude increase in the material properties group can imply two orders of magnitude increase in retarded transport time for the sorbing tracers and nearly a factor of 10 for HTO. Interestingly, the result for Cl-36 is roughly as expected. This might be related to a slightly overestimated anion exclusion factor for the independently obtained D_e for anions, although could equally well be related to inaccurate estimation of the late time behaviour for this solute (as noted by the modelling group in their report). Using the second approach, a reduced impact of flow channelling was observed for the upscaled results, although this might be related to the implicit non-persistence of flow channels when the summed breakthrough is used as a basis for the residence time distribution convolution.

The teams from the Czech Republic comprising the SURAO consortium did not study issues related to the scale up of models of heterogeneity and chose to model only the reference cases. The main purpose of this submission was to study differences between different modelling tools adopted for the calculations, to harmonize results between different tools. Sensitivity of modelled results to grid discretisation in the immediate vicinity of the fracture surface was highlighted as an important factor.

The KTH modelling group took another approach, using a multichannel representation with material properties (K_d) assigned from a β-distribution assuming proportionality with average mica content of the rock along individual flow channels. There was a moderate impact of multichannel flow heterogeneity for the early breakthrough curve (BTC) arrival for strongly sorbing tracer relative to reference cases (there was little effect for weakly sorbing tracers), although when summed in proportion to flow over all flow channels, the results were essentially indistinguishable from the homogeneous reference case represented as a single flow path. There was a negligible impact of flowpath heterogeneity for late tracer BTC arrival relative to reference cases (this was also true for the U-238 decay chain studied in Task 9D-2). Different β-distributions for K_d have moderate impact on statistical dispersion of BTCs for individual flow channels, although the proportionality of K_d with mica content has a relatively weak effect on BTC retention, due to the limited range of mica content variation.

The CFE modelling group used a very detailed pore-scale model of matrix heterogeneity that represented diffusive transport in the grain boundary porosity derived from X-μCT measurements on a sample of the veined gneiss (VGN) rock type specified for Task 9D. Hydrodynamic heterogeneity was not modelled beyond standard Taylor dispersion in the main flow channel. Due to the highly resolved 3D pore-scale representation, calculations could only be made for a very short (cm-scale) path length. In a separate calculation this was upscaled to a flowpath that was roughly eight times longer by tessellation of the matrix microstructure map of the short path segment. It was found that

sorption at fracture surface dominated the BTC at short to medium timescales, while matrix retention dominated late time behaviour. Matrix retention was also found to be increasingly important over longer transport scales.

In general, the different modelling groups adopted some interesting approaches to simulate the Task 9D case studies. As demonstrated by the CFE modelling group, scale-up of extremely detailed pore-scale models of the rock matrix is difficult over increasingly large spatial scales and shortcuts are necessary to make the problem tractable. The approach adopted by CFE of using a tessellation of a smaller scale micro-DFN domains to represent a longer path length was a useful work-around, although still sufficiently computationally intensive that only a 100 mm transport path of very limited matrix depth could be modelled. Amphos 21 abandoned their detailed scale modelling tools adopted in previous tasks in favour of two semi-empirical approaches based on interpretation of breakthrough data from the WPDE experiments and up-scaling of the empirical data to the SA-scale. This approach seems more practical than that adopted by CFE, although it suffers from the drawback that only solutes studied in the small scale WPDE experiment can be extrapolated to the safety assessment (SA) case. There are also substantial questions related to the depth of rock sampled in the WPDE experiment relative to that modelled in the SA case that remain unaddressed in this submission.

The hydrodynamic transport resistance (F-factor), for example, is 778 times greater for the SA case than for the WPDE-2 experiment. Assuming that the material properties sampled in the experiment represent an approximate average for the rock, this implies an effective depth of matrix penetration on the SA-scale that is 778 times greater than that experienced by solute in the experimental study. The key assumption in the extrapolation of WPDE experimental results to the SA-scale is that the material properties characteristic of the first 50 μm of the rock matrix (the average depth of rock matrix sampled in WPDE-2) are similarly representative of the first 4 cm of rock matrix associated with retardation in the SA case study. This assumption appears to underlie both empirical approaches adopted by the Amphos 21 modelling group, although is not discussed in the submission.

The submission by the KTH modelling group was more closely related to their previous work in Task 9A where there was a focus on hydrodynamic heterogeneity, although here extended to address sorptive heterogeneity in the rock matrix. The statistical model of rock matrix heterogeneity described in the submission, however, is adopted with little supporting argumentation concerning whether, or not it is a realistic representation of material property variability. Even though it is an interesting numerical experiment, the relevance of the results for transport calculations on the SA-scale is not clearly articulated by the authors.

Unfortunately, not all of the modelling groups seem to have addressed the underlying objectives of the Task as outlined by the questions posed in Section 1. Although these questions were not explicitly stated in the Task Description, they were communicated as part of the overarching theme of the work in presentations of the Task 9D at GWTFS recurrent meetings and workshops. The submission that best succeeded in delivering requested performance measures was the contribution from KTH, although seemingly without engaging with the underlying objectives in detail. The submission by Amphos 21 included two innovative approaches to solving the SA-scale problem. The questions posed in Section 1 could only be considered indirectly, however, and the adopted modelling approaches did not provide performance measures for the tracers specified in the task. The interpretation of late time behaviour in tracer experiments, rather than modelling of peak breakthrough seems to be a promising means of avoiding many issues associated with hydrodynamic artefacts, although this was only tangentially related to the aims of the Task. The submission by CFE seems to have had the greatest potential to address questions related to scale-up effects of heterogeneity, although was hampered by the complexity of the approach and difficulty of achieving a sufficiently representative scale to enable non-trivial conclusions to be drawn for SA applications.

Although it may be concluded that the overall aims of the Task 9D were not achieved, the modelling group submissions point the way towards how a future Task of similar nature might be more likely to achieve its goals. As a start, the task definition appears to have been more complex than what the modelling groups were equipped to address with the tools developed to study the previous Tasks 9A–C. This suggests that a task of reduced complexity on an intermediate spatial or temporal scale might have been more appropriate. As an example, it seems clear that much useful information could have been obtained by specifying more modest changes in the modelled domain size and flowrates so that the same tools previously deployed could have been used more effectively. In this regard, extending the

flowpath to the km-scale was probably harmful to the objectives of the Task. It was generally not possible to obtain nontrivial insights for SA applications with such a large jump in scale from Task 9A–C.

The failure of at least some of the submissions to fully engage with underlying mechanistic questions relating to scale up appears to be the result of poor communication of objectives in the task description and related documentation. This could be improved in future by stronger constraints on the posed problem and possibly by reducing the scope of requested performance measures to more specific items with direct coupling to the posed questions. In the present case this might have included a clearer focus on estimation of effective retention parameters rather than breakthrough curves and diffusion profiles which require further analysis to place in a proper context. It is also acknowledged that scheduling issues related to the completion of other tasks may have caused Task 9D to be less prioritised which may have influenced the ambition level of the participating modelling groups.

References

SKB's (Svensk Kärnbränslehantering AB) publications can be found at www.skb.com/publications.

Barten W, 1996. Linear response concept combining advection and limited rock matrix diffusion in a fracture network transport model. Water Resources Research 32, 3285–3296. doi:org/10.1029/96WR02508

Bird R B, Stewart W E, Lightfoot E N, 2002. Transport phenomena. 2nd ed. New York: Wiley.

Byegård J, Hakami E, Hjerne C, Nordqvist R, Cvetkovic V, Drake H, Tullborg E-L, Winberg A, 2017. TRUE-1 Completion. Final report. SKB TR-12-11, Svensk Kärnbränslehantering AB.

Crawford J, Löfgren M, 2019. Modelling of radionuclide retention by matrix diffusion in a layered rock model. SKB R-17-22, Svensk Kärnbränslehantering AB.

Cvetkovic V, 2017. Statistical formulation of generalized tracer retention in fractured rock. Water Resources Research 53, 8736–8759. doi:10.1002/2017WR021187

Cvetkovic V, Selroos J-O, Cheng H, 1999. Transport of reactive tracers in rock fractures. Journal of Fluid Mechanics 378, 335–356. doi:10.1017/S0022112098003450

Detwiler R L, 2008. Experimental observations of deformation caused by mineral dissolution in variable-aperture fractures. Journal of Geophysical Research: Solid Earth 113. doi:10.1029/2008JB005697

Gelhar L W, 1993. Stochastic subsurface hydrology. Prentice Hall.

Gelhar L W, Welty C, Rehfeldt K R, 1992. A critical review of data on field-scale dispersion in aquifers. Water Resources Research 28, 1955–1974. doi:10.1029/92WR00607

GoldSim, 2014. GoldSim Contaminant Transport Module. User's guide, version 6.4. GoldSim Technology Group.

Haggerty R, McKenna S A, Meigs L C, 2000. On the late-time behavior of tracer test breakthrough curves. Water Resources Research 36, 3467–3479. doi:10.1029/2000WR900214

Hakami E, Larsson E, 1996. Aperture measurements and flow experiments on a single natural fracture. International Journal of Rock Mechanics and Mining Sciences & Geomechanics Abstracts 33, 395–404. doi:10.1016/0148-9062(95)00070-4

Hakanen M, Ervanne H, Puukko E, 2014. Safety case for the disposal of spent nuclear fuel at Olkiluoto. Radionuclide migration parameters for the geosphere. Posiva 2012-41, Posiva Oy, Finland.

Havlová V, Hofmanová E, Kolomá K, Trpkošová D, 2016. Realizace a vyhodnocení LTD etapa III. experiment v Grimsel Test Site. Průběžná zpráva projektu 2016. ÚJV Řež, a.s. (In Czech.)

Hokr M, Havlová V, Vetešník A, Gvoždík L, Milický M, Polák M, Reimitz D, Říha J, Trpkošová D, Višňák J, Vopálka D, 2021. Testing of fracture-matrix transport models using in situ data and benchmark problems. Task 9 of SKB Task Force GWFTS – Increasing the realism in solute transport modelling based on the field experiments REPRO and LTDE-SD. SKB P-20-22, Svensk Kärnbränslehantering AB.

Ikonen J, Sammaljärvi J, Siitari-Kauppi M, Voutilainen M, Lindberg A, Kuva J, Timonen J, 2015. Investigation of rock matrix retention properties supporting laboratory studies I: Mineralogy, porosity, and pore structure. Posiva Working Report 2014-68, Posiva Oy, Finland.

Keller A A, 1997. High resolution cat imaging of fractures in consolidated materials. International Journal of Rock Mechanics and Mining Sciences 34, 155.e1–155.e16. doi:10.1016/S1365-1609(97)00181-0

Kukkonen I, Kivekäs L, Vuoriainen S, Kääriä M, 2011. Thermal properties of rocks in Olkiluoto: Results of laboratory measurements 1994–2010. Posiva Working Report 2011-17, Posiva Oy, Finland.

Liu L, Neretnieks I, Shahkarami P, Meng S, Moreno L, 2018. Solute transport along a single fracture in a porous rock: a simple analytical solution and its extension for modeling velocity dispersion. Hydrogeology Journal 26, 297–320. doi:10.1007/s10040-017-1627-8

Löfgren M, Nilsson K, 2019. Task description of Task 9A – Modelling of REPRO experiments WPDE-1 and WPDE-2. Task 9 of SKB Task Force GWFTS – Increasing the realism in solute transport modelling based on the field experiments REPRO and LTDE-SD. SKB P-17-18, Svensk Kärnbränslehantering AB.

Mahmoudzadeh B, Liu L, Moreno L, Neretnieks I, 2014. Solute transport in a single fracture involving an arbitrary length decay chain with rock matrix comprising different geological layers. Journal of Contaminant Hydrology 164, 59–71. doi:10.1016/J.JCONHYD.2014.05.011

Neretnieks I, 2002. A stochastic multi-channel model for solute transport – analysis of tracer tests in fractured rock. Journal of Contaminant Hydrology 55, 175–211. doi:10.1016/S0169-7722(01)00195-4

Neretnieks I, 2006. Channeling with diffusion into stagnant water and into a matrix in series. Water Resources Research 42. doi:10.1029/2005wr004448

Nilsson K, Byegård J, Selnert E, Widestrand H, Höglund S, Gustafsson E, 2010. Äspö Hard Rock Laboratory. Long Term Sorption Diffusion Experiment (LTDE-SD). Results from rock sample analyses and modelling. SKB R-10-68, Svensk Kärnbränslehantering AB.

Painter S, Cvetkovic V, Mancillas J, Pensado O, 2008. Time domain particle tracking methods for simulating transport with retention and first-order transformation. Water Resources Research 44. doi:10.1029/2007WR005944

Poteri A, Andersson O, Nilsson K, Byegård J, Skålberg M, Siitari-Kauppi M, Helariutta K, Voutilainen M, Kekäläinen P, Ikonen J, Sammaljärvi J, Lindberg A, Timonen J, Kuva J, Koskinen L, 2018a. The First Matrix Diffusion Experiment in the Water Phase of the REPRO Project: WPDE 1. Posiva Working Report 2017-23, Posiva Oy, Finland.

Poteri A, Andersson O, Nilsson K, Byegård J, Skålberg M, Siitari-Kauppi M., Helariutta, K., Voutilainen, M, Kekäläinen P, Ikonen J, Sammaljärvi J, Lindberg A, Timonen J, Kuva J, Koskinen L, 2018b. The Second Matrix Diffusion Experiment in the Water Phase of the REPRO Project: WPDE 2. Posiva Working Report 2017-24, Posiva Oy, Finland.

Ross S M, 1985. Introduction to probability models. 3rd ed. Orlando, FL: Academic Press.

Russian A, Dentz M, Gouze P, 2016. Time domain random walks for hydrodynamic transport in heterogeneous media. Water Resources Research 52, 3309–3323, doi:10.1002/2015WR018511.

Selroos J-O, Cvetkovic V, 1992. Modeling solute advection coupled with sorption kinetics in Heterogeneous formations. Water Resources Research 28, 1271–1278. doi:10.1029/92wr00011

Soler J M, Neretnieks I, Moreno L, Liu L, Meng S, Svensson U, Trinchero P, Iraola A, Ebrahimi H, Molinero J, Vidstrand P, Deissmann G, Říha J, Hokr M, Vetešník A, Vopálka D, Gvoždík L, Polák M, Trpkošová D, Havlová V, Park D-K, Ji S-H, Tachi Y, Ito T, 2019. Evaluation and modelling report of Task 9A based on comparisons and analyses of predictive modelling results for the REPRO WPDE experiments. Task 9 of SKB Task Force GWFTS – Increasing the realism in solute transport modelling based on the field experiments REPRO and LTDE-SD. SKB R-17-10, Svensk Kärnbränslehantering AB.

Soler J M, Kekäläinen P, Pulkkanen V-M, Moreno L, Iraola A, Trinchero P, Hokr M, Říha J, Havlová V, Trpkošová D, Vetešník A, Reimitz D, Višňák J, Vopálka D, Gvoždík L, Milický M, Polák M, Fukatsu Y, Ito T, Tachi Y, Svensson U, Park D-K, Ji S-H, Gylling B, Lanyon G W, 2021. Evaluation report of Task 9C based on comparisons and analyses of modelling results for the ONKALO REPRO-TDE experiment. Task 9 of SKB Task Force GWFTS – Increasing the realism in solute transport modelling based on the field experiments REPRO and LTDE SD. SKB TR-21-09, Svensk Kärnbränslehantering AB.

Sudicky E A, Frind E O, 1982. Contaminant transport in fractured porous media: Analytical solutions for a system of parallel fractures. Water Resources Research 18, 1634–1642. doi:10.1029/WR018i006p01634

Svensson U, 1994. Refined modelling of flow and transport in the numerical model of the Äspö Hard Rock Laboratory. SKB HRL Progress Report 25-94-12, Svensk Kärnbränslehantering AB.

Svensson U, 2001. A continuum representation of fracture networks. Part I: Method and basic test cases. Journal of Hydrology 250, 170–186. doi:10.1016/S0022-1694(01)00435-8

Svensson U, Ferry M, 2014. DarcyTools: A computer code for hydrogeological analysis of nuclear waste repositories in fractured rock. Journal of Applied Mathematics and Physics 2, 365–383. doi:10.4236/jamp.2014.26044

Svensson U, Voutilainen M, Muuri E, Ferry M, Gylling B. 2019a. Modelling transport of reactive tracers in a heterogeneous crystalline rock matrix. Journal of Contaminant Hydrology 277. doi:10.1016/j.jconhyd.2019.103552

Svensson U, Trinchero P, Ferry M, Voutilainen M, Gylling B, Selroos J-O, 2019b. Grains, grids and mineral surfaces: Approaches to grain scale matrix modelling based on X- ray micro-computed tomography data. Springer Nature Applied Sciences 1, 1277. doi:10.1007/s42452-019-1254-1

Tang D H, Frind E O, Sudicky E A, 1981. Contaminant transport in fractured porous media: Analytical solution for a single fracture. Water Resources Research 17, 555–564. doi:/10.1029/WR017i003p00555

Trinchero P, Cvetkovic V, Selroos J-O, Bosbach D, Deissmann G, 2020a. Upscaling of radionuclide transport and retention in crystalline rocks exhibiting micro-scale heterogeneity of the rock matrix. Advances in Water Resources 142, 103644. doi:10.1016/j.advwatres.2020.103644

Trinchero P, Painter S L, Poteri A, Sanglas J, Cvetkovic V, Selroos J-O, 2020b. A particle-based conditional sampling scheme for the simulation of transport in fractured rock with diffusion into stagnant water and rock matrix. Water Resources Research 56. doi:10.1029/2019WR026958

Trinchero P, Poteri A, Gylling B, Selroos J-O, 2020c. Modelling the water phase diffusion experiment at Onkalo (Finland): Insights into the effect of channeling on radionuclide transport and retention. Journal of Hydrology 590, 125399. doi:10.1016/j.jhydrol.2020.125399

Tsang C-F, Neretnieks I, 1998. Flow channeling in heterogeneous fractured rocks. Reviews of Geophysics 36, 275–298. doi:10.1029/97RG03319

TUL, 2015. Flow123d version 1.8.2. Documentation of file formats and brief user manual. Institute of New Technologies and Applied Informatics (NTI), Technical University of Liberec (TUL).

Voutilainen M, Kekäläinen P, Poteri A, Siitari-Kauppi M, Helariutta K, Andersson P, Nilsson K, Byegård J, Skålberg M, Yli-Kaila M, Koskinen L, 2019. Comparison of water phase diffusion experiments in laboratory and in situ conditions. Journal of Hydrology 575, 716–729. doi:10.1016/j.jhydrol.2019.05.069

Vuorinen U, Snellman M, 1998. Finnish reference waters for solubility, sorption and diffusion studies. Posiva Working Report 98-61, Posiva Oy, Finland.

Weast R C (ed), 1989. CRC Handbook of chemistry and physics: a ready-reference book of chemical and physical data**.** 70th ed. Boca Raton, FL: CRC Press.

Winberg A, Andersson P, Hermanson J, Byegård J, Cvetkovic V, Birgersson L, 2000. Äspö Hard Rock Laboratory: final report of the first stage of the tracer retention understanding experiments. SKB TR-00-07Svensk Kärnbränslehantering AB.

Zheng C, 2010. MT3DMS v5.3 Supplemental user's guide, Technical Report to the U.S. Army Engineer Research and Development Center, Department of Geological Sciences, University of Alabama.

Zheng C, Wang P P, 1999. MT3DMS: A modular three-dimensional multi-species transport model for simulation of advection, dispersion and chemical reactions of contaminants in groundwater systems; documentation and user's guide. U.S. Army Engineer Research and Development Center Contract Report SERDP-99-1, Vicksburg, MS.

Zou L, Jing L, Cvetkovic V, 2017. Shear-enhanced nonlinear flow in rough-walled rock fractures. International Journal of Rock Mechanics and Mining Sciences 97, 33–45. doi:10.1016/j.ijrmms.2017.06.001

Appendix 1

Contribution from Amphos 21 – Final report on Task 9D

Paolo Trinchero, Amphos 21

November 2020

A1.1 Executive summary

In fractured crystalline rocks, radionuclides are transported through open fractures by fluid flow and can access the connected pore space of the adjacent rock matrix by diffusion. The mass exchange term between the fracture and the matrix is a function of in-plane groundwater flow patterns. Thus, channelling and preferential flow caused by heterogeneity in fracture aperture have an impact on the overall rock retention capacity. In this work, which was motivated by Task 9D of the SKB Task Force GWFTS, we have used experimental data from the recent Water Phase Diffusion Experiment (WPDE) carried out at ONKALO (Finland), to assess the influence of channelling on contaminant transport and retention at increasingly larger scales. The upscaling was performed by extracting non-parametric Retention Time Distribution (RTD) functions from the experimental data and using them to carry out transport simulations along a segmented pathway. The analysis shows that channelling leads to anomalous early breakthroughs at short scales, whereas at increasingly larger distances this effect is smoothed out and the nuclide breakthrough curves become mostly controlled by mass exchange processes between the fracture and the matrix. This homogenisation is observed at shorter scales for sorbing nuclides. The influence of channelling on radionuclide retention is shown to be modest, due to compensating effects between the shorter groundwater travel times and the larger specific fracture surface area made available through in-plane diffusion into stagnant water.

A1.2 Scope and objectives of the work

The objective of this work is aligned with the general objective of Task 9D, which reads "Task 9D… will focus on extrapolating results from in situ experimental conditions to something more closely resembling a typical Safety Assessment (SA) scenario" (Appendix 5). However, the objective is here pursued using a novel non-parametric approach, in which the heterogeneous signature of WPDE is extracted and numerically convoluted along an idealised transport pathway made up of minimum spatial units (fracture segments), characterised by the same temporal scales and processes as the experimental section of WPDE. It turns out that the results presented in the main part of this document (which are also included in a recent scientific publication (Trinchero et al. 2020c)) are not strictly based on the parameterisation suggested in Appendix 5. To facilitate inter-group model comparison, Section A1.7 has been included, in which the parametric calculations have been repeated along a transport pathway that closely resembles that proposed in Appendix 5.

A1.3 Interpretation of the WPD experiment

A1.3.1 Short overview of the WPD experiment

The WPDE was carried out in a 1.9 m long section of drillhole ONK-PP323, around 18 m away from the niche wall (Figure A1-1). A co-axial dummy was placed in the selected section, which was then packed off. The gap between the dummy and the fracture wall produced an artificial fracture of relatively well-defined geometry (we will use the term "slot" from now on to refer to this artificial fracture). A low steady-state water flow was prescribed at the end of the packed-off section, resulting in water flowing towards the niche. Two different experiments with different flow rates were carried out: WPDE-1 (Q = 20 μL/min) and WPDE-2 (Q = 10 μL/min).

In both experiments, a tracer pulse a few hours long was obtained by adding a cocktail of active tracers to the injection water: HTO, Na-22, Cl-36 and I-125 in WPDE-1 and HTO, Na-22, Cl-36, Sr-85 and Ba-133 in WPDE-2. The injected tracers are displaced along the slot by fluid flow and can diffuse into the rock matrix, where they might eventually be sorbed onto the available sorption sites. Once the concentration gradient is reversed, tracers can back-diffuse into the slot. Tracer activities in the water phase were measured at the end of the packed-off section for over half a year for WPDE-1 and about

one and a half years for WPDE-2. The six radionuclides were chosen so that their retention includes a wide range of values; i.e. from no sorption for neutral species to medium to high sorption for cations. Moreover, the non-sorbing tracer Cl-36 was included to investigate anionic exclusion effects. The retention of iodine was most likely influenced by speciation effects.

WPDE-1 was performed from March to August 2012 and WPDE-2 ran from January 2013 to May 2014. Significantly higher injection activities were used in WPDE-2, which included two additional radionuclides: Sr-85 and Ba-133. The qualitative comparison of the Sr-85 breakthrough curve with the rest of the breakthrough curves of WPDE2 confirms that the residual tracer activity in the rock matrix from WPDE1 has no effect on the breakthrough curves of WPDE2.

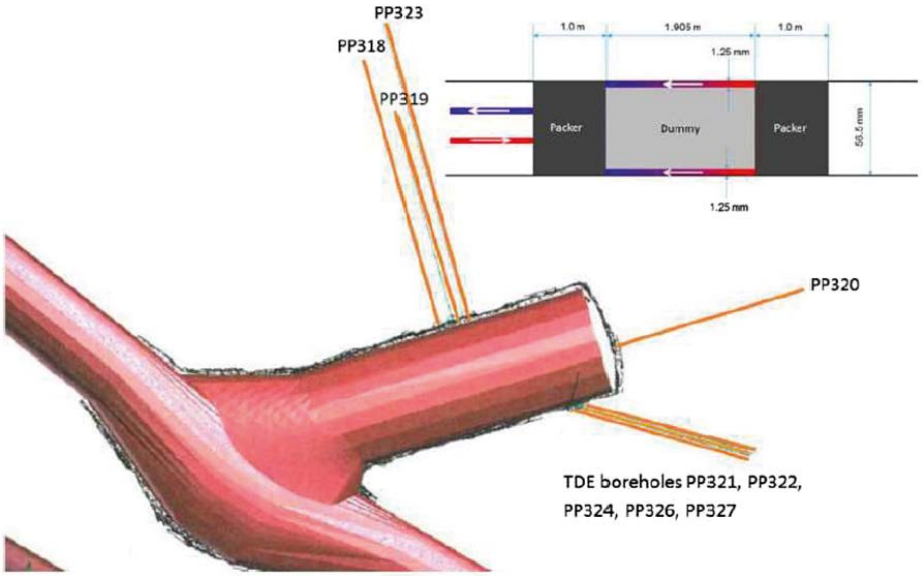

Figure A1-1. *The REPRO niche located at the 401 m level at the underground rock characterization facility of ONKALO (Finland). The orange lines show the different drillholes drilled from the niche wall. The drillhole ONK-PP323 was used to carry out the WPDE. A sketch of the WPDE experimental setup is shown in the upper right corner. In this sketch the arrows show the circulating water, the red line on the left shows the injection point and the blue line shows the extraction point. Figure modified from Poteri et al. (2018a, b) and Löfgren and Nilsson (2019).*

All the parameters of the WPDE experiment are summarised in Table A1-1. The theoretical advective groundwater travel time (τ_{th}) is computed assuming a regular cross section of area $A = \pi(\varnothing\delta - \delta^2)$, where $\varnothing$ [m] is the diameter of the drillhole and δ [m] is the aperture of the slot.

Table A1-1. Parameters of the WPDE experiment.

Symbol	Quantity	Value	
L	Length of packed-off section	1.9 m	
$\varnothing$	Diameter of the drillhole	5.65×10^{-2} m	
δ	Aperture of the slot	1.25×10^{-3} m	
		WPDE-1	WPDE-2
Q	Flow rate	1.1×10^{-4} g/y	5.3×10^{-3} g/y
τ_{th}	Groundwater travel time	3.9×10^{-2} y	7.8×10^{-2} y
β_{th}	Transport resistance	31.3 y/m	62.6 y/m

In fractured systems, matrix diffusion is a function of the so-called transport resistance, which is defined as (Cvetkovic et al. 1999):

$$\beta = \int_0^\tau \frac{d\varepsilon}{b(\varepsilon)} \tag{A1-1}$$

where τ [y] is the groundwater travel time and b [m] is the fracture half aperture. Equation A1-1 is valid for a planar fracture and 1/b [m−1] is the specific fracture surface area (i.e., the fracture surface area available per unit fracture volume). However, the experimental set-up is based on an annular fracture. Hence, in the models presented hereafter, we will map the annular fracture, which has a single outer surface for diffusive mass exchange, into a planar fracture bounded with two matrix surfaces. This mapping is done by defining an equivalent planar fracture that has the same specific fracture surface area as the slot. This gives an equivalent fracture half aperture equal to:

$$b = \delta - \frac{\delta}{\varnothing} \approx \delta \tag{A1-2}$$

The theoretical transport resistance for the two experiments, β_{th}, is listed in Table A1-1.

A1.3.2 Modelling of WPDE

The radionuclide breakthrough curves measured at the fracture outlet for the two experiments are shown in Figure A1-2. These data are decay corrected to the activity at the injection time and normalised by the total injected activity:

$$\gamma_i = \frac{c_i Q}{M_i} \tag{A1-3}$$

where c_i [Bq/g] is the measured decay-corrected aqueous concentration of the i-th radionuclide, Q [g/y] is the applied flow rate and M_i [Bq] is the activity in the injected solution. It is important to note that in WPDE-1 Cl-36 was close to or below detection limit just when the curve reached the tailing. Therefore, the injected activity of Cl-36 was increased in WPDE-2 to get a reliable representation of the tail.

It can be noticed that all the breakthrough curves are characterised by an anomalous rising limb with a significant early arrival, whereas their late-time part follows the power-law behaviour expected in fractured media (Haggerty et al. 2000, Tang et al. 1981). Despite the limited amount of data available to characterise the tail (less than one logarithmic cycle), the expected −3/2 slope (log-log plot) is observed for all the radionuclides except for Cl-36, which would have needed an additional logarithmic cycle of data (this is infeasible since it would have required the experiment to be run for up to 10 years). The clear separation of the tails of the breakthrough curves provides additional evidence of the clear role of matrix diffusion. Exception of the afore-mentioned behaviour is observed for Ba-133 in WPDE-2, which is strongly retarded.

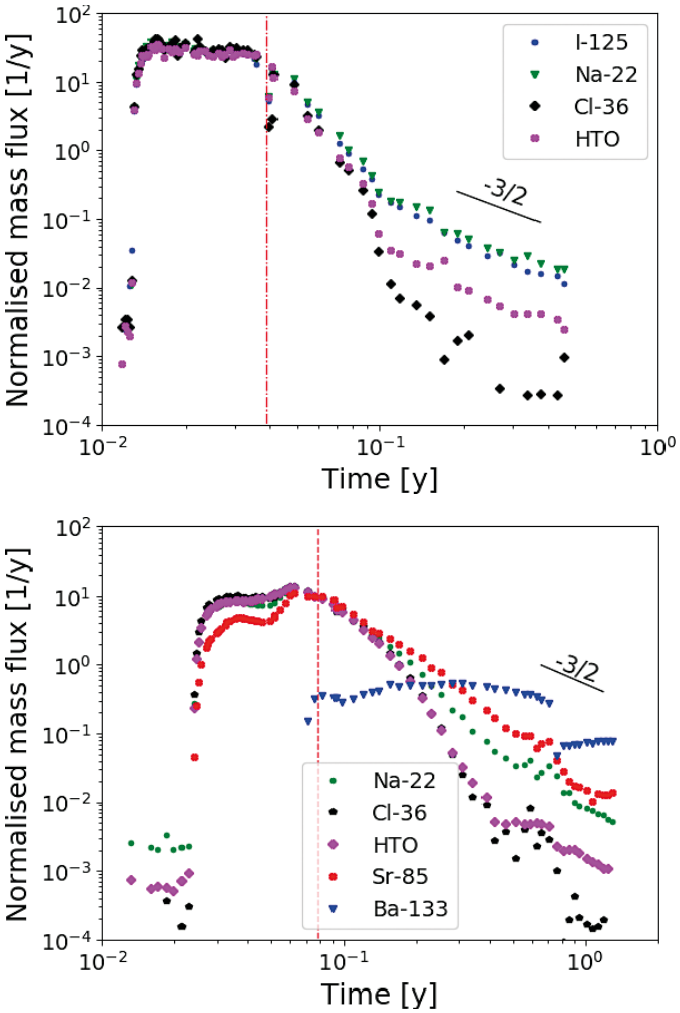

Figure A1-2. *Decay corrected activity normalised by the total injected activity computed at the fracture outlet for WPDE-1(top) and WPDE-2 (bottom). The vertical dashed-dotted lines indicate the theoretical groundwater travel time, τ_{th}.*

The reason for the anomalous early arrivals remains unclear, although it is most probably related to channelling in the slot and preferential flow (Soler et al. 2019). Besides channelling, diffusion into stagnant water regions in the slot and subsequent diffusion into the rock matrix (secondary diffusion) are considered to be significant processes affecting radionuclide transport and retention in the experiment (Poteri et al. 2018a).

The tails of the different breakthrough curves have been extended considering the measured height and the expected −3/2 slope in log-log scale (Figure A1-3). These extended breakthrough curves have been used to calculate a scaling factor, ω [-], which is equal to the relative amount of mass exiting at the outlet:

$$\omega = \int_0^\infty \gamma dt \qquad \text{(A1-4)}$$

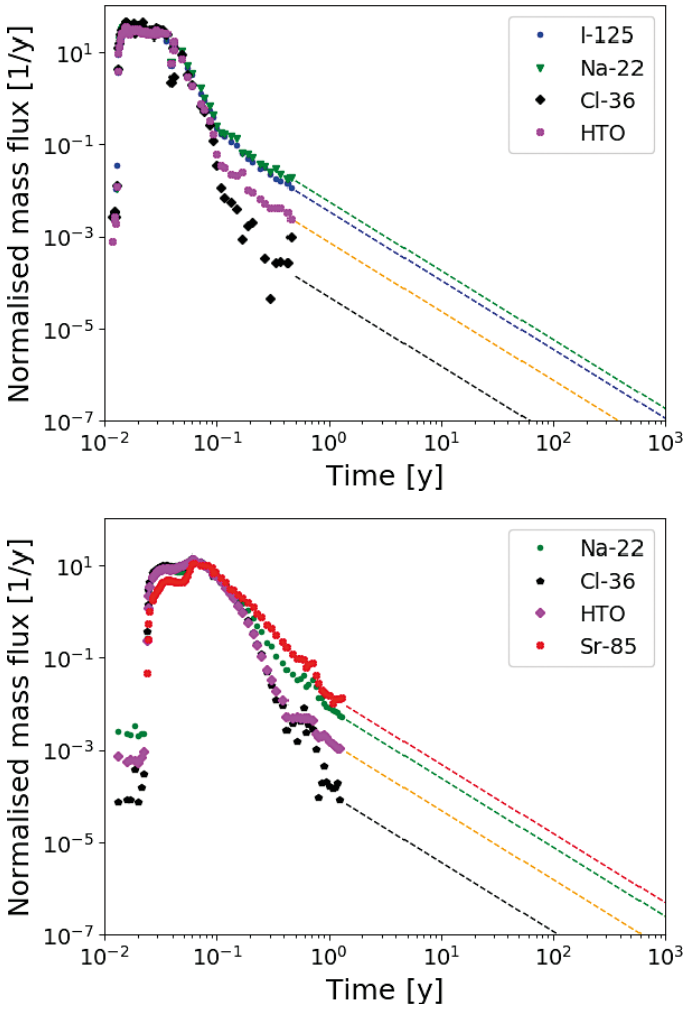

Figure A1-3. *Breakthrough curves of (top) WPDE-1 and (bottom) WPDE-2. The tail of the breakthrough curves has been extended assuming a power-law behaviour with exponent −3/2 (Tang et al. 1981).*

The scaling factors evaluated for the different radionuclides and the two experiments are listed in Table A1-2. Notice that Ba-133 is not considered in this analysis as the available time series is not long enough to show the expected late-time power-law behaviour.

Table A1-2. Scaling factors (Equation A1-4) computed for the different radionuclides and the two experiments.

	ω WPDE-1	ω WPDE-2
I-125	0.90	-
Na-22	0.98	1.00
Cl-36	0.90	0.97
HTO	0.82	0.93
Sr-85	-	1.02
Ba-133	-	0.52

The breakthrough curves were re-scaled by the computed scaling factor so that the total area below the curve adds up to one. The re-scaled breakthrough curves are visually very similar to those of Figure A1-3 and thus are not shown here for the sake of brevity. All the results presented hereafter are compared with the re-scaled experimental breakthrough curves.

The experimental results are interpreted here using the Tang's analytical solution (Tang et al. 1981):

$$\gamma = \frac{\beta\kappa}{2\sqrt{\pi}} exp\left(\frac{-\beta^2\kappa^2}{4t_{ret}}\right) t_{ret}^{-3/2} \quad \text{(A1-5)}$$

where $t_{ret} = t - \tau$ [y] is the retention time in the matrix and κ is a material parameter group defined as:

$$\kappa = \sqrt{\phi D_e R} \quad \text{(A1-6)}$$

where ϕ [-] and D_e [m^2/y] are the porosity and effective diffusivity of the rock matrix respectively. The third term inside the square root is the retardation factor [-], which is defined as:

$$R = 1 + \frac{K_d \rho_s}{\phi} \quad \text{(A1-7)}$$

where ρ_s [Kg/m^3] is the bulk rock dry density and K_d [m^3/Kg] is the radionuclide specific distribution coefficient. It is worth noting that Equation A1-5 does not include longitudinal dispersion. This is an intentional choice, as the objective here is not to fit the early part of the experimental breakthrough curves using some artificial value of in-plane dispersion, but rather to investigate what is the implication of neglecting flow channelling in large-scale simulations.

At late times, Equation A1-5 reduces to:

$$\lim_{t\to\infty} \gamma(t) = \frac{\beta\kappa}{2\sqrt{\pi}} t^{-3/2} \quad \text{(A1-8)}$$

From Equation A1-5 we see that, given the same hydrodynamic processes experienced by the radionuclides (i.e., same β), the tail of the breakthrough curve gives a direct indication of the degree of radionuclide retention. From Figure A1-2 it is evident that in both experiments Cl-36 shows the lowest degree of retention. This is indeed related to the fact that Cl-36 is a negatively charged species ($^{36}Cl^-$) that shows a very low tendency to diffuse into the rock matrix, due to electrostatic repulsion with the also negatively charged mineral surfaces (i.e., anion exclusion). HTO (i.e., tritiated water) is a neutral species and hence is not affected by anionic exclusion and is not sorbed in the matrix, which explains its higher retention compared to Cl-36 and its lower retention compared to the rest of radionuclides. Na-22 and I-125 show a similar, relatively high retention. For sodium, which is present in the form of the positively charged species $^{22}Na^+$, this high retention is mostly related to cation exchange processes in the rock matrix. The relatively high sorption of iodine is related to speciation effects. Sr-85 shows a significantly high retention, consistent with the results of laboratory batch experiments. Using the material parameter group as a general indicator of radionuclide retention, the following relationship holds:

$$\kappa^{Cl-36} < \kappa^{HTO} < \kappa^{I-125} \approx \kappa^{Na-22} < \kappa^{Sr-85} \quad \text{(A1-9)}$$

Given the theoretical value of transport resistance (β_{th}), Equation A1-8 can be used to estimate the value of κ for the different radionuclides and the two experiments. The values of κ estimated from the height of the breakthrough tails are identified with $_{est}$ and are listed in Table A1-1. These estimated values follow the trend discussed above; we see very low values for radionuclides with low retention such as Cl-36, and high values for the strongly sorbing radionuclides such as Sr- 85.

Table A1-3. Material parameter group (κ; Equation A1-6) as estimated from the height of the tail of the experimental breakthrough curves (κ_{est}) and as inferred from laboratory characterisation studies (κ_{blind}).

	κ_{est} [$m^2 s^{-1}$]^{½}		κ_{blind} [$m^2 s^{-1}$]^{½}
I-125	4.0×10^{-4}	-	-
Na-22	6.5×10^{-4}	4.4×10^{-4}	4.6×10^{-3}
Cl-36	5.4×10^{-6}	6.5×10^{-6}	5.3×10^{-6}
HTO	8.5×10^{-5}	8.7×10^{-5}	2.3×10^{-4}
Sr-85	-	8.7×10^{-4}	4.2×10^{-3}

Equation A1-5, the set of estimated material parameter groups (κ_{est}) and the parameters of Table A1-1 have been used to simulate the radionuclide breakthrough curves for the considered radionuclides and the two experimental set-ups. The results are shown in Figure A1-4. As expected, the simulated breakthrough curves capture the long-term radionuclide behaviour. This is because the tails of the curves are controlled by matrix diffusion and this process is in turn properly captured through the estimation of the material parameter group based on the experimental height of the tail. It is also interesting (and not surprising) to notice the significant difference between modelled and experimental results at early and intermediate times. In fact, in both experiments the breakthrough curves are characterised by a sharp and early arrival and a flat peak. The simulated breakthrough curves are also characterised by a sharp rising limb, but it is observed much later (at $t = \tau_{th}$). The simulated peaks are narrow and the related peak values are significantly higher than the experimental data. This simulated behaviour is indeed related to the intentional choice of neglecting in-plane dispersion in these models. Similar discrepancies between modelled and experimental data were already observed in blind predictions performed by different modelling groups in the framework of the SKB Task Force GWFTS (Soler et al. 2019).

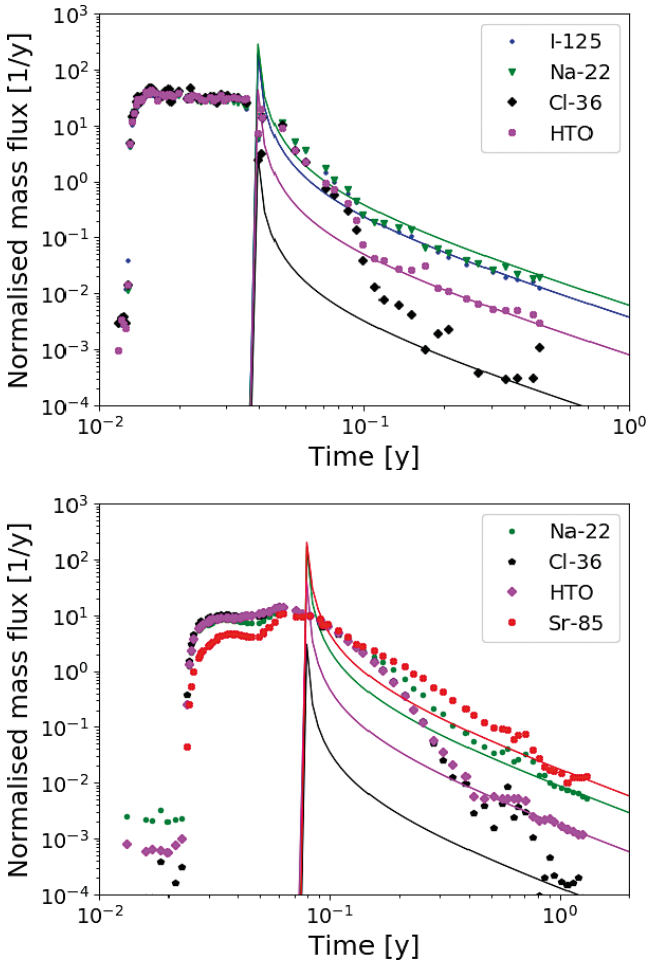

Figure A1-4. *Breakthrough curves computed using Equation A1-5 and κ_{est} for WPDE-1(top) and) WPDE-2 (bottom). The results of the analytical solution are shown with continuous lines, whereas experimental data are shown with different markers.*

Different complementary studies were carried out to support the analysis and interpretation of WPDE. For instance, a replica experiment was run in the laboratory using drill cores taken from the in situ sections (Voutilainen et al. 2019). Besides this replica experiment, characterisations of matrix porosity were carried out by means of water saturation method, argon pycnometry and the 14C-PMMA method, and analyses of matrix diffusion coefficient were performed based on data of through diffusion experiments and electrical resistivity measurements. Additionally, sorption distribution coefficients (K_d values) were determined using laboratory batch experiments on crushed material. The results of these characterisation studies, which are thoroughly described in Poteri et al. (2018a), were used to provide a set of parameters to the modellers of the SKB Task Force GWFTS, which were used for the afore-mentioned blind predictive models (Soler et al. 2019). This set of values is used here to compute an additional set of κ values, which is denoted with $_{blind}$ (see Table A1-3). Notice that this set does not include values for I-125 due to the afore-mentioned issues with iodine speciation. The breakthrough curves computed using Equation A1-5 with κ_{blind} are shown in Figure A1-5. These results show that matrix parameters obtained from laboratory experiments provide a good description of the late-time behaviour of the breakthrough curves for Cl-36 and a slight over-estimation of the height of the tail for HTO. However, retention of sorbing nuclides (i.e., Na-22 in WPDE-1 and 2, and Sr-85 in WPDE-2) is significantly over-estimated. This over-estimation is related to the estimated K_d values. There is in fact evidence that sorption coefficients obtained from batch experiments performed on crushed material over-estimate in situ retention processes (Winberg et al. 2000, Byegård et al. 2017, Voutilainen et al. 2019). As for the previous set of calculations based on κ_{est}, these computed breakthrough curves are remarkably different to the experimental data at short to intermediate times, due to channeling effects that are not accounted for in the models.

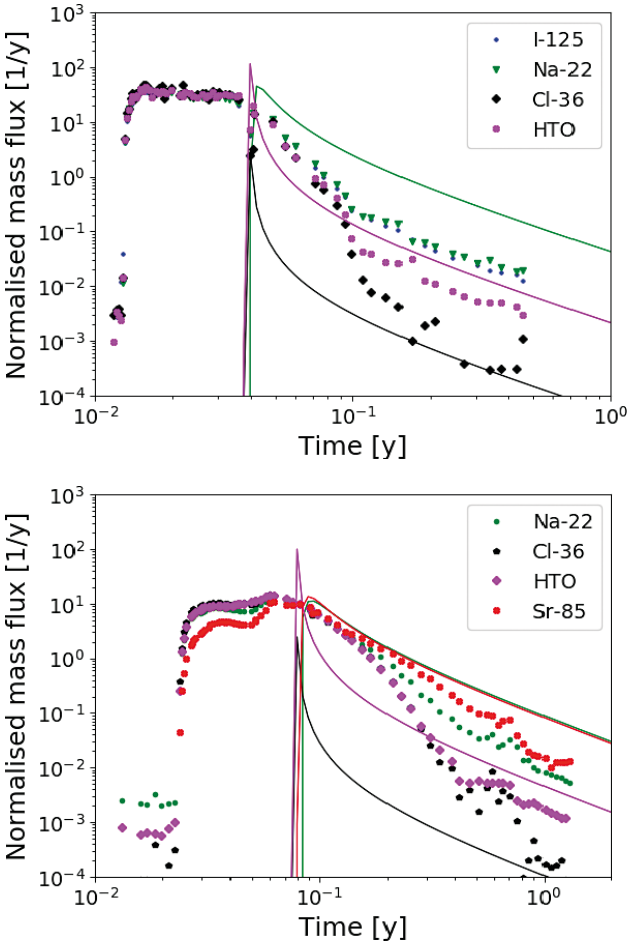

Figure A1-5. *Breakthrough curves computed using Equation A1-5 and κ_{blind} for WPDE-1 (top) and WPDE-2 (bottom). The results of the analytical solution are shown with continuous lines, whereas experimental data are shown with different markers.*

A1.4 Extrapolation of the WPD experiment

A1.4.1 Upscaling the heterogeneous breakthrough curves

The radionuclide breakthrough curves of the in situ experiment can be interpreted using a Lagrangian formulation as (Painter et al. 2008, Trinchero et al. 2020b):

$$\gamma = \int_0^\infty \int_0^\infty f_{ret}(t-\tau|\beta) f_{\tau,\beta}(\tau,\beta) d\tau d\beta \quad \text{(A1-10)}$$

where f_{ret} is the retention time distribution (which describes the time spent by a packet of radionuclide mass in the rock matrix) and $f_{\tau,\beta}$ is the joint probability density for τ and β (which describes in-plane variability in groundwater flow patterns and accounts for the correlation between τ and β). Notice that the retention time distribution can be described using existing parametric models (Painter et al. 2008) while $f_{\tau,\beta}$ is unknown.

An equivalent simplified model, denoted with ^{SM}, is here defined based on the assumption that:

$$\gamma^{SM} = f_{ret}^{SM}(t-\tau_{th}) \quad \text{(A1-11)}$$

By equating Equation A1-11 to Equation A1-10 we get an equivalent simplified model in which the breakthrough curve of the selected radionuclide at the selected spatial scale (the spatial scale of the WPDE experiment in this specific application) is described by a single probability distribution function (f_{ret}^{SM}) that lumps together all the underlying processes, including diffusion and retention in the matrix as well as channelling and dispersion in the slot. This probability distribution function can be directly inferred from the in situ breakthrough curve, which can be thought of as a heterogeneous signal. The propagation of the signal at a larger distance can be evaluated by numerically convoluting f_{ret}^{SM} along a segmented pathway, under the assumption that each segment is characterised by the same in-plane processes (i.e., same $f_{\tau,\beta}$). This upscaling procedure, which has been recently validated by Trinchero et al. (2020a), is implemented within a TDRW numerical framework (Painter et al. 2008).

A1.4.2 The retention time distributions (f_{ret}^{SM}) of the in situ experiment

The retention time distributions (f_{ret}^{SM}) have been extracted from the experimental data using the approach described in the previous sub-section. The scaled extended time series have been used to assess the tail of the distribution. For visual purposes it is interesting to plot the complementary cumulative distribution functions (CCDF), which are defined as:

$$\bar{F}_{ret}(t) = 1 - \int_0^t f_{ret}^{SM}(\xi) d\xi \quad \text{(A1-12)}$$

The CCDFs extracted from WPDE1 are shown in Figure A1-6. The height of the tails of the different nuclides is consistent with the relationship described by Equation A1-9. It is also interesting to notice that $\lim_{\zeta \to 1} \bar{F}_{ret}^{-1}(t)$, meaning that the origin of the cumulative distribution function of t_{ret} occurs at negative times. This is due to channelling processes, which cause the observed early breakthrough. These processes are lumped in to the estimated retention time distribution.

To cross-check their consistency, TDRW calculations are carried out with the extracted f_{ret}^{SM}, using a pathway made of a single segment. The simulations are performed using the computer code MARFA (Painter et al. 2008, Trinchero et al. 2020b). The results are shown in Figure A1-7. All the computed breakthrough curves agree well with the experimental data. The noise of the computed breakthrough curves is due to (i) statistical noise intrinsic to particle-based methods and (ii) noise in the experimental data used to obtain the non-parametric retention time distribution.

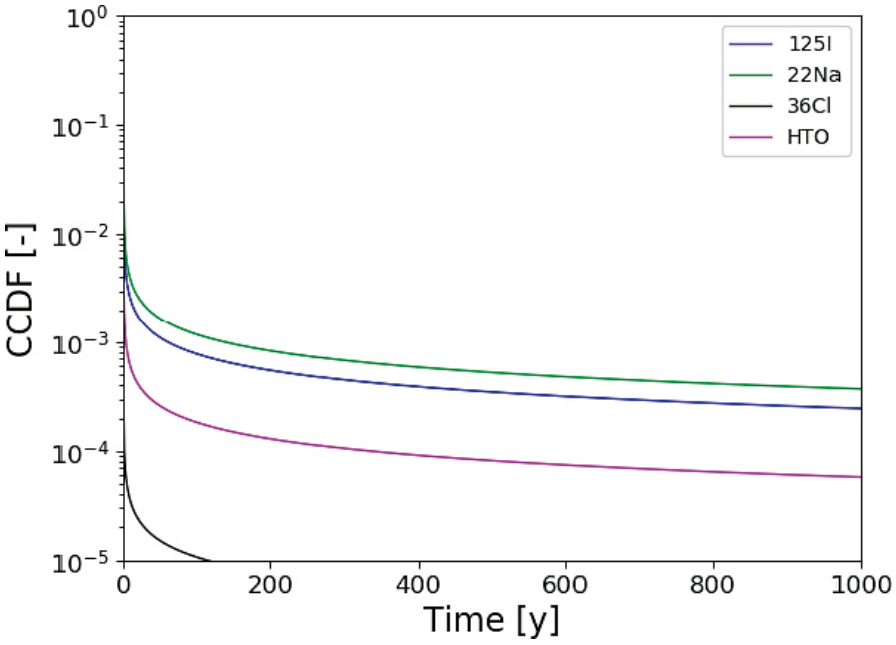

Figure A1-6. *Complementary cumulative density function ($\bar{F}_{ret}$ (t)) extracted from WPDE1 for the four considered nuclides.*

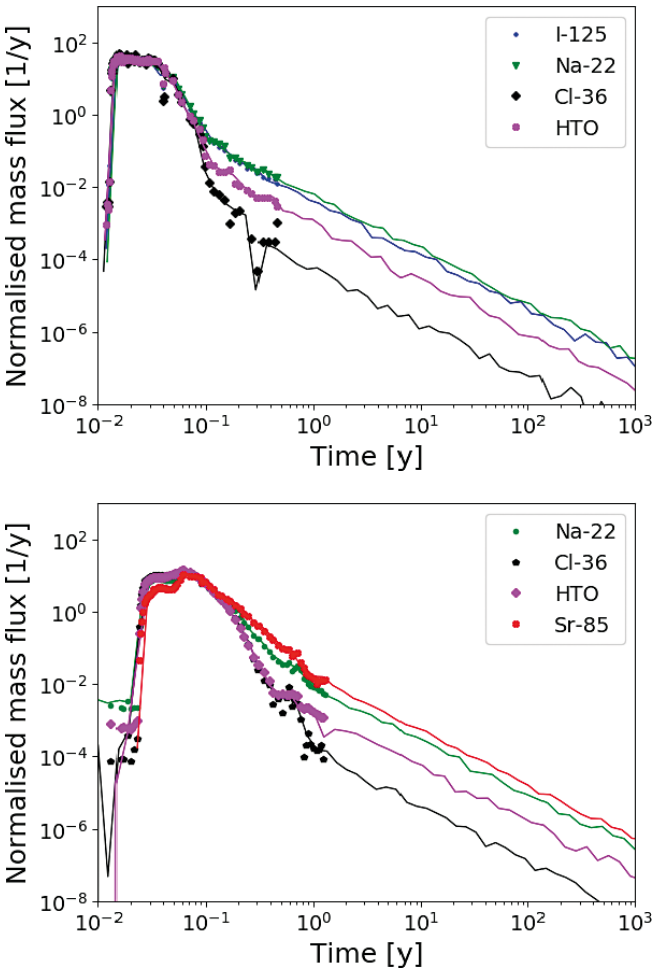

Figure A1-7. *Breakthrough curves computed using f_{ret}^{SM}. The results of the time-domain particle tracking calculations are shown with continuous lines whereas experimental data are shown with different markers.*

A1.4.3 Large-scale simulation

The retention time distributions extracted from WPDE1 (f_{ret}^{SM}) have been used to perform radionuclide transport calculations along a transport pathway made of 529 segments, where each segment is representative of the scale of the WPDE experiment (i.e., L = 1.9 m and $\tau = \tau_{th}$; see Table A1-1). The assumption here is that segment-to-segment retention properties are constant. The results of the upscaled solution are compared with simulations carried out along the same transport pathway using the parametric model (Equation A1-5) based on both κ_{est} and κ_{blind}. The cumulative groundwater travel time and transport resistance of both models is equal to $529 \times \tau_{th}$ y and $529 \times \beta_{th}$ y/m (Table A1-1). The results show that the breakthrough curves of Cl-36 computed with the parametric models are characterised by a later first-arrival time and have a noticeably lower peak value compared with the upscaled solution (see Figure A1-8). This difference is attributable to in-plane channelling effects that are not accounted for by the parametric models. The late-time behaviour is well approximated by both parametric-based models, meaning that (i) the parameters obtained from the laboratory experiments describe the low retention of Cl-36 well and (ii) κ_{est},extracted from the in situ experiment for Cl-36, provides a reliable estimation of retention processes in the rock matrix. Similar behaviour is observed for HTO, although, as already observed when interpreting the WPDE1 experiment, the parametric breakthrough curve based on κ_{blind} slightly over-estimates HTO retention in the matrix. When compared with Cl-36, a slightly lower mismatch between the peak values computed with the parametric models and the upscaled solution is observed. For the two sorbing nuclides (Na-22 and I-125), the parametric model based on κ_{est} provides an accurate approximation of the upscaled solution. This is because, at this large spatial-scale, breakthrough curves of sorbing nuclides are mostly controlled by mass exchange processes between the fracture and the matrix, and these processes are well captured by the estimation of κ based on the late-time experimental data. The significant over-estimation of Na-22 retention by the parametric model based on κ_{blind} is due to the previously discussed inconsistency between sorption distribution coefficients derived from batch experiments performed on crushed material and the actual retention properties observed in the field.

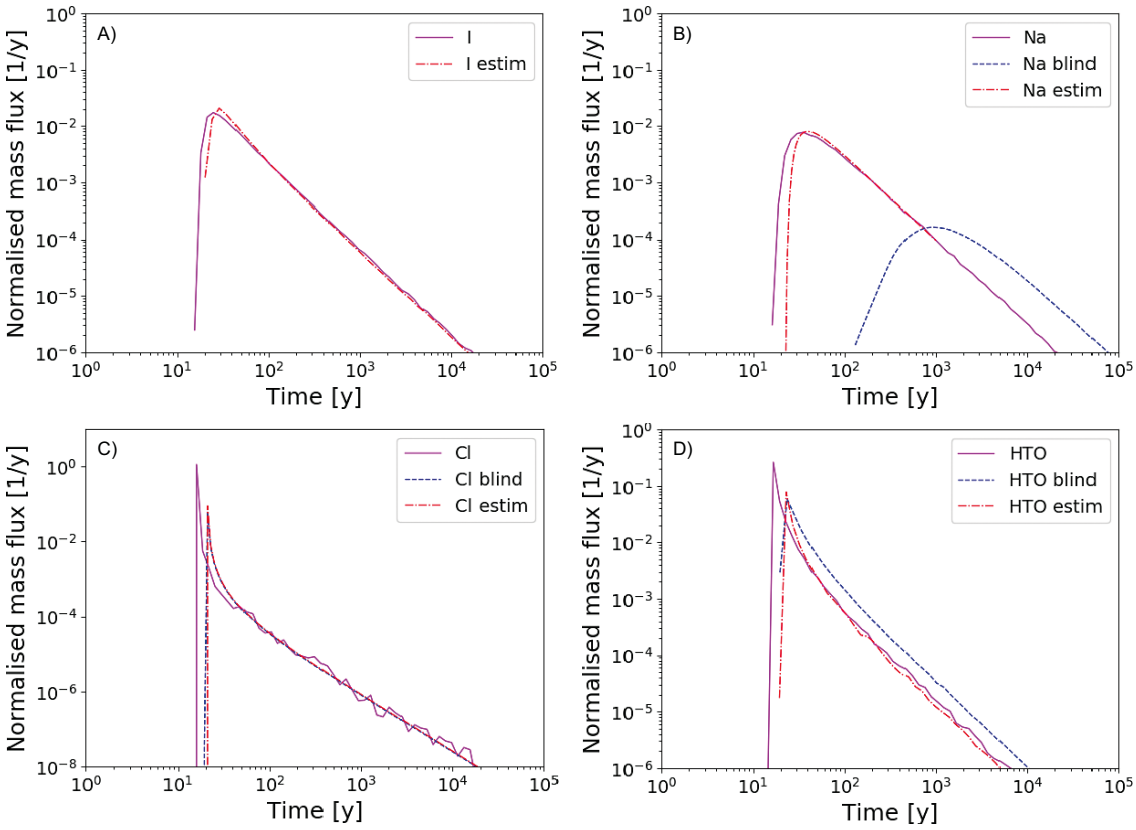

Figure A1-8. *Breakthrough curves computed using the upscaling procedure (Section A1.4.1) and f_{ret}^{SM} extracted from WPDE1 for (a) I-125, (b) Na-22, (c) Cl-36 and (d) HTO. The calculations are carried out along a transport pathway made of 529 segments. Each segment is characterised by the same in-plane processes as the WPDE1 experiment. The results of the upscaled solution are compared with simulations carried out along the same transport pathway using the parametric model (Equation A1-5) based on both κ_{est} and κ_{blind}.*

Analogous calculations are carried out using the retention time distributions extracted from WPDE2 (f_{ret}^{SM}). The only difference here is that the groundwater travel time of a single segment is taken from WPDE2 (see Table A1-1). In the related parametric simulations, the transport resistance is also taken from WPDE2. The results are qualitatively similar to those based on WPDE1, with the main difference being that here the agreement between the upscaled solution and the parametric model based on κ_{est} is better (see Figure A1-9). In fact, for HTO the match between the two breakthrough curves is very good. However, for Cl-36 the parametric model captures the first arrival well but still underestimates the peak value. This better agreement is related to the fact that the higher cumulative transport resistance of the models is based on WPDE2. Hence, as the transport resistance is an indicator of the scale of the problem, these results suggest that the effect of channelling is gradually smoothed out at increasingly larger distances from the source. The agreement between the upscaled solution and the parametric model based on κ_{est} is very good for the two sorbing nuclides, Na-22 and Sr-85. As in the previous set of calculations, the breakthrough curves of these two nuclides computed using κ_{blind} are significantly shifted to later times. This discrepancy is related to the discussed discrepancy between K_d values measured from crushed material in the laboratory and the actual sorption properties observed in the field. The spatial persistence of the channeling effects is studied in detail by assessing discrepancies in the first arrival time between the upscaled model and the parametric simulation based on κ_{est}. This is done by comparing the breakthrough curves obtained at different downstream distances from the source. At each downstream location the relative difference in the first arrival time is evaluated as $(t_{hom} - t_{het})/t_{het}$. Here, t_{hom} and t_{hom} [y] are arbitrarily set as equal to the time when 0.1 % of the total injected mass has reached the boundary. The results of these calculations are shown in Figure A1-10. Channeling effects are significant for both non-sorbing and sorbing nuclides at short downstream distances. These channeling effects lead to early breakthrough ($t_{het} < t_{hom}$). At increasingly larger distances, mass exchange processes become the dominant transport mechanism and the signature of channeling processes is progressively smeared out. The scale of this homogenization process is related to the specific nuclide retention; for strongly sorbing nuclides, such as Sr-85, the homogeneous behaviour is observed earlier.

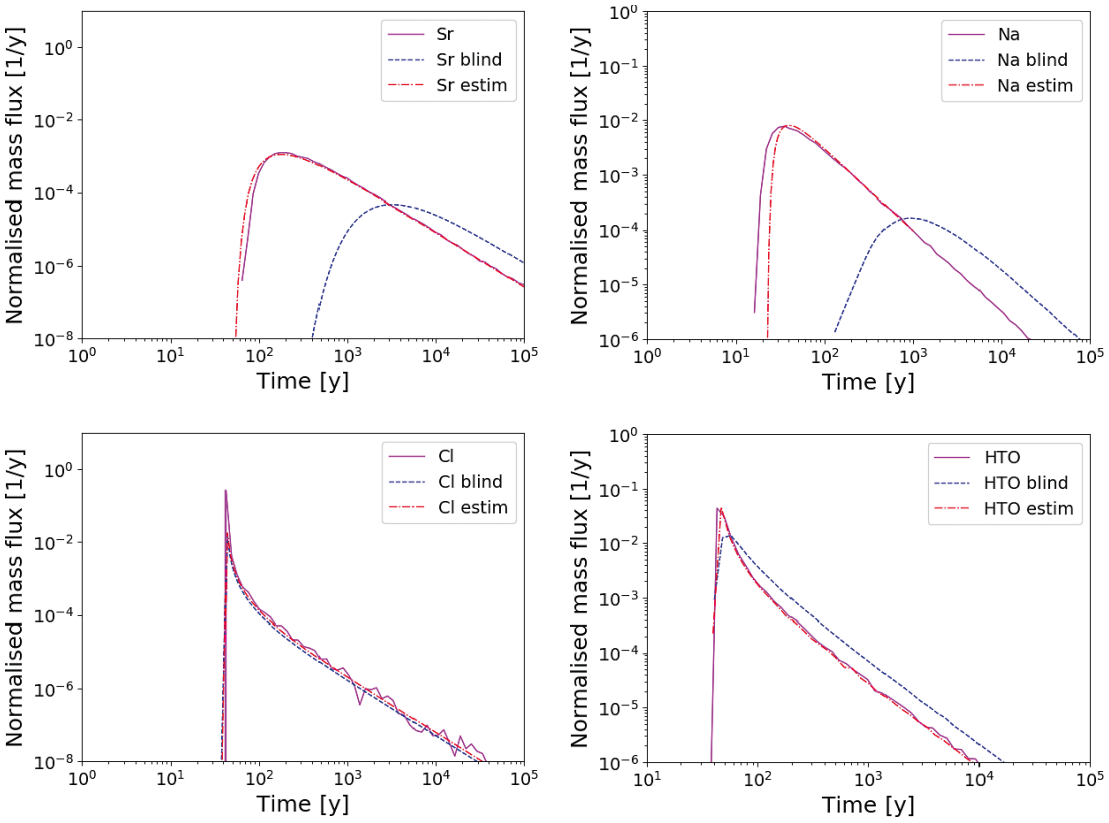

Figure A1-9. *Breakthrough curves computed using the upscaling procedure (section 5.4.1) and f_{ret}^{SM} extracted from WPDE2 for (a) Sr-85, (b) Na-22, (c) Cl-36 and (d) HTO. The calculations are carried out along a transport pathway made of 529 segments. Each segment is characterised by the same in-plane processes as the WPDE2 experiment. The results of the upscaled solution are compared with simulations carried out along the same transport pathway using the parametric model (Equation A1-5) based on both κ_{est} and κ_{blind}.*

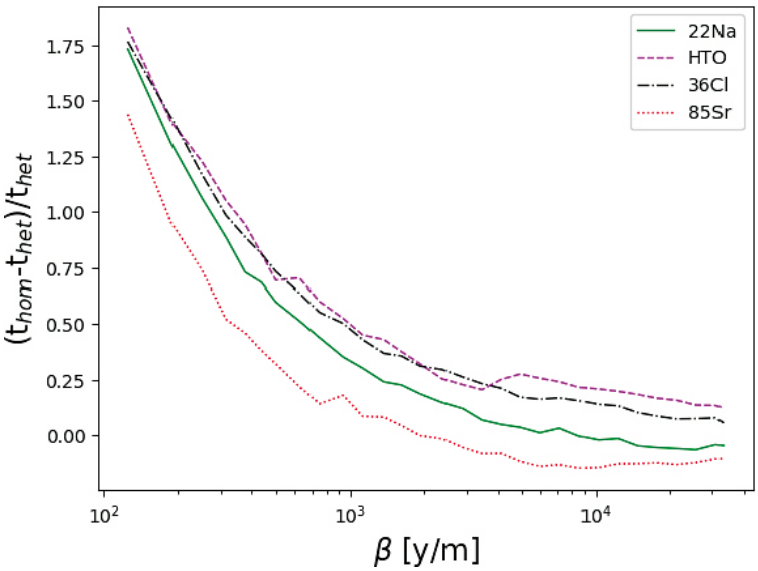

Figure A1-10. *Relative difference between the first arrival time (0.1 % of total injected mass) of the upscaled model and the parametric model (Equation A1-5) based on κ_{est} for the four considered nuclides. The parameters and the retention time distribution (f_{ret}^{SM}) are taken from WPDE2. The x-axis shows the cumulative transport resistance.*

A1.5 Discussion

The results presented and discussed in this work show that the effect of channeling on radionuclide transport, observed at a small scale in terms of an anomalous rising limb of the breakthrough curve with a very early arrival time, is increasingly smoothed out at progressively larger downstream distances. This evidence is consistent with recent results of Cvetkovic (2017), who showed that the coupling between water residence time and retention is weaker at longer time scales. Channeling is expected to have a direct influence on radionuclide retention through the transport resistance (Equation A1-1). However, this effect is surprisingly modest in both the experimental results and the upscaled large-scale calculations. This is due to compensating effects between the reduced groundwater travel time and the larger specific fracture surface area, which is made available by means of diffusion into stagnant water in the fracture and subsequent secondary diffusion into the rock matrix (Neretnieks 2006). Similar compensating effects were already pointed out in recent synthetic simulations (Trinchero et al. 2020b).

The upscaled simulations presented in this work are based on idealised transport pathways that do not account for segment-to-segment longitudinal variability. In real fractured systems, transport pathways exhibit strong longitudinal heterogeneity, due to changes in fracture openings caused by, for example, differences in mechanical stress. In a recent work, Trinchero et al. (2020a) have shown that longitudinally homogeneous and heterogeneous models do not significantly differ in terms of homogenisation of the heterogeneous signal at downstream distances. Hence, the conclusions drawn in this work with the upscaled models are deemed to be generic and valid for realistic site-scale conditions.

A1.6 Summary and conclusions

Natural fracture apertures are produced by geochemical and mechanical processes (e.g. Detwiler 2008, Zou et al. 2017). This results in a very complex and highly heterogeneous distribution of fracture openings. This complexity, which has a strong impact on groundwater flow and transport (Tsang and Neretnieks 1998), makes it difficult to interpret field tracer tests. A field water phase diffusion experiment (WPDE) was recently designed and executed at ONKALO (Finland), with the objective of placing the focus on retention processes in the matrix. To this end, a geometrically well-defined artificial fracture was obtained by placing a cylindrical dummy co-axially within a packed-off section of a drillhole. Despite state-of-the-art execution of the experiment and well controlled conditions, the resulting nuclide breakthrough curves were characterised by an anomalous early breakthrough and a flat peak. These effects were attributed to in-plane channelling processes, caused by small

irregularities in the artificial fracture. It turns out that the WPDE experiment provides a unique dataset to evaluate the mutual interplay between in-plane channelling processes, matrix diffusion and sorption in the matrix.

By using an approach based on retention time distribution functions, we have upscaled the results of WPDE and assessed the implication of channelling and retention processes in the matrix at different spatial scales. The effect of channelling is shown to be significant at the scale of the in situ experiment but it progressively vanishes at larger scales, where the nuclide breakthrough curve is mostly controlled by mass-exchange processes between the fracture and the rock matrix. This homogenisation occurs at shorter scales for sorbing nuclides. We have also shown that the late-time part of the breakthrough curve can be used to infer a lumped product of the material parameter group and the transport resistance. This can in turn be used by a parametric model to successfully describe the large-scale nuclide breakthrough curve. Parametric-based calculations using matrix parameters obtained from laboratory experiments also provide a good approximation of the upscaled solution for non-sorbing nuclides, however, they significantly overestimate retention for sorbing nuclides. This over-estimation is related to observed inconsistencies between sorption distribution coefficients inferred from laboratory experiments performed on crushed rock and the actual retention observed in the field (Winberg et al. 2000, Byegård et al. 2017, Voutilainen et al. 2019). Another point worth noting is the estimation of parametric values based on the late-time behaviour of the breakthrough curves. Equation A1-8 can be used to infer the lumped product of the material parameter.

A1.7 Additional – Results for the evaluation

As explained in Section A1.2, this work has been inspired and motivated by the general objectives of Task 9D. However, it has not strictly followed the recommendations for model parameterisation provided in the task description (Appendix 5). This is because the primary models presented here are based on a non-parameteric approach. In fact, the large-scale upscaled models (Section A1.4.3) are based on idealised transport pathways built upon minimum spatial units (fracture segments) equal to the experimental section of WPDE. Parametric models, used to interpret and analyse upscaled results, are also implemented in a similar fashion by assuming $\tau = N_{seg} \times \tau_{th}$ and $\beta = N_{seg} \times \beta_{th}$, where N_{seg} is the number of segments and τ_{th} and β_{th} are the theoretical values in WPDE. In the work presented in the main part of this report, which is in turn based on the manuscript of Trinchero et al. (2020c), $N_{seg} = 529$.

To allow for comparison here, the parametric calculations of Section A1.4.3 are repeated using $N_{seg} = 800$ and τ_{th} and β_{th} based on WPDE-2 (see Table A1-1). The material parameter group is based on κ_{blind} (see Table A1-3). The resulting cumulative groundwater travel time and transport resistance (62.4 y and 50 080.0 y/m, respectively) are very close to the parameters suggested in Appendix 5. HTO should be considered as a proxy for A nuclide (Table A5-1 in Appendix 5 whereas Na-22 and Sr-85 should be regarded as proxies for nuclide C (moderately-sorbing). Cl-36 could be a proxy for an anionic species (not included in Appendix 5). The results of the simulations are shown in Figure A1-11.

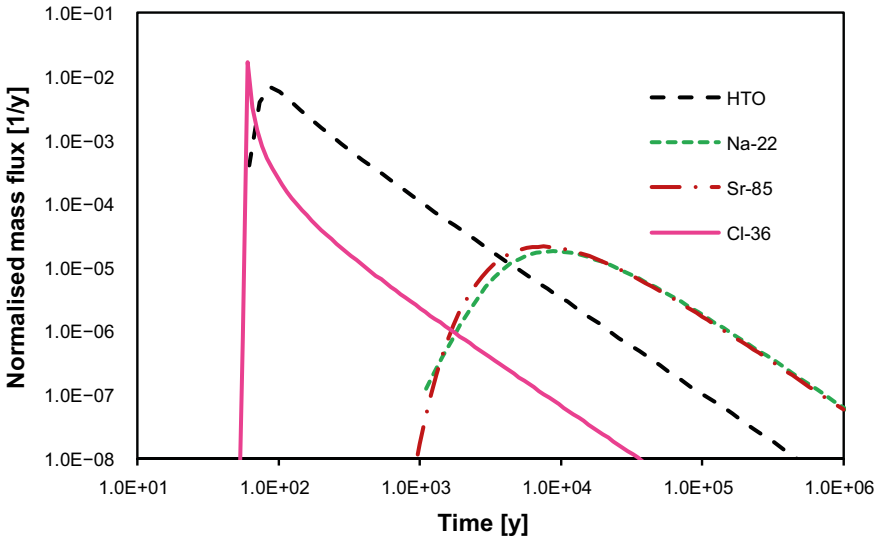

Figure A1-11. *Breakthrough curves computed using the parametric model (Equation A1-5) based on κ_{blind}. The calculations are carried out using a transport pathway made of 800 segments. Each segment is characterised by the same in-plane processes of the WPDE2 experiment.*

Appendix 2

Contribution from the Czech teams – Solution of the transport task at the scale of a SA (Task 9D)

M Hokr, J Říha
Technical University of Liberec

V Havlová, D Trpkošová
ÚJV Řež

A Vetešník, D Reimitz, J Višňák, D Vopálka
FJFI ČVUT (Czech Technical University in Prague, Faculty of Nuclear Sciences and Physical Engineering)

L Gvoždík, M Milický, M Polák
PROGEO s.r.o.

December 2020

A2.1 Introduction

The aim of subtask 9D is to extrapolate the models and results from the scale of in situ experiments to the scale and conditions considered in a safety assessment (SA). The configuration of the model is based on Task 9A and in sub-variants the properties and phenomena important in a real SA are added gradually. In the original plan issued by GWFTS, the basic ideas of the four variants were presented. In the end two variants (9D-1 and 9D-2) were implemented by both the Czech teams, authors of this report, and the project as a whole (Hokr et al. 2021).

Due to that the contract of the Czech teams ended before the completion of Task 9D, only a part of the assignment was performed. In addition, the comparisons of the results from the Czech co-authors are elaborated for the needs of SURAO.

A2.2 Summary of the task description and the data

The task is based on synthetic simplified geometry (Figure A2-1), with realistic parameters corresponding to the conditions of transport from the repository to the "interface with the biosphere", with a 1 km-long "fracture". Transport through one fracture (advection and hydrodynamic dispersion), retention processes in the rock matrix (diffusion, sorption) and radioactive decay are considered. In addition to the scale, the inclusion of decay marks a significant change from Task 9A. Two variants distinguish cases of fictitious single tracers and a simplified decay series of uranium. The task description is detailed in Appendix 5.

The relationship of the tasks at different scales, the in situ WPDE experiment (9A) and the safety assessment (9D) is expressed by the parameters in Table A2-1. The retardation effect on transport is expressed by the F factor, which is the ratio of the flow wetted surface of the fracture to the flow rate expressed in a/m. Task 9D is specified with the F-value of the SR-Site study, which is approximately two orders of magnitude higher than the WPDE experiment. The transverse area of the fracture in the WPDE (annulus) is 2.17×10^{-4} m^2, which corresponds to the "flat" configuration of Task 9D:

- This is equivalent to a fracture width of 177 mm and an aperture of 1.22 mm for diffusion into the matrix on only one side of the fracture, (used for the models of TUL and PROGEO with explicit geometry).
- This is equivalent to a fracture width of 88 mm and 2.44 mm for diffusion into the matrix on both sides of the fracture (used for the models produced by CTU and ÚJV, using the "built-in" analytical solution of diffusion in the pipe element of GoldSim).

As the task description does not state a specific way of modelling the dispersion in the fracture, the default value of the Peclet number Pe = 10 is proposed, which corresponds to a standard model of hydrodynamic dispersion and a task dimension of longitudinal dispersivity of 100 m.

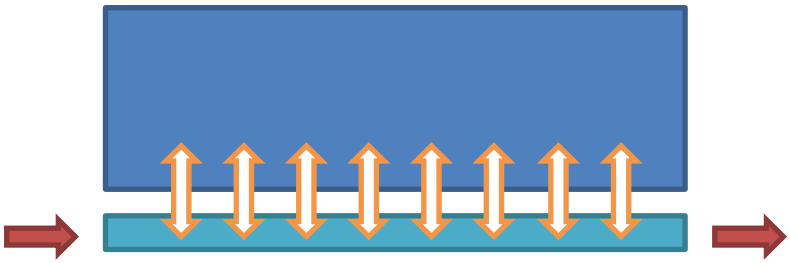

Figure A2-1. *Diagram of diffusive transport into the matrix in a scale corresponding to the safety calculation.*

The transverse dimension of the matrix domain is also not specified. As a result, the choice of finite or infinite distance is determined by the model used or a specific distance.

Rock matrix parameters are based on Task 9A and VGN rock is considered the dominant type in the experimental series REPRO. Specific parameters are given for the individual tracers for variants 9D-1 and 9D-2 in the subsections below. In both cases, anion exclusion is considered (i.e., the effective diffusion coefficient is an order of magnitude lower with a corresponding lower "transport porosity" (pore volume available for the tracer particles)).

Table A2-1. Parameters of flow and interaction of the rock matrix for Task 9D in the context of Task 9A (WPDE).

	WPDE-1	WPDE-2	SA Task 9D
q (m^3/a)	1.05×10^{-2}	5.26×10^{-3}	3.55×10^{-3}
v (m/a)	48.48	24.24	16.36
t_w (a)	0.0393	0.0786	61.12
F (a/m)	32.14	64.29	5×10^4

A2.2.1 Step 9D-1 – fictitious tracers

The task as specified above is defined according to Appendix 5 for four dummy tracers (with parameters representing model cases of real radionuclides) marked A–D (Table A2-2) and four variants of other parameters marked a–d (Table A2-4). Of these, only a, which has a pulse input (1 mol/a) of 1 000 years duration and no decay, and b, which has a continuous inlet flow of 1 MBq/a and decay, were considered. The flow values are only technical; given the considered linearity of the model, they do not qualitatively affect the result.

The tracers primarily represent cases of sorption of varying size (Table A2-2) while the non-sorbing tracer A corresponds to the anion, with parameters considered for chlorine in Task 9A. The available porosity for tracer A is considered as 0.000436, as it was in Task 9A, rather than as the ratio of the D_e values as mentioned in the task description (Appendix 5). The half-life of each tracer increases sequentially from A to D. The density of rock was 2.741 kg/m^3.

Normalised breakthrough curves (time course of mass flow or output activity flow normalised by the input flow) and transverse profiles on the middle of the length of the task, at times that are different for each tracer, are prescribed as outputs (Table A2-3). The profile should be determined as total concentration (variant a) or activity (variant b) at the points of the profile, including both dissolved and sorbed forms. The analysis of the first versions of the models (carried out by the investigators) contributed to the selection of the given times, which are more suitable than those originally determined (this was included in the cited revision of the task description).

Table A2-2. Parameters of model tracers A–D according to the task description, the porosity corresponds to the relative volume of rock pores available for the given tracer.

Tracer	K_d (m^3/kg)	D_e (m^2/s)	$T_{1/2}$ (a)	Porosity (-)
A (non-sorbing)	0	5×10^{-15}	20	0.000436
B (weakly sorbing)	10^{-4}	1.83×10^{-13}	1 000	0.0065
C (moderately sorbing)	10^{-3}	1.83×10^{-13}	10 000	0.0065
D (strongly sorbing)	0.1	1.83×10^{-13}	1 000 000	0.0065

Table A2-3. Times for profile output.

Tracer	Time for profile output [a]
A (non-sorbing)	500
B (weakly sorbing)	5 000
C (moderately sorbing)	50 000
D (strongly sorbing)	500 000

Table A2-4. Variants of the model according to the task description (calculations are performed for the first two).

Variant	Decay	Input boundary condition	Parameters
“a”	No	Pulse	Constant
“b”	Yes	Continuous	Constant
“*c*”	*No*	*Pulse*	*Variable*
“*d*”	*Yes*	*Continuous*	*Variable*

A2.2.2 Step 9D-2 – decay series

The second variant 9D-2 considers real radionuclides bound together by a decay series. A simplified series of six radionuclides, starting with U-238, was designed by the task proposer for the model task. Connection to the general decay process is shown in Figure A2-2. The half-life decreases with the sequence of products in the chain, so secular equilibrium can be assumed based on the rates of ingrowth and decay.

A continuous inflow of only U-238 is specified, with an activity flow of 1 MBq/a (again, this is only a technical choice). The radionuclides are assigned transport parameters according to Table A2-5.

Again, the breakthrough curves of the flow activity of the individual tracers normalised by the input flow of U-238 and the transverse profiles, evaluated in half of the length of the model at 100 ka, are required as outputs.

Table A2-5. Specified parameters of the considered radionuclides (according to Appendix 5 where the origin of the data is also explained).

Radionuclide	Dominant species	K_d (m^3/kg)	D_e (m^2/s)	$t_{½}$ (a)
U-238	$Ca_2UO_2(CO_3)_3$	8.0×10^{-2}	1.83×10^{-13}	4.47×10^{9}
U-234	$Ca_2UO_2(CO_3)_3$	8.0×10^{-2}	1.83×10^{-13}	2.45×10^{5}
Th-230	$Th(OH)_2(CO_3)_2^{2-}$	8	5×10^{-15}	7.54×10^{4}
Ra-226	Ra^{2+}	6.0×10^{-2}	1.83×10^{-13}	1.6×10^{3}
Pb-210	$PbCl^{+}$	2	1.83×10^{-13}	2.22×10^{1}
Po-210	$PoO(OH)_2$	2	1.83×10^{-13}	3.79×10^{-1}

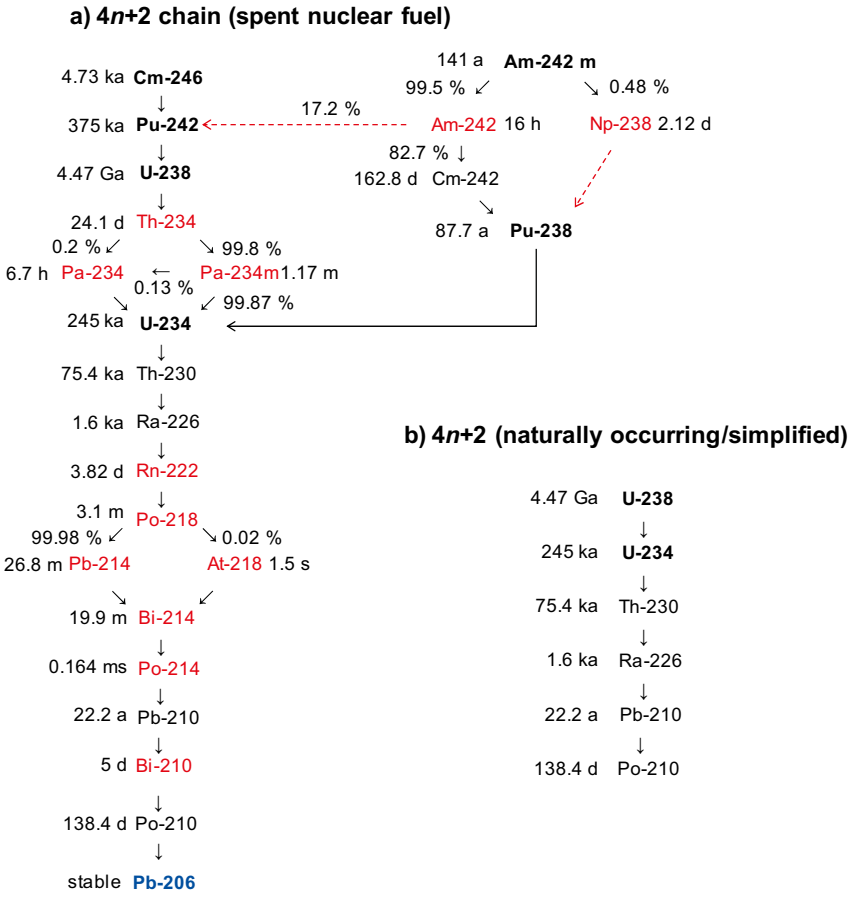

Figure A2-2. *Derivation of a simplified decay series (taken from Appendix 9).*

A2.3 Solution in Flow123d (TUL)

The concept of the model is based on a combination of a 1D fracture and a 2D rock matrix. The imaginary third dimension of the rock matrix (Flow123d input) is equal to 0.177 m, which ensures the correct value of the wetted surface (according to the task description). The fracture flow area is 217 mm^2, which corresponds to an aperture of 1.226 mm.

The fracture length is 1 000 m and the rock matrix thickness is 1 m (10 m in some calculations). The rock matrix is divided into layers of different thicknesses. The thinnest layer is closest to the fracture, and the thickness increases as the distance from the fracture increases. This was introduced to ensure finer discretisation near the fracture/rock interface.

The hydraulic conductivity in the fracture was calculated from the cubic law. The hydraulic conductivity in the rock matrix was calculated from the known permeability value (taken from the Task 9A task description). Parameters and boundary conditions of the flow are summarised in Table A2-6. The table shows that the resulting velocity (flux) in the fracture corresponds to the values given in the task description.

A2.3.1 Task 9D-1

The transport model parameters are used according to Table A2-2. Other parameters specific for Flow123d are summarised in Table A2-6 and Table A2-7 (where a fracture and a matrix are additionally distinguished). The boundary condition of the transport was a constant mass flow of 1 kg/year (just a choice for convenience) on the inflow into the fracture, which does not affect the normalised breakthrough curves and the transverse profiles were converted to equivalent of the mass or activity flux in the task definition using the specific activity or molar weight.

Table A2-6. Task9D – Flow123d – parameters and Boundary Conditions (BC) of the flow model.

Hydraulic conductivity in the fracture	39.447×10^{-6} m/a
Hydraulic conductivity in the rock	3.096×10^{-5} m/a
BC “inlet”	Total flow 16.36 m/a
BC “outlet”	Dirichlet Φ = 0 m
BC “remainder”	Homogeneous Neumann (zero flow)
Flow/rate	3.55×10^{-3} m^3/a ~ 16.36 m/a

Table A2-7. Task9D – Flow123d – transport model parameters.

Item	Rock matrix	Fracture
Porosity tracer A	4.3637×10^{-4}	1
Porosity tracer B, C and D	6.5×10^{-3}	1
Longitudinal dispersivity	0 m	100 m
Transverse dispersivity	0 m	10 m

The results of transport simulations, in the form of normalised breakthrough curves and concentration profiles at specified times in a line perpendicular to a fracture halfway through its length, are part of a comparison in Section A2.7.

A2.3.2 Task 9D-2

The transport model parameters are summarised in Table A2-5. The results of transport simulations in the form of normalised breakthrough curves are part of the cross-comparison in Section A2.7.

The breakthrough curves of the most highly sorbing members of the decay series are significantly different from the breakthrough curves produced by other investigators. Using the exclusion method, we determined that this is due to spatial discretisation of the rock matrix near the fracture/rock interface.

A2.4 Variants of the solution at CTU

CTU perceived Task 9D as the application of results obtained in previous tasks by modelling in situ experiments to the solution of transport tasks, corresponding to scenarios and scales typical for safety assessments. In accordance with the task description, we considered the model of an idealised fracture in the form of flat plates bounded on both sides by a homogeneous isotropic rock matrix of unlimited thickness (Figure A2-3).

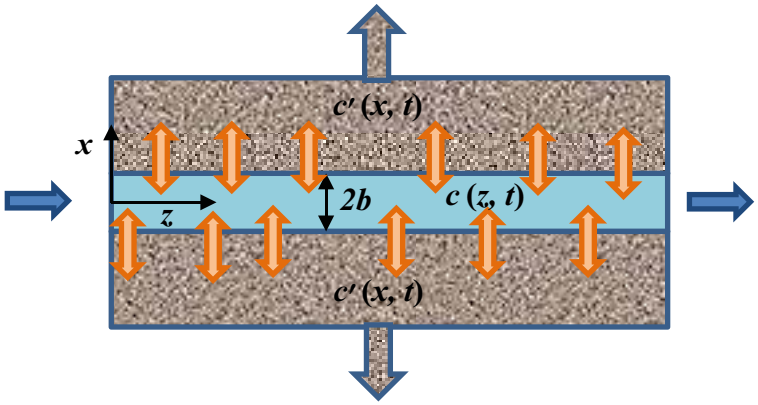

Figure A2-3. *Diagram of transport in an idealised fracture with aperture 2b; the blue arrows indicate the direction of advective flow, orange arrows indicate diffusion into the matrix, c(z, t) indicates the concentration of radionuclide in the flowing water, and c′(x, z, t) indicates the concentration in the pore water of the rock matrix.*

A2.4.1 Analytical solution

The transport of radionuclides in this idealised fracture may be described using two sets of partial differential equations (Sudicky and Frind 1982). The first set of equations describes advective transport along the fracture in the direction of the z axis

$$\begin{gathered}\frac{\partial c_1}{\partial t}+v\frac{\partial c_1}{\partial z}+\lambda_1 c_1-\left.\frac{\varepsilon D_{p,1}}{b}\frac{\partial c_1'}{\partial x}\right|_{x=b}=0\\ \vdots\\ \frac{\partial c_n}{\partial t}+v\frac{\partial c_n}{\partial z}+\lambda_n c_i-\lambda_{n-1}c_{n-1}-\left.\frac{\varepsilon D_{p,n}}{b}\frac{\partial c_n'}{\partial x}\right|_{x=b}=0, 0\le z\le\infty.\end{gathered} \tag{A2-1}$$

where x,z are spatial variables, t is time change, $c_i = c_i(z,t)$ is the concentration of i-th radionuclide ($i \in [1,n]$) in the aqueous medium of the fracture, $c'_i = c'_i(x,z,t)$ is the concentration of the i-th radionuclide in the pore water of the rock matrix, v is the flow velocity in the fracture, λ_i is the decay constant of i-th radionuclide, ε is the porosity of the rock matrix, $2b$ is the aperture of the fracture $D_{p,i} = \tau D_{w,i}$ is the diffusion coefficient of the i-th radionuclide in the pores, τ is the shape/geometric factor, and $D_{w,i}$ is the diffusion coefficient of the i-th radionuclide in water.

The second set of equations describes diffusion and sorption in the rock matrix in the perpendicular direction, in the direction of the x axis

$$\begin{gathered}\frac{\partial c'_1}{\partial t}-\frac{D_{p,1}}{R_1}\frac{\partial^2 c'_1}{\partial x^2}+\lambda_1 c'_1=0\\ \vdots\\ \frac{\partial c'_n}{\partial t}-\frac{D_{p,n}}{R_n}\frac{\partial^2 c'_n}{\partial x^2}+\lambda_n c_n-\frac{R_{n-1}\lambda_{n-1}c'_{n-1}}{R_n}=0, b\le x\le\infty,\end{gathered} \tag{A2-2}$$

where $R_i = 1 + (\rho_d/\varepsilon K_{d,i})$ is the retardation coefficient of the i-th radionuclide, ρ_d is the bulk density of the material, and $K_{d,i}$ is the equilibrium distribution coefficient of the i-th radionuclide.

The following initial and boundary conditions were considered

$$\begin{gathered}c_i(z,0)=0,\ c_i(0,t)=c_{o,i}\delta(t)\\ c_i'(x,z,0)=0,\ \ c_i'(b,z,t)=c_i(z,t), c_i'(\infty,z,0)=0.\end{gathered} \tag{A2-3}$$

The analytical solution of this transport task for the concentration c_1 of the first radionuclide of the decay series can be written in the form (Sudicky and Frind 1982)

$$\begin{gathered}c_1(z,t)=\theta(t-T)c_{0.1}\frac{\gamma_1 z}{2\pi^{1/2}T^{3/2}}exp\left(-\frac{(\gamma_1 z)^2}{4T}-\lambda_1 t\right)\\ T=t-\frac{z}{v},\ \gamma_1=\frac{\epsilon\sqrt{R_1 D_{p,1}}}{bv},\end{gathered} \tag{A2-4}$$

where $\theta(t)$ is the Heaviside step function ($\theta(t) = 0$, for $t \le 0$; $\theta(t) = 1$ for $t > 1$). For the other members of the decay series, it is not possible to explicitly express the dependence c_i on z and t due to the complexity of the calculation of the inverse Laplace transform.

We used Equation (A2-4) for c_1 to validate the model in GoldSim (GS), specifically in order to solve transport problems for four fictitious radionuclides. Equation (A2-4) describes the time dependence of the fracture end concentration in response to the Dirac unit impulse (initial and boundary condi-

tions shown in Equation A2-3). To calculate the response for pulse flow for 1 000 years, we created a function in MATLAB® (R2016b) that first calculated the Equation (A2-4) for the specified transport parameters and then calculated the convolution (MATLAB conv) with the rectangular function

$$U(t) = \begin{cases} 1; \text{for } 0 \le t \le 1000, \\ 0; \text{for } t < 0, \text{or } t \ge 1000. \end{cases}$$

We also used the analytical solution to design a further extension of the transport model in the framework of Task 9D. It has been shown in Barten (1996) that transport by a system of fractures connected in series can also be described by Equation (A2-4), in which the parameters T and γ_1 are given as the sum of the parameters of the fractures. Therefore, we think that the heterogeneous nature of the fracture network should be represented by a more complex fracture system that will consist of interconnected parallel pathways.

A2.4.2 Model in GoldSim

Figure A2-4 includes a diagram of the Task 9D model in GoldSim. The transport part of the model consists of five components. The selector (FlInjection) component is used to specify a time-limited pulse flow, two pipe pathway components (Pipe1 and Pipe2) represent a fracture with a rock matrix, the container component (Matrix Diffusion) contains a planar network of 98 × 1 Cell pathways and calculates cross-sectional concentration profiles of radionuclides in the rock matrix in the middle of the fracture length. The pipe pathway component contains the concentration of radionuclides in the water at the end of the fracture as the output. It does not allow the explicit calculation of the concentration profile in the rock matrix. Therefore, we split the fracture into two equal lengths and used the concentration at the output of the first pipe pathway component (Pipe1) as a boundary condition for the cell pathway network. In order to use the model for non-sorbing and sorbing radionuclides simultaneously, we chose a network of 98 Cell pathway elements at an interval of (0, 10) [m] with a non-equidistant step extending from the fracture towards the matrix to calculate the concentration profile. We created two models in GoldSim, the first to solve the transport problem for four fictitious radionuclides, and the second to solve the problem for the uranium (4n+2) decay series.

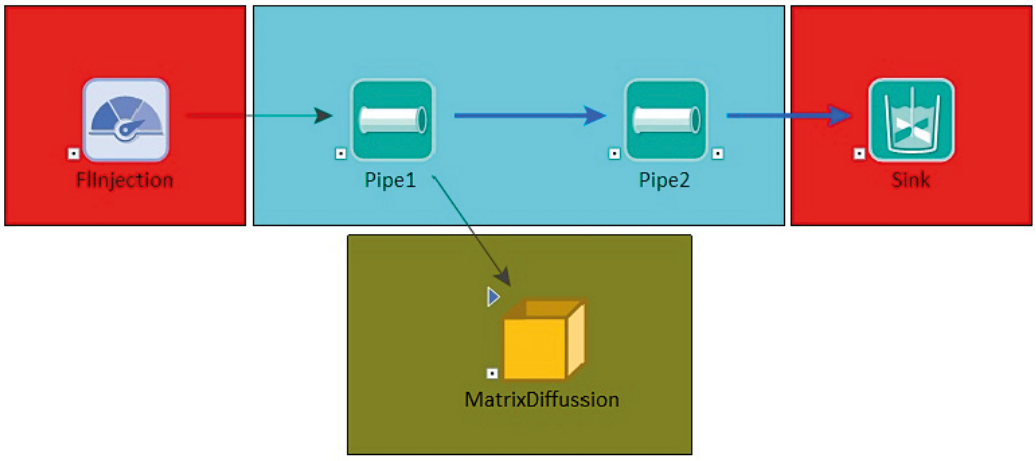

Figure A2-4. *Diagram of the transport part of the 9D model in GoldSim.*

A2.5 Solution in GoldSim (ÚJV)

GoldSim version 12.0 was used to solve Task9D by the team at ÚJV Řežs. The rock environment is considered to be homogeneous with isotropic properties. The pipe pathway component was used for the solution of the task and a fracture of 1 000 m × 0.088 m × 0.00244 m (length × width × transport aperture) was simulated (Figure A2-5). The fracture is simulated as open, without mineral infill. In the fracture, a dispersion of 10 % of the scale of the task was considered.

The following processes are simulated in the fracture:

- Advective transport;
- Longitudinal dispersion;
- Diffusion into rock matrix (exchange between mobile and immobile zones);
- Sorption;
- Radioactive decay for selected tracers.

The input was simulated in two ways, both as a 1 000-year pulse and as a constant input throughout the simulation. A groundwater flow rate of 0.00355 m^3/year was considered in the fracture (see Table A2-1). The parameters of the transport model were taken from the task description and are given in Table A2-2.

Task 9D2 adopts the same model geometry used in Task 9D, however it differs in terms of its considered source, U-238. Its products decay according to the series shown in Figure A2-2.The injected amount of U-238 was 1 Bq/year. The parameters of the transport model were taken from the Task Description and are given in Table A2-5.

Figure A2-5. *Method of fracture simulation in GoldSim, diagram of the mathematical model.*

A2.6 Solution in MT3D (PROGEO)

At PROGEO, a selected part of the tasks was simulated during the solution of Task 9D:

- Task 9D 1 for tracers A and C and for two boundary conditions “a” (pulse) and “b” (constant source with radioactive decay);
- Task 9D 2 with the U-238 decay series.

MODFLOW2005 (for flow calculation) and MT3DMS and MT3D-USGS (for transport calculation) were used for the solution of Task 9D, as well as for the solution of Task 9A, on which Task 9D is based. The conceptual model used in the solution of Task 9D is similar. Task 9D is solved by a one-layer model in 2D, with a model domain formed by a rectangular grid of computational cells (see Figure A2-6). The fracture is entered in the upper row of the computational cells, i.e., it is oriented in the direction of the *x*-axis and diffusion into the rock matrix is in the direction of the *y*-axis. The length of the model domain is 1 000 m (corresponding to the fracture length), and the width is 1 m (corresponding to the thickness of the rock matrix). The thickness of the single-layer model is 0.177 m (corresponding to the TUL concept). The length of the computational cells in the fracture direction is a constant 1 m (i.e., a total of 1 000 columns). The width of the first row of the computational cells representing the fracture is 1.22 mm (corresponding to the fracture aperture). The width of the computational cells representing the rock matrix gradually increases from 0.1 mm to 170 mm, as distance from the fracture increases (this increase occurs over 41 rows in total). The rock matrix cells that are in contact with the fracture have a very narrow width. This is because, as established in the solution of Task 9A, it provides more accurate results of the transport simulation, especially in the case of sorbing tracers. Time steps are set in a geometric series, starting at 0.001 years and increasing with a quotient of 1.05. The time step is restarted when the input concentration is changed.

Flow values of the fractures and transport parameters of the rock matrix (porosity, diffusion coefficients, sorption coefficients and half-life) are taken from the joint task description and are the same as those used by co-investigators.

The main aim of the simulation of Task 9D-1 in MODFLOW2005 and MT3DMS was to establish the possibility of performing a type of task (a combination of fracture flow and diffusion into the rock matrix) in programs that have been used in PROGEO for a long time, and with which we have successfully solved real hydrogeological tasks.

Given that Task 9A was also solved at PROGEO, the aim was to verify the consistency of small-scale simulation results (Task 9A with a fracture length of 1.9 m) and then upscale to a regional scale task, albeit simplified to a single fracture (Task 9D with fracture length of 1 000 m).

The motivation of the solution of Task 9D-2 was to verify and compare the results of the radionuclide decay series simulation in the MT3D USGS program, as the decay series simulation is a new feature which was only added in 2016 (earlier versions of the program, e.g., MT3DMS, did not allow this solution).

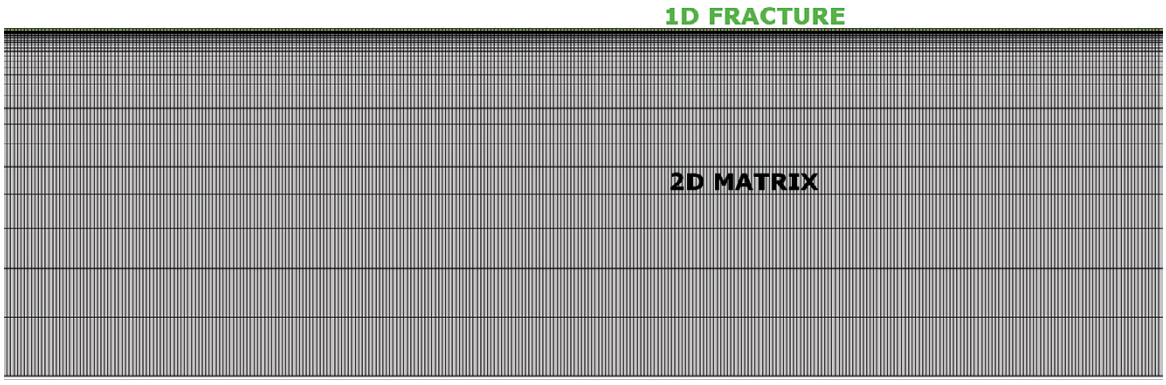

Figure A2-6. *Task 9D – discretisation of the model domain in the PROGEO solution.*

A2.7 Comparison of the solutions

A2.7.1 Task 9D-1

The breakthrough curves for the pulse input variants are shown in both the linear and logarithmic axes of the concentration, in order to see the shape of the decreasing characteristic of diffusion into the matrix. The graphs in Figure A2-7, Figure A2-8, Figure A2-9 and Figure A2-10 show the individual tracers A–D. The comparison includes three (B, D) or four (A, C) numerical calculations, an analytical solution without dispersion or a model without dispersion (B, D), allowing for several partial evaluations.

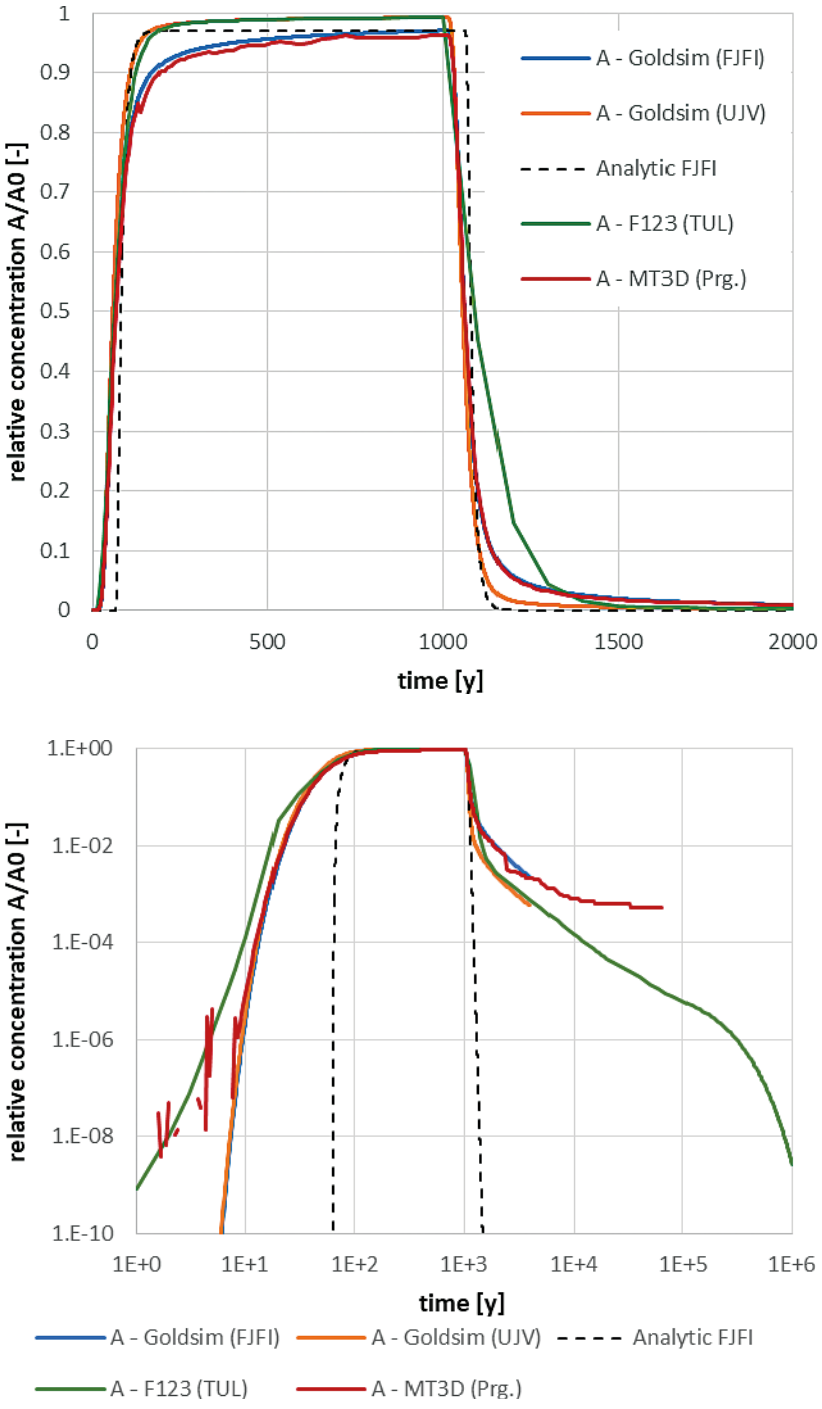

Figure A2-7. *Comparison of solution 9D-1-a breakthrough curves plotted against two types of axis scale for tracer A (four models), in this case, the analytical solution is for the advection-only model (without the matrix diffusion).*

The breakthrough curves are in qualitative agreement among the model variants for each tracer. Some deviations occur either on the linear axis only or on the logarithmic axis only. The most obvious effect is the course discretisation of Flow123d, while MT3D for the same conceptual model has a better agreement with the more accurate GoldSim. The deviations of the trend in the slope of the curve in the logarithmic axis are related to the different matrix thicknesses for each model, as demonstrated by the comparison in Section A2.8, and a similar comparison in Task 9A.

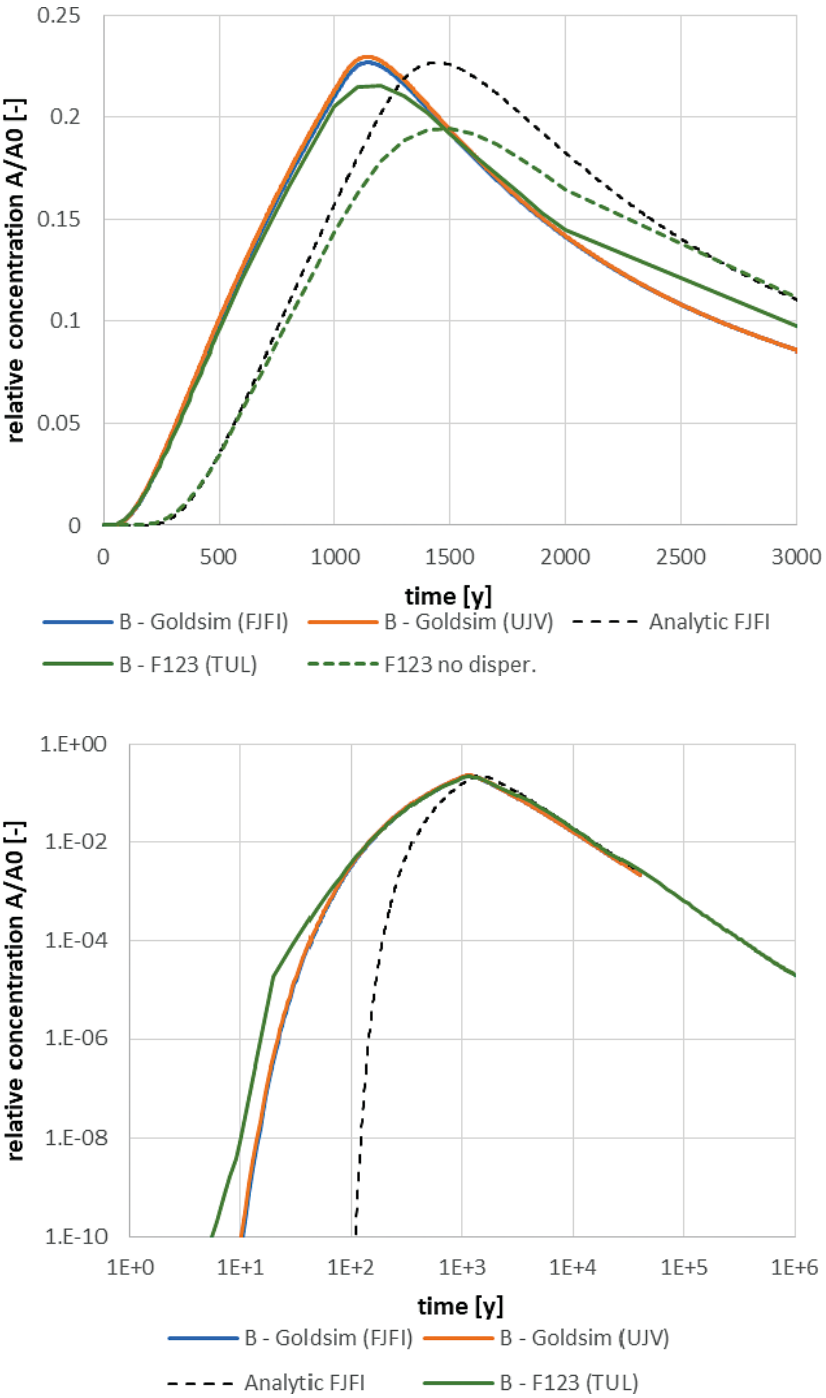

Figure A2-8. *Comparison of solution 9D-1-a breakthrough curves plotted against two types of axis scale for tracer B (three models and variants without dispersion corresponding to the analytical solution).*

The shift of the analytical solution compared with all models of sorbing tracers B, C and D may seem surprising. However, this phenomenon has also been observed for Task 9A, in terms of sensitivity to dispersion in the fracture. The dispersion effect is also documented here by comparing the Flow123d solution with zero dispersion for tracers B and D, where the same shift occurs as in the analytical solution (however, numerical diffusions occur at different peak heights).

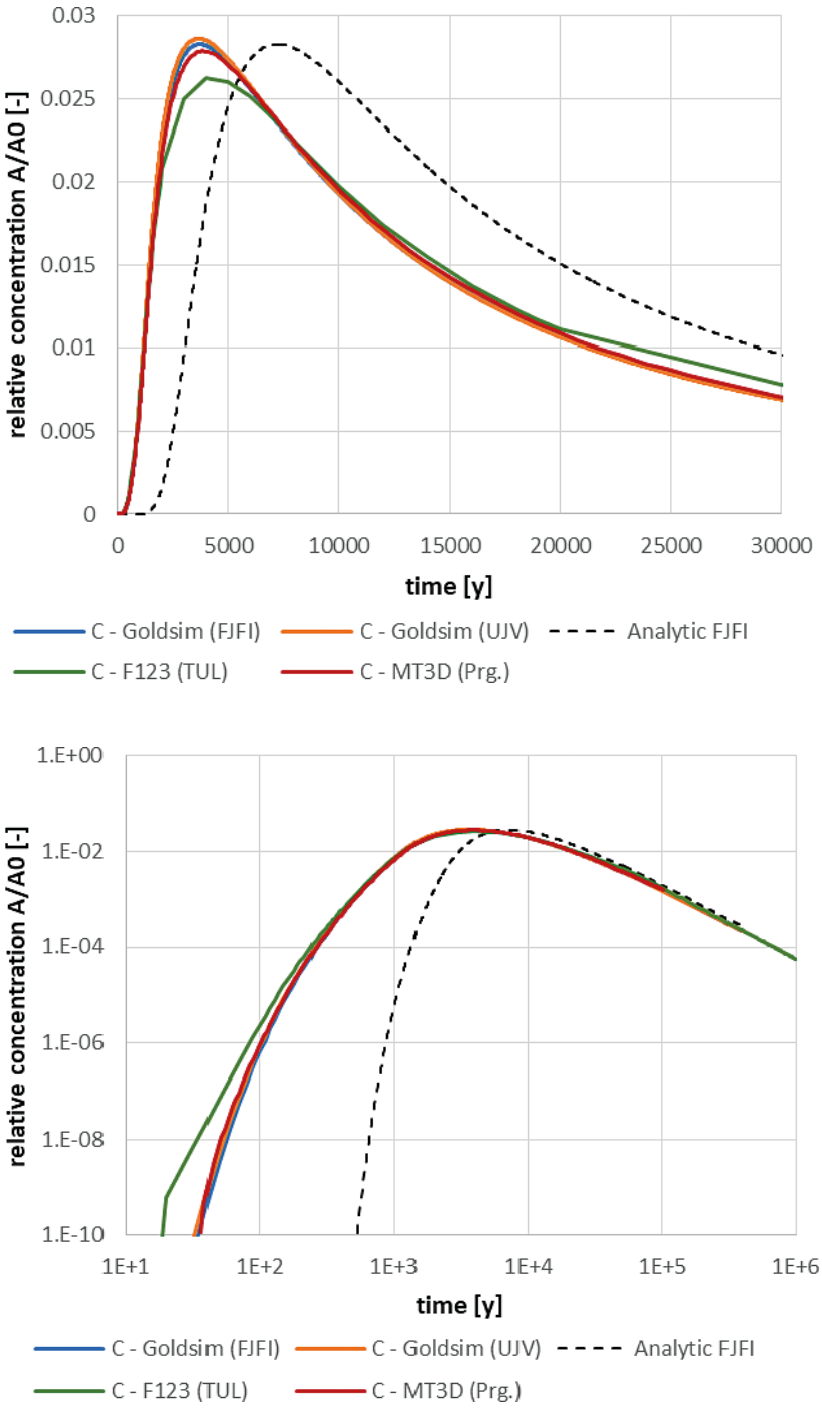

Figure A2-9. *Comparison of solution 9D-1-a breakthrough curves plotted against two types of axis scale for tracer C (four models).*

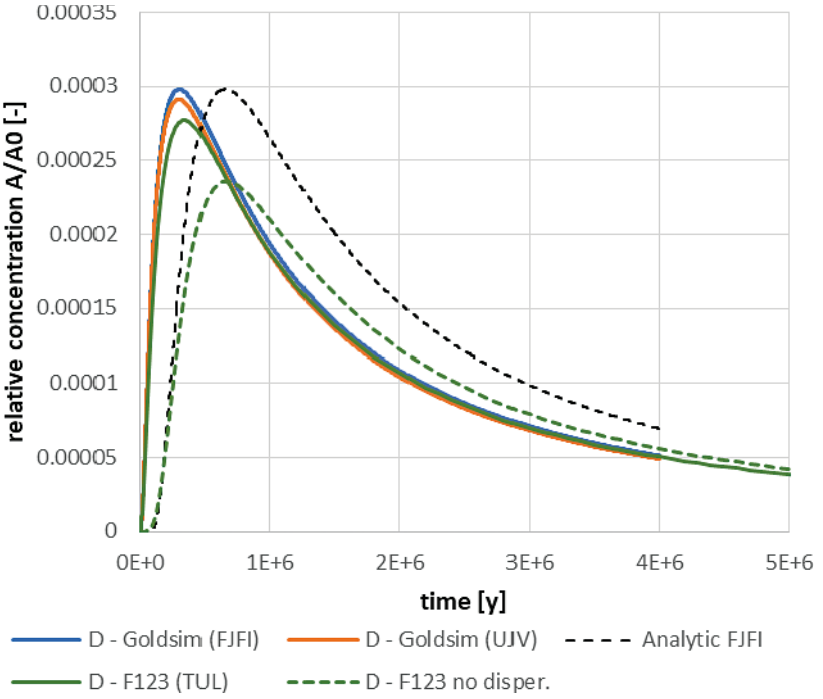

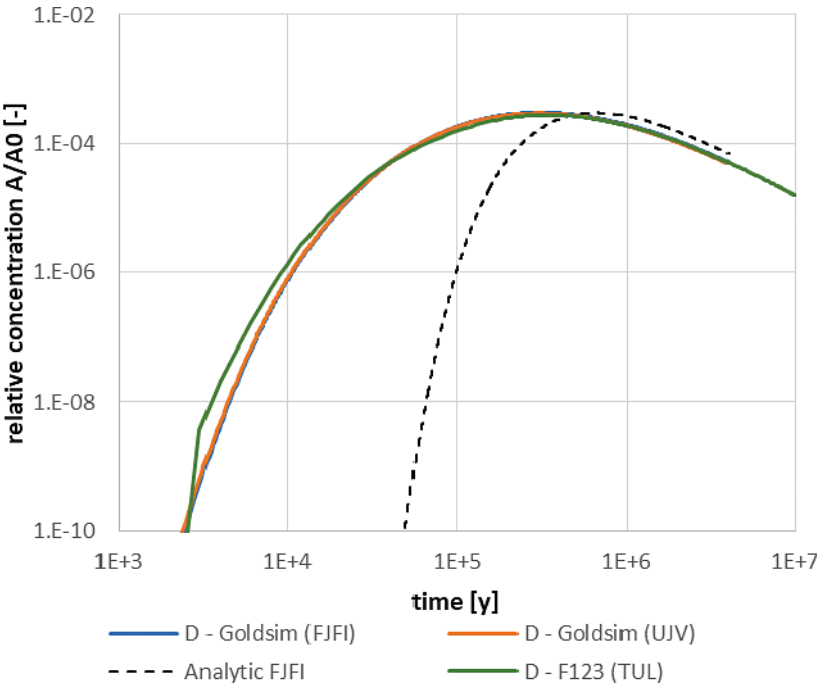

Figure A2-10. *Comparison of solution 9D-1-a breakthrough curves plotted against two types of axis scale for tracer D (three models and variants without dispersion corresponding to the analytical solution).*

For variants with a continuous input, the steady state is asymptotic; the outputs are drawn in one form with a linear axis for all of the tracers in Figure A2-11. Again, in contrast with the analytical solution, you can see the effect of dispersion at the position of the leading part of the curve for all numerical models. Slight differences in the asymptotic activity values are seen; they are more pronounced in tracer A, where each of the four models gives a different value. In this case, the dominant effect of time discretisation, probably related to the simultaneous calculation of transport and decay, was confirmed, where the discretisation becomes more apparent for rapid decay (Section A2.8).

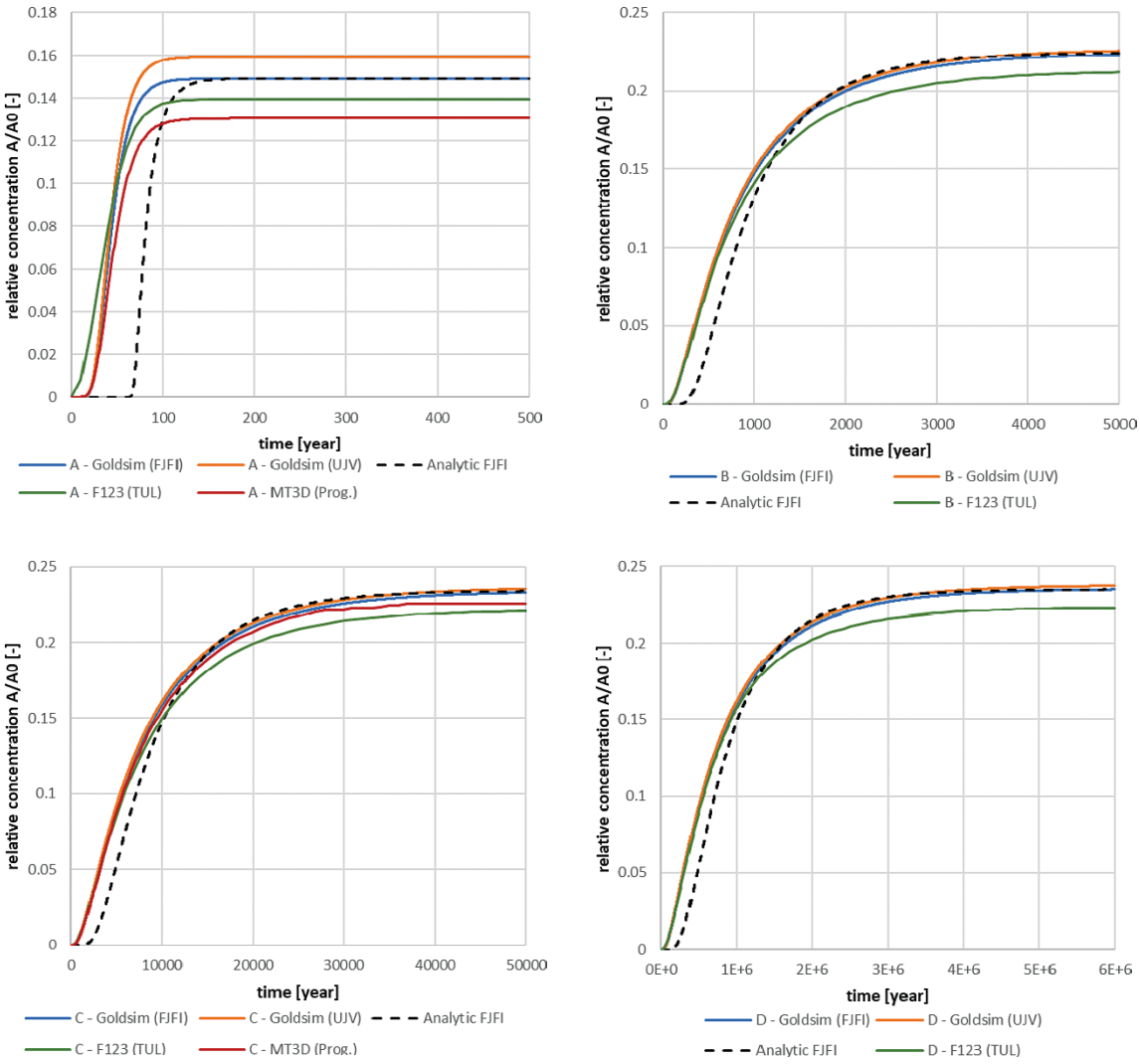

Figure A2-11. *Comparison of solution 9D-1-b breakthrough curves for all of the tracers (A – 4 models, B – 3 models, C – 4 models, D – 3 models).*

In Figure A2-12, only the profiles of the GoldSim (CTU) and Flow123d (TUL) models are compared. The starting points of the fracture profiles differ slightly (in accordance with slight differences in breakthrough curves) and the trends are qualitatively identical. The results of Flow123d show the smoothness of the curves, which is probably due to the course discretisation and the effect of interpolation of points with values differing by one order of magnitude.

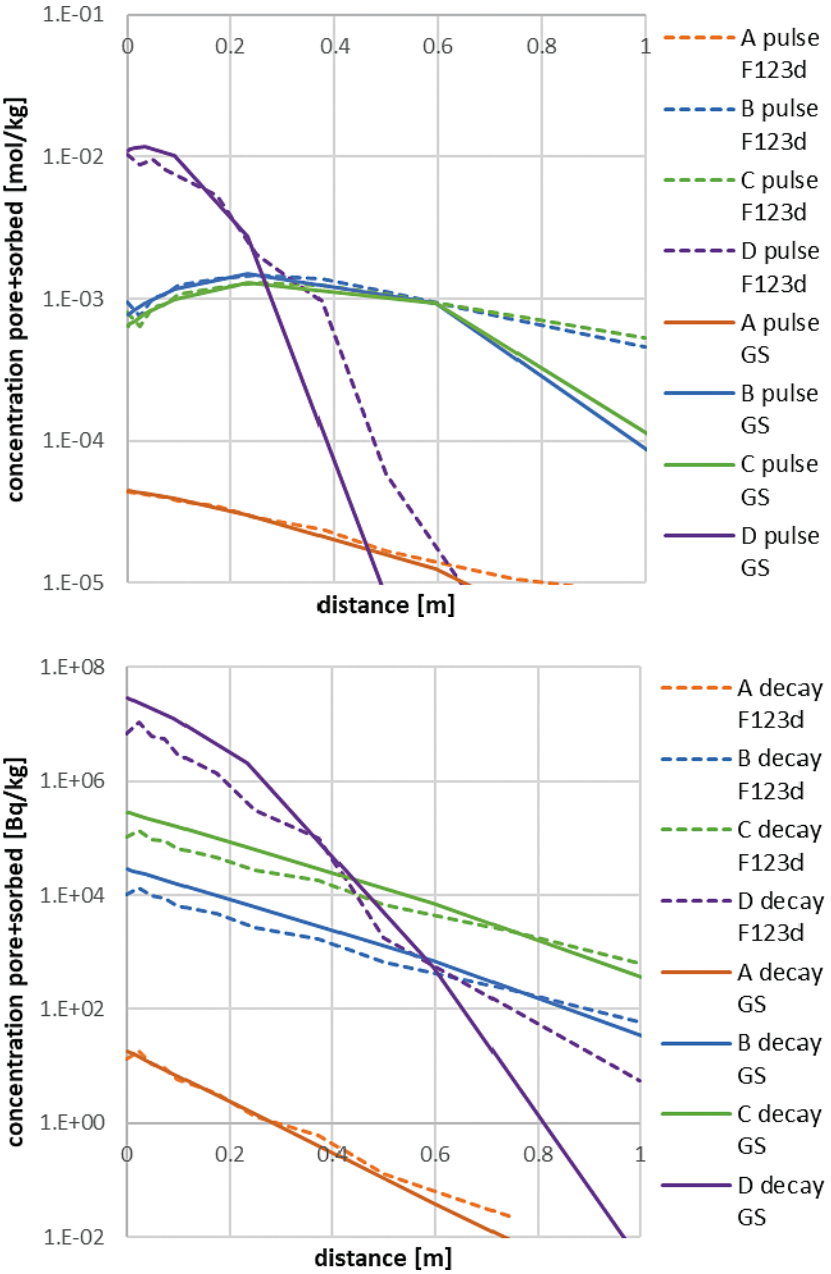

Figure A2-12. *Comparison of solution 9D-1 cross-sectional profiles of two models (Flow123d and GoldSim – GS) for all of the tracers. The first plot shows pulse inflow without decay (variant a) and the second shows continuous inflow with decay (variant b).*

A2.7.2 Task 9D-2

Figure A2-13 shows the processing of the two GoldSim models (CTU and ÚJV) in logarithmic axes over a longer period of time. Figure A2-14 shows a comparison of the three models GoldSim, Flow123d and MT3D, in linear axes. In the first case exact agreement is seen, except for a slight deviation in the leading edge of the Th curve (these values are one order of magnitude less than the maximum), as well as the differences in orders of magnitude between the activity values of the individual radionuclides, which cannot be captured on the linear axis. The results of Po and Pb are identical, due to equilibrium at a short half-life and the same transport parameters.

In the second case, Figure A2-14 shows the agreement of the models for U-238, U-234 and Ra, while for the remaining radionuclides, Th, Pb and Po, the result of Flow123d is significantly different (in a similar order to the other radionuclides, while the rest agree with values of approximately two orders of magnitude lower). This is more precisely quantified in Table A2-8, which shows values of activities at 1 Ma (i.e., selected points on the curves). It may be seen that in the three radionuclide cases with higher sorption, the deviation of the GoldSim and MT3D models is evident in the order of agreement. This hypothesis is again directed to the effect of discretisation in connection with high sorption.

As a control, U-238 was compared with the considered decay against the D-tracer without decay (Figure A2-15). A second auxiliary comparison is given in the following section.

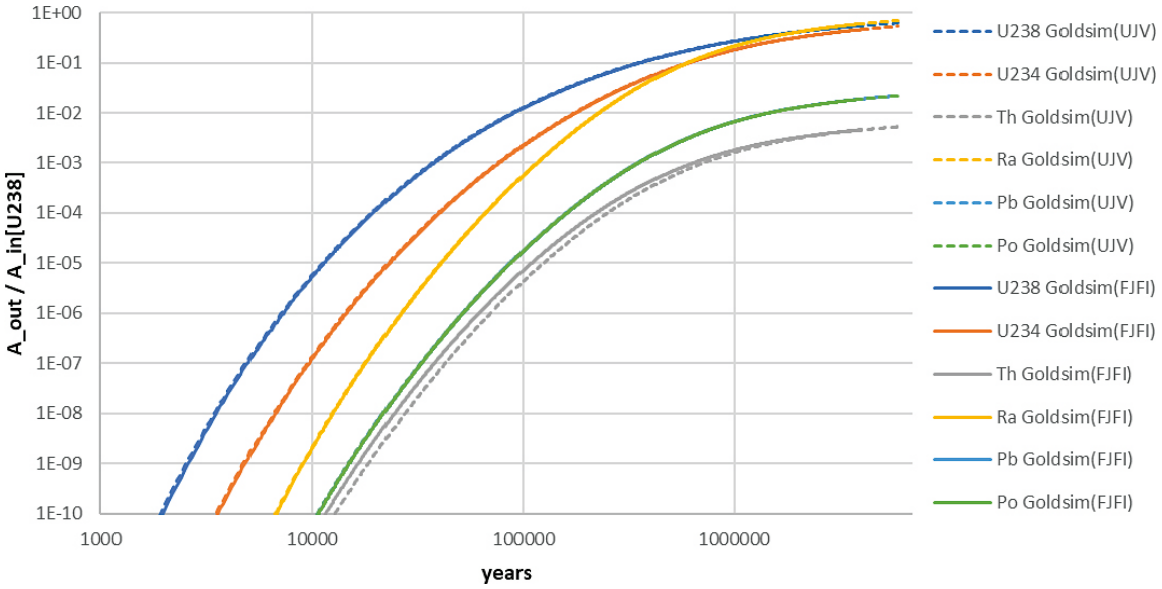

Figure A2-13. *Comparison of solution 9D-2 showing breakthrough curves for six radionuclides in the decay series (Pb is graphically indistinguishable from Po) and two independently processed GoldSim calculations.*

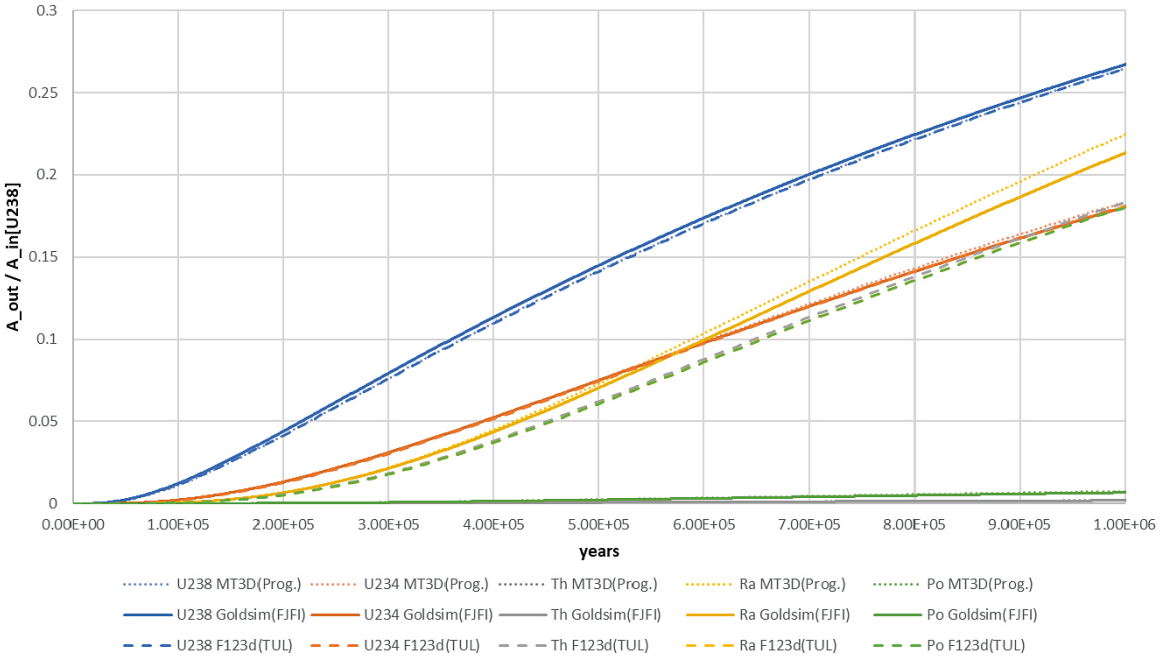

Figure A2-14. *Comparison of solution 9D-2 showing breakthrough curves for five radionuclides in the decay series (Pb is not plotted as it is graphically indistinguishable from Po) and calculations by three different software programs.*

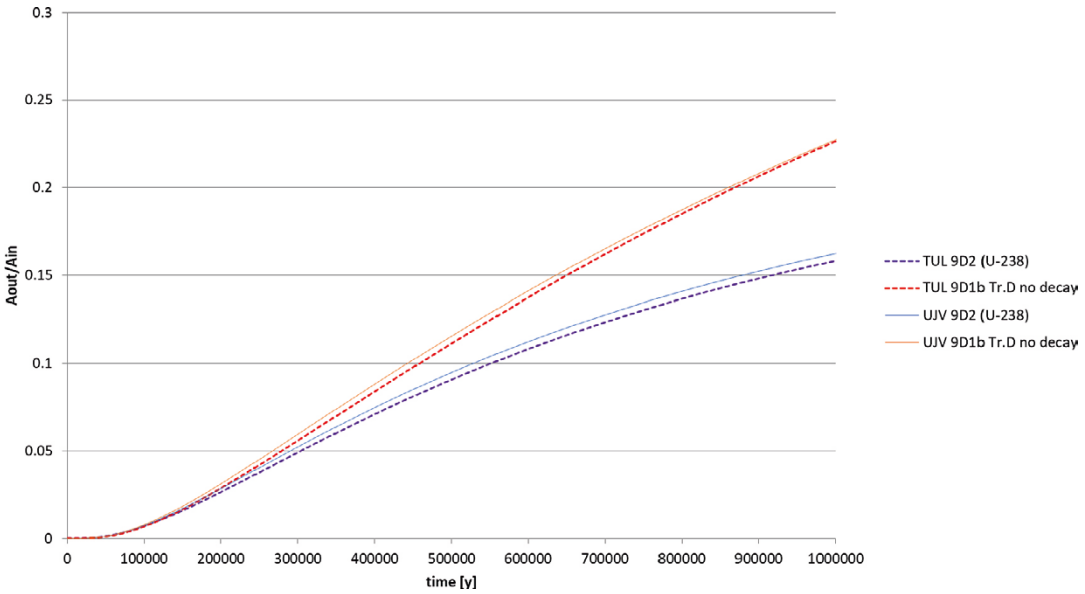

Figure A2-15. *A control comparison of the breakthrough curves of 9D-1 (tracer D) and 9D-2 (U-238) between Flow123d(TUL) and GoldSim (ÚJV).*

Table A2-8. Comparison of values on the breakthrough curve at 1 Ma (activity normalised by the input activity of U-238).

	U-238	U-234	Th-230	Ra-226	Pb-210	Po-210
GoldSim (CTU)	0.267	0.180	0.00179	0.213	0.00665	0.00662
GoldSim (ÚJV)	0.270	0.182	0.00161	0.213	0.00665	0.00662
MT3D-USGS	0.265	0.183	0.00185	0.224	0.00777	0.00748
Flow123d	0.265	0.181	0.183	0.180	0.180	0.180

A2.7.3 Auxiliary task with uniform sorption

Due to the large differences between the breakthrough curves of the more sorbing radionuclides in 9D-2 and the observed problematic behaviour during large sorption in previous tasks, an auxiliary task was defined. This task differed in so far as it set a uniform sorption coefficient $K_d = 8.0 \times 10^{-2}$ m^3/kg for all of the radionuclides in the decay series. This corresponds to the parameters of uranium. Other "dummy" radionuclides are labelled "-alt". A comparison of the breakthrough curves is shown in Figure A2-16, which shows a good agreement between GoldSim and Flow123d, thereby confirming the aforementioned cause of the difference in the results of the original task description for 9D-2. Table A2-9 compares the specific values of activity on the breakthrough curve.

The profiles of activity in the transverse direction in the rock matrix are shown in Figure A2-17. The agreement of parts of the curves near the fracture is good. The area where the course of the curves separates corresponds to the change in discretisation in the Flow123d model, which again confirms the combination of discretisation and large sorption as the main cause of the differences.

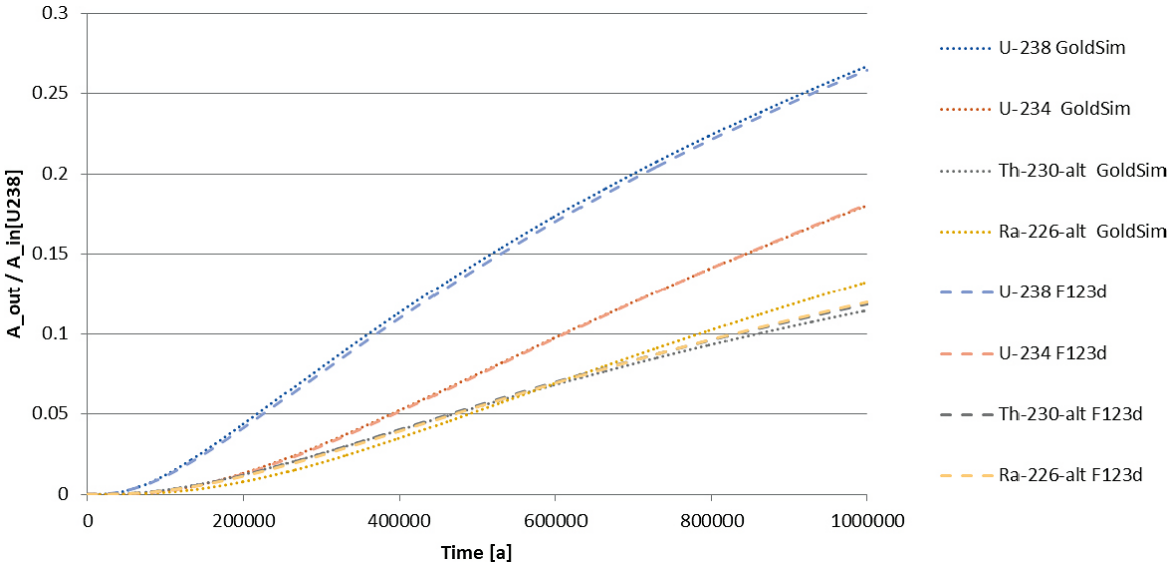

Figure A2-16. *Breakthrough curves of the auxiliary model (profiles Po and Pb are identical to Ra in both models).*

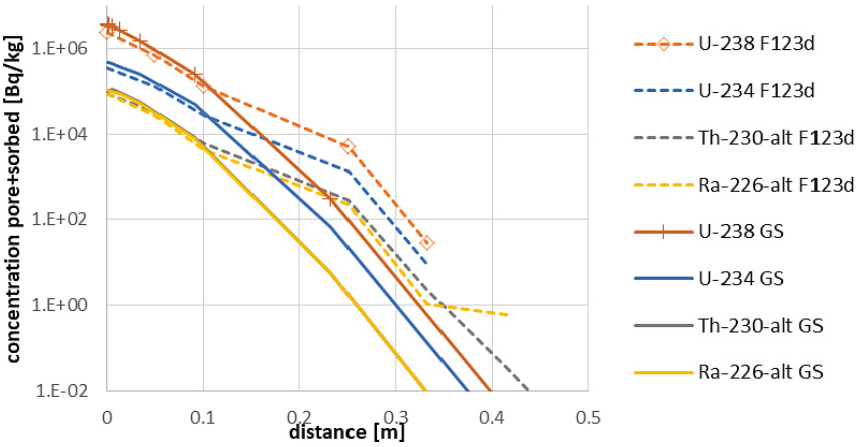

Figure A2-17. *Transverse profiles in the auxiliary model (Po and Pb profiles are identical to Ra in both models).*

Table A2-9. Comparison of values on the breakthrough curve at 1 Ma (activity normalised by the input activity of U-238) for a modified task with uniform sorption.

	U-238	U-234	Th-230	Ra-226	Pb-210	Po-210
GoldSim	0.267	0.18	0.114	0.132	0.132	0.132
Flow123d	0.265	0.181	0.119	0.12	0.12	0.12

A2.8 Verification of the influences in the calculation

A2.8.1 Sensitivity to spatial discretisation

The sensitivity of the course of the breakthrough curves to the spatial discretisation of the model (especially near the fracture/rock interface) was tested. For this purpose, five variants of the mesh were created, where the individual layers of the rock matrix had different thicknesses. The variants are described in Table A2-10, where the columns indicate at what depth (distance from the fracture) the individual layers end. The layer distances correspond to discretisation triangle sides in the direction perpendicular to the fracture. The "Refined fine" variant was created from the "Fine" mesh by dividing each of its triangular elements into four triangles. The analysis results are shown in Figure A2-18, Figure A2-19, Figure A2-20 and Figure A2-21 (scenario 9D-1a: no decay, BC in the form of a 1 000-year-long pulse). It is evident that for the conservative tracer, the results are not dependent on spatial discretization; with increasing sorption the dependence becomes more and more pronounced. Therefore, we reach the same conclusions as in the case of Task 9A, where we stated that a very fine mesh is needed for strongly sorbing tracers near the fracture/rock interface.

Table A2-10. Task9D – Flow123d – Mesh variants (the presented position of layer interface is also approximately the element size for the next layer, except the "Refined fine" – e.g. the zone between 0.5 m and 10 m is discretized by 0.5 m for "Fine").

Mesh marking	Layer 1 [m]	Layer 2 [m]	Layer 3 [m]	Layer 4 [m]	Layer 5 [m]
"Coarse"	0.2	0.4	1	2	10
"Medium"	0.1	0.2	0.5	1	10
"Fine"	0.05	0.1	0.25	0.5	10
"Refined fine"	0.05	0.1	0.25	0.5	10
"Thin"	0.005	0.01	0.03	0.1	1

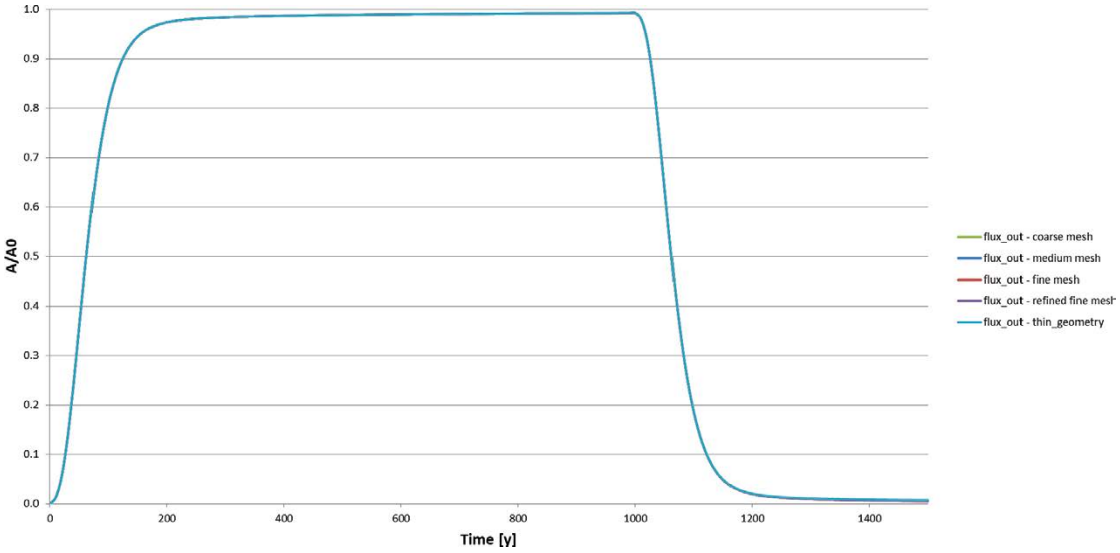

Figure A2-18. *Task9D – plot showing influence of spatial discretisation on tracer A.*

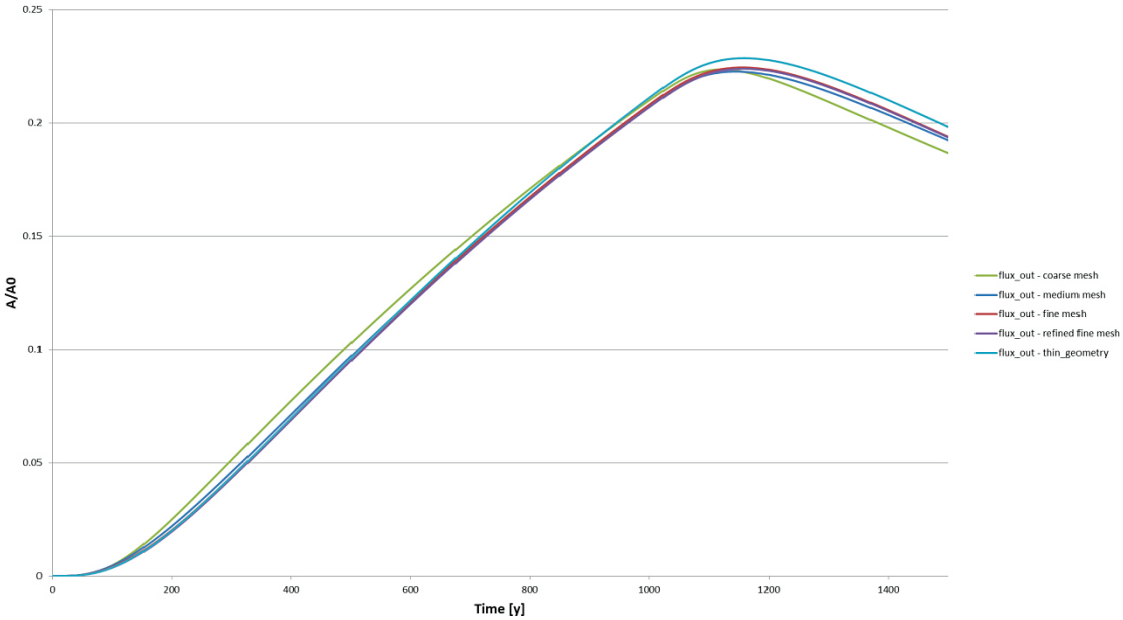

Figure A2-19. *Task9D – plot showing influence of spatial discretisation on tracer B.*

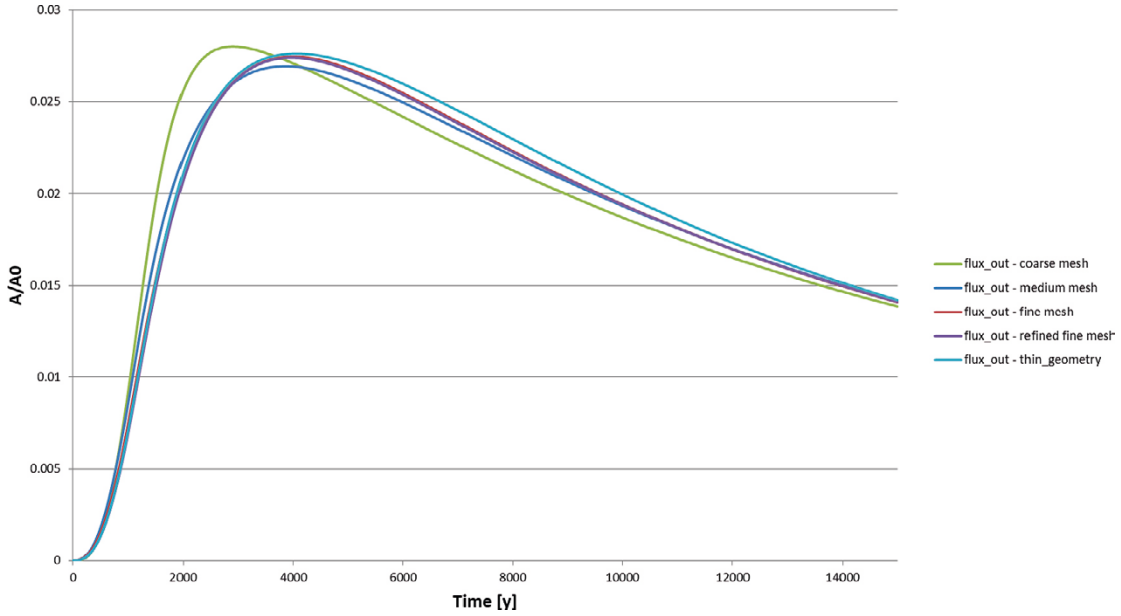

Figure A2-20. *Task9D – plot showing influence of spatial discretisation on tracer C.*

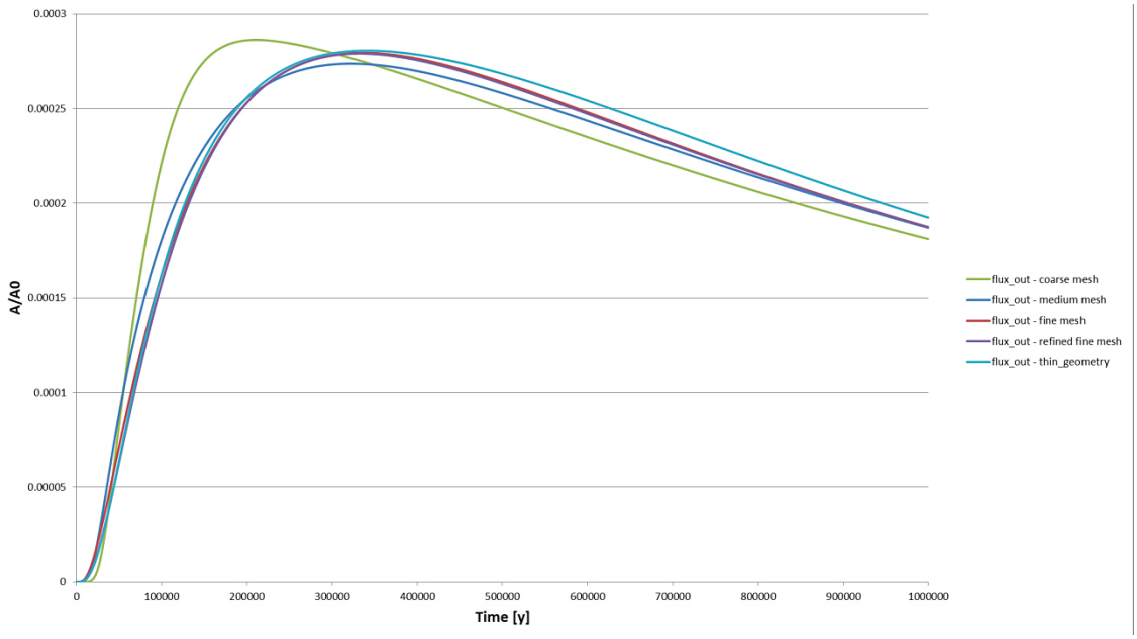

Figure A2-21. *Task9D – plot showing influence of spatial discretisation – tracer D.*

Sensitivity to the discretisation time was also tested. It was determined that it is advisable to choose a finer time step, especially in the beginning of the simulation. In the event that radioactive decay is considered, the length of the time step must also be chosen with regard to the half-life of the individual tracers.

A2.8.2 Influence of rock matrix thickness

The influence of the thickness of the rock matrix on the breakthrough curve (and the boundary conditions of zero mass flux over the outer boundary of the model) was tested. The simulation period was 10^6 years (10^7 for tracer D). Figure A2-22 shows the normalised breakthrough curves for each of the tracers, for rock matrix thicknesses 1 m and 10 m. The "waviness" of the breakthrough curve for a thicker rock matrix is caused by the variable time step of the calculation over time. The figure shows that the influence of matrix thickness (near the BC) is more significant for conservative and low-sorbing tracers. The influence is expressed on the course of the descending part of the breakthrough curve.

A2.8.3 Influence of hydrodynamic dispersion in the fracture

The influence of the presence of hydrodynamic dispersion in the fracture on the results of normalised breakthrough curves was tested. The tests were performed on a computational mesh with a rock matrix thickness of 10 m. The simulation period was 10^6 years (10^7 for tracer D). Figure A2-23 shows normalised breakthrough curves for each of the tracers with and without hydrodynamic dispersion. It may be seen from the figure that the hydrodynamic dispersion mainly has great influence on the shape of the leading edge of the breakthrough curve and the position of the maximum. The influence on the shape of the falling edge is negligible.

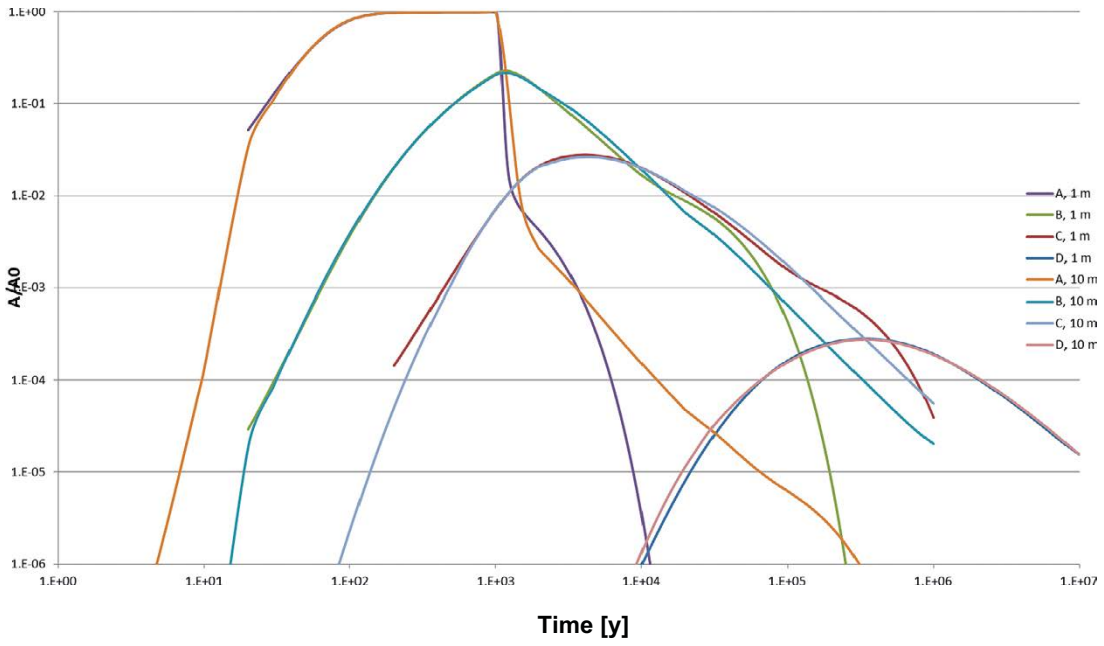

Figure A2-22. *Task9D-1a – influence of rock matrix thickness on normalised breakthrough curves of each of the tracers.*

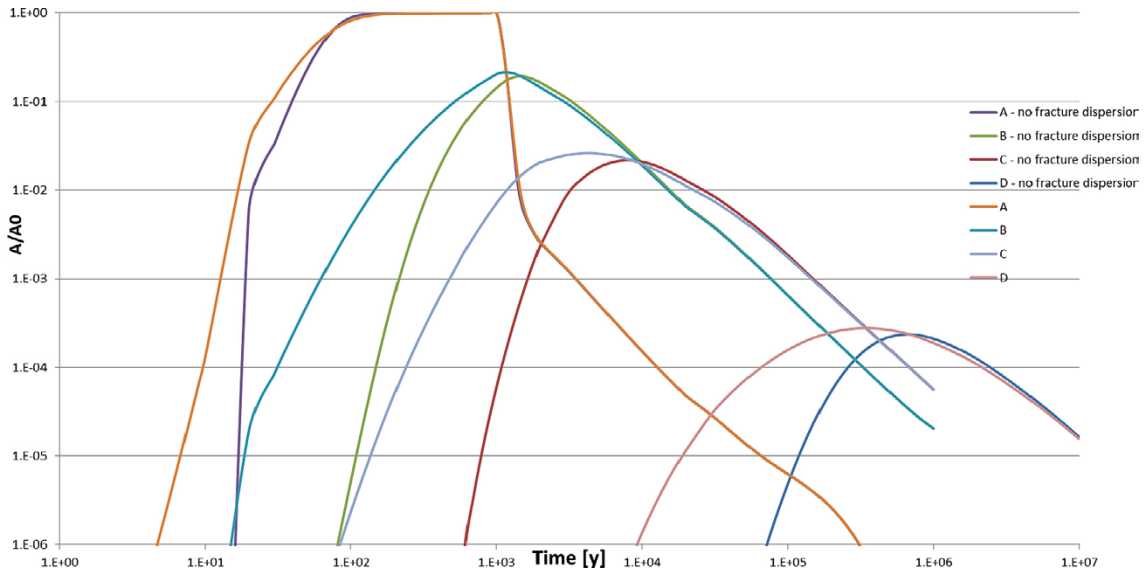

Figure A2-23. *Task9D-1a – influence of dispersion in the fracture on normalised breakthrough curves for each of the tracers.*

A2.9 Conclusion

The project solution has provided an understanding of the retention processes, especially the origin of uncertainties in calculations whose analogue may be part of the safety assessment.

The following text summarises specific conclusions evaluating the applicability and limitations of various conceptual models and simulation algorithms, as well as findings from experimental data that have a general overlap, i.e., they relate in particular to the crystalline rock environment without being bound to a specific location.

International collaboration contributed both to the availability of large amounts of data and the evaluation of methodologies and results in a wider team, including direct comparison of the results of a large number of models produced by different investigators. According to the requirements of the task description, verification of the use of simulation codes of Flow123d and GoldSim for radionuclide transport in relatively diverse configurations was achieved, and critical situations requiring attention and a control of the solution were determined.

A2.9.1 Evaluation of the modelling performed within Task 9

The comparison of the results of the predictive calculations resulted primarily in the verification of the simulation codes, but also in the correct way of entering input data in various forms transformed from the supplied data. The models of the Czech investigators (co-investigators of the sub-project to which the text of this appendix originally related) were verified among themselves in all Tasks 9A–9D. Models based on the same control equations and baseline assumptions gave consistent results, with any partial differences being clarified.

Although these were seemingly simple tasks (involving linear equations and regular geometry), it was determined that numerical algorithms may behave in a complicated and unpredictable way. Typical causes known in numerical mathematics may also be identified in the following tasks: large contrasts in the coefficients (manifested indirectly in the form of spatial mass balance in the case of sorption), spatial scale (extent of the breakthrough into the matrix) and temporal scale (decay rate versus transport rate).

The benefit of performing the calculation with the pipe elements in GoldSim (or the algorithm based on the analytical solution of transverse diffusion into the matrix) is the elimination of the influence of discretisation, thereby providing the most accurate solution, at the expense of constraints in the geometry of the area and spatial inhomogeneity of the fractures. The procedure cannot be used other

than for the transverse direction from the fracture and a homogeneous matrix must be assumed (e.g., without a Borehole Damage Zone (BDZ)). All of the models based on discretisation (GoldSim-CellNet, Flow123d and MT3D) suffer from inaccuracy as a result. In the case of a regular grid (GS-CellNet and MT3D), the refinement sufficient for the convergence of the solution was easier to achieve. On the other hand, the unstructured Flow123d mesh offers full flexibility in irregular geometry, as was the case with the TDE experiment with three boreholes, where various different conceptual simplifications had to be considered for GS-CellNet.

As with the original evaluation of the LTDE-SD experiments (Nilsson et al. 2010) and similar ones outside this project (Havlová et al. 2016), it was confirmed that the measured data characterising diffusion transport with sorption in many cases cannot be explained using standard equations and laboratory determined coefficients. Based on the previously designed concept of the BDZ (zone influenced by the drilling), the inverse models were implemented in the form of an inhomogeneous matrix with various different coefficients depending on the distance from the borehole wall. As a result, it was possible to obtain model results in agreement with the measurements in most cases, albeit with many limitations; often the determination is ambiguous and the obtained coefficient and position interfaces are not transferable to other cases.

The micro-DFN methodology is able to successfully explain the measured data in a more conceptual way, where the origin of the inhomogeneity data is given by the actual data of the rock microstructure. One limitation is that such data are bound to a specific sample and therefore cannot be used for prediction in general with the current methods of obtaining and processing the input data. Furthermore, there is no tried-and-tested method for upscaling to a corresponding safety assessment. Therefore, the implementation of the project provides space for further research in this direction.

A2.9.2 Benefits of the collaboration

Experimental data from underground laboratories in Sweden and Finland were provided in full to the whole international team of participants, which allowed for wide discussion of the interpretation of processes and the applicability of different types of models. For the further activities of SÚRAO, this brings a range of technical matters for the performance of experiments (which are not directly the subject of this modelling sub-project and result directly from materials available on the GWFTS portal) and suggestions for obtaining transport parameters of individual radionuclides for the needs of a safety assessment.

The discussions were largely aimed at distinguishing physical phenomena of interest and experimental artefacts. In particular, many discrepancies were found for the LTDE-SD experiment (Task 9B). At the same time, contradictory analogues were presented – cases where the rapid penetration of a small concentration of tracer to a greater depth can be observed as a real phenomenon, versus a contamination of samples. The other investigators in Task 9 worked with the models under either of these assumptions.

For the use of the models, it is essential to ensure the conditions of laboratory and in situ measurements, as this will allow the connection between transport parameters at different scales (e.g., the effect of disturbance at the borehole wall and the treated sample surface).

Furthermore, the necessity of simultaneous measurement of concentration (activity) in the reservoir of the injection borehole (or fractures) and in the rock itself (at least during the disassembly phase) was confirmed. Models based on one type of data lead to ambiguous interpretations and do not allow the determination of transport parameters that can be transferred to other conditions.

Appendix 3

Contribution from KTH – Task 9D report

Shuo Meng, Luis Moreno, Longcheng Liu
Department of Chemical Engineering, Royal Institute of Technology, KTH, Stockholm, Sweden

December 2020

A3.1 Introduction

We have performed the modelling exercises following the guidelines found in the Task Description (Appendix 5). The task description includes two tasks: Tasks 9D-1 and 9D-2. The present report will introduce our conceptual model for the two tasks and present the calculation results. The effects of assumptions considered in the conceptual model on simulation results will also be discussed.

A3.1.1 Background

We have worked with flow and transport in fractured crystalline rocks with porous matrices for a long time, and our interest is primarily aimed at applications to nuclear waste repositories. Over the years we have developed analytical and numerical computation tools suitable for such applications and have performed numerous field and laboratory experiments related to this problem.

A3.1.2 Objectives

Task 9D focuses on extrapolating results from in situ experimental conditions to something more closely resembling a typical Safety Assessment (SA) scenario. In the exercise of Task 9D, we work on an extruded geometry of the setup in REPRO experiments of Task 9A.

A3.1.3 Scope and limitations

The modelling in Task 9D (Task 9D-1 and -2) is based on the multi-channel model and the effect of velocity dispersion is mainly considered. In addition, the heterogeneity of rock matrix in the model is accounted for in terms of distribution coefficients, the variation of which is spatially dependent. Porosity and pore diffusivity in the model are assumed to be constant. Single nuclide radioactive decay is considered in Task 9D-1 and the radioactive decay chain is accounted for in Task 9D-2.

A3.1.4 Outline of the Report

The simulation results of Task 9D-1 and -2 are presented in Chapter A3.3. In addition to expected outcomes, the influences of assumptions on calculation results, including the number of sub-channels in one flow-path, Beta probability distribution, Fickian dispersion, and the number of flow-paths in 9D-1, as well as the assumption of heterogeneity of the rock matrix in 9D-2, are discussed.

A3.2 Methodology and model

The experimental section of Task 9D is schematically shown in Figure A3-1. It is a coupled system, composed of a flat fracture and rock matrix at both sides. The fracture has a length on the order of 1 000 m and a width of 8.87 cm. Its average aperture is 2.45 mm. The water flows into the fracture at a rate of 3.55×10^{-3}/yr, and a moderate of hydrodynamic dispersion (Pe = 10) is accounted for.

A3.2.1 Conceptual model and mathematical model

The model includes moderate hydrodynamic dispersion. Numerous field observations show that Pe is often found in the range between 1 and 100 (predominantly $1 \sim 10$) (Gelhar 1993, Gelhar et al. 1992). This actually defines the pulse spreading dominated by velocity dispersion and the contribution of Fickian dispersion is negligible. To account for the hydrodynamic dispersion in terms of velocity dispersion, a 1D multi-channel model (Liu et al. 2018) might be made use of.

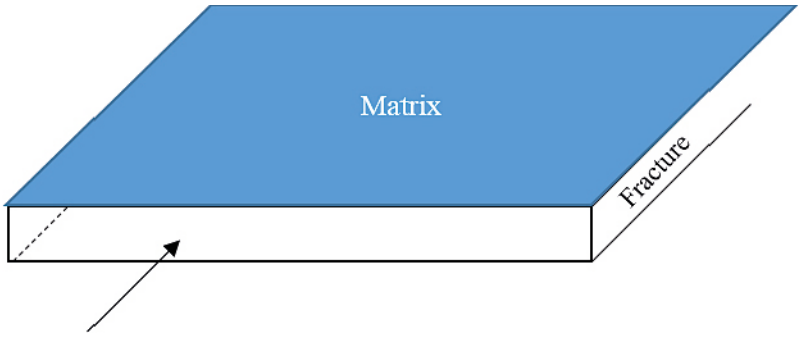

Figure A3-1. *Schematic overview of REPRO experimental setup.*

In a 1D multi-channel model, as schematically shown in Figure A3-2, the fracture might be seen as a system of N independent channels or flow-paths, the cross-section of which is rectangular and constant along one channel. The channels are identical in width but each has an individual aperture. In other words, the width of the channels is the same while the aperture might vary across channels, which can often be described by a probability distribution function. Likewise, the flow-rate might be distinct in different channels, as following a certain distribution. The solute will not mix between those channels; they are only mixed at the outlet. Thus, the solute concentration at the outlet of the fracture can be written as

$$c_{\mathrm{f}}\left(t\right)=\frac{\sum_{i=1}^{i=N} q_{\mathrm{i}} c_{\mathrm{f,i}}\left(t\right)}{\sum_{i=1}^{i=N} q_{\mathrm{i}}} \tag{A3-1}$$

where q_{i} is the flow-rate in i-th channel and $c_{\mathrm{f,i}}$ is the solute concentration at the outlet of i-th channel.

The assumption behind this equation is that any influence on $c_{\mathrm{f,i}}$ by q_{i} is already accounted for. However, it is almost impossible to know the number of channels present in the fracture. For facilitating the mathematical manipulations, we can rewrite Equation A3-1 in a continuous form. It is,

$$c_{\mathrm{f}}\left(t\right)=\frac{1}{q_{\mathrm{mean}}}\int_{0}^{\infty} c_{\mathrm{f}}\left(t;q\right)\kappa\left(q\right)q\mathrm{d}q \tag{A3-2}$$

with

$$q_{\mathrm{mean}}=\int_{0}^{\infty} q\kappa\left(q\right)\mathrm{d}q \tag{A3-3}$$

where q_{mean} is the mean flow-rate of the ensemble of channels.

$\kappa(q)$ represents the real flow-rate distribution among the channels. It is often estimated from the aperture field of natural fractures, as follows. We assume that the flow velocity u in each channel is related to the aperture of that channel, denoted as b, by the cubic law (Bird et al. 2002), which is written as

$$u=kb^{2} \tag{A3-4}$$

where k is a constant characterizing the water velocity.

Since the width w in each channel is known, the flow-rate is obviously related to aperture in terms of Equation A3-4. Provided that the aperture field follows a log-normal distribution (Hakami and Larsson 1996, Keller 1997), i.e. Lognormal (μ_{a}, σ_{a}^{2}), $\kappa(q)$ can be estimated readily. As a result, the Péclet number, quantifying the spreading of the tracer pulse caused by velocity dispersion, is derived and shown in Liu et al. (2018), which is

$$\mathrm{Pe}=\frac{2}{\exp\left(4\sigma_{\mathrm{a}}^{2}\right)-1} \tag{A3-5}$$

and the mean flow-rate in this case is written as,

$$q_{\text{mean}} = wkb_{\text{mean}}^3 \exp\left(3\sigma_{\text{a}}^2\right) \tag{A3-6}$$

where b_{mean} is the mean aperture of the ensemble of channels, given by

$$b_{\text{mean}} = b_{\text{o}} \exp\left(\frac{\sigma_{\text{a}}^2}{2}\right), \tag{A3-7}$$

where b_{o} is the median aperture, defined as: $b_{\text{o}} = \exp(\mu_{\text{a}})$.

Because Pe is known in the task description, σ_{a}^2 can be readily obtained from Equation A3-5. Likewise, we assume that the mean aperture b_{mean} is equal to the given aperture in the task description, which makes μ_{a} determined in Equation A3-7. In addition, we consider that the given fracture water flow-rate in the task description is the mean water flow-rate of the ensemble of channels and that the given width is the summation of the width of the ensemble of channels. Therefore, the velocity constant k can be derived from Equation A3-6 directly and all unknown parameters are determined from given conditions in the task description.

$c_{\text{f}}(t,q)$ denotes the solute concentration in the channel outlet having a volumetric flow-rate q, and can be derived semi-analytically (i.e., by numerical inversion of a solution in Laplace domain, as shown in Mahmoudzadeh et al. (2014)). It considers the transport and interaction mechanisms that may influence the solute transport. For instance, we note that the heterogeneity of rock matrix along the flow-path is accounted for in cases (c) and (d). Then it can be assumed that the flow-path is composed of numerous sub-channels. The rock matrix is homogenous in each sub-channel, while only the distribution coefficients are different between adjacent sub-channels. Consequently, the rock matrix becomes heterogeneous along the flow-path.

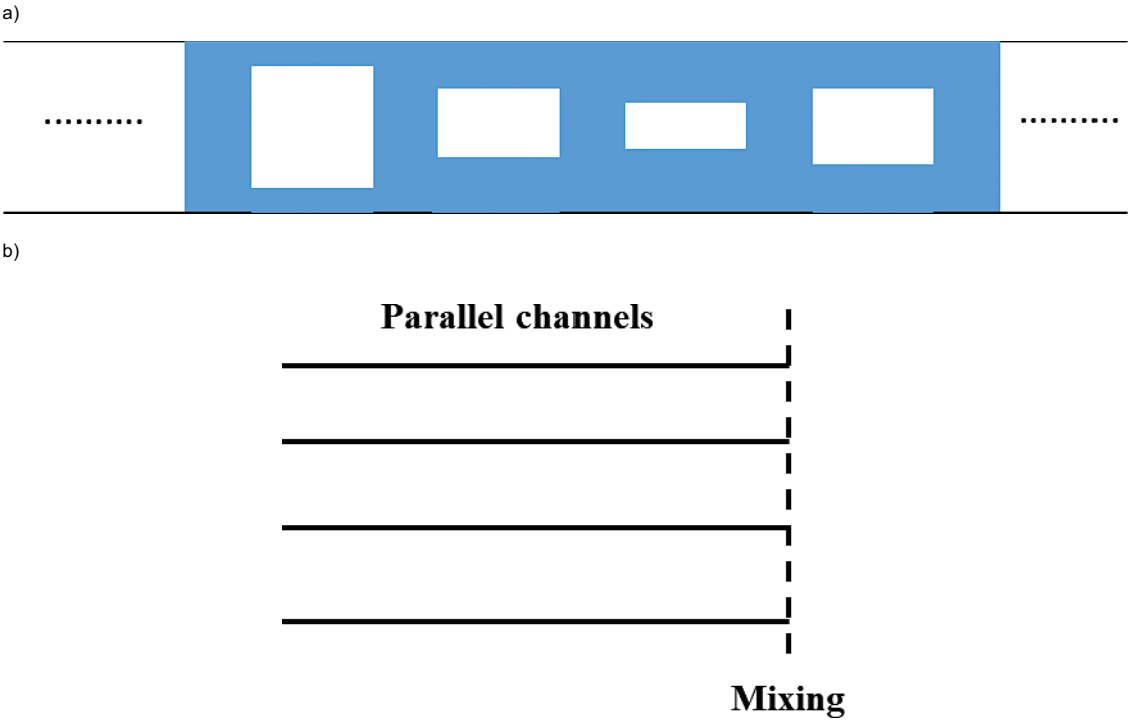

Figure A3-2. *Schematic view of the flow channels in a conductive fracture: a) the cross-sectional view of a fracture, where the blue shadow indicates rock matrix and white parts represents channels; b) the top view of a fracture, where each black line refers to a channel.*

K_d is considered to be linearly proportional to the local mica volume fraction, as suggested in the task description. This dependence indicates that the assumed heterogeneity can be implemented in terms of varied local mica volume fractions. The local mica content in this case is considered to be described by a beta probability distribution, i.e., Beta (α,β), which has a mean local mica content of 31.3 % and a minimum of 0 % , while the highest content is 100 %. The mean of a beta probability distribution, denoted as E_{beta} can be written as

$$E_{beta} = \frac{\alpha}{\alpha + \beta} \tag{A3-8}$$

Since E_{beta} is known, β can obviously be obtained, provided that α is given. However, many groups of α and β can be derived, because of limited conditions in the task description. To simplify the subsequent simulations and discussion, only two group of values are chosen, which are presented in next section.

A3.2.2 Input data

The dominant rock type in Task 9D is VGN (magmatic metamorphic gneiss, veined-gneiss), in which mica has a mean volume fraction of 31.3 %. The average bulk density of the rock is 2 741 kg/m^3 and the mean porosity is 0.65 %.

The tracers used in Task 9D are different in distinct subtasks. In the first subtask, Task 9D-1, there are four tracers: A (non-sorbing), B (weakly-sorbing), C (moderately-sorbing) and D (strongly-sorbing). Their distribution coefficient (K_d), effective diffusivity (D_e), half-life ($t_{½}$) and decay constant λ are detailed in Table A3-1.

Table A3-1. Solute-specific material property parameters for use in Task 9D-1.

Solute	K_d (m^3/kg)	D_e (m^2/s)	$t_{½}$ (yr)	λ (1/yr)
A (non-sorbing)	0	5×10^{-15}	20	3.47×10^{-2}
B (weakly-sorbing)	10^{-4}	1.83×10^{-13}	10^3	6.93×10^{-4}
C (moderately-sorbing)	10^{-3}	1.83×10^{-13}	10^4	6.93×10^{-5}
D (strongly-sorbing)	0.1	1.83×10^{-13}	10^6	6.93×10^{-7}

These four tracers were injected into the systems with two injection modes: rectangle mode for Case (a) and (c) and Heaviside mode (1 MBq/yr) for (b) and (d). In the rectangle mode (1 000 yr of injection time, 1 mol/yr), the rock matrix is assumed to be heterogeneous in Case (c) and homogeneous in Case (a). Likewise, heterogeneity is considered in Case (d) and homogeneity in Case (b). In addition, decay is accounted for in Cases (b) and (d) for comparison purposes. In Task 9D-2, the radionuclides belonging to the radium decay chain (4n+2), starting at U-238 are applied. All the information is summarized in Table A3-2.

Table A3-2. Detailed information of four cases in Task 9D-1 and two cases in Task 9D-2.

	Case	Injection mode	Concentration/Activity	Rock matrix	Decay
9D-1	a	Rectangle 1 000 yr	1 mol/yr	Homogeneous	No-decay
	b	Heaviside	1 MBq/yr	Homogeneous	Decay
	c	Rectangle 1 000 yr	1 mol/yr	Heterogeneous	No-decay
	d	Heaviside	1 MBq/yr	Heterogeneous	Decay
9D-2	a	Heaviside	1 MBq/yr	Homogeneous	Decay
	b	Heaviside	1 MBq/yr	Heterogeneous	Decay

We should note the implementation of the given injection conditions in the subsequent simulations. As introduced before, we assume that there are N independent channels in the fracture with individual flow-rate q_i, where N approaches to infinity. The total flow-rate of the ensemble of channels is $\sum_{i=1}^{i=N} q_i$. However, we know that the mean flow-rate of the ensemble of channels is q_{mean}. Therefore, the total

flow-rate can also be written as Nq_{mean} and the injected concentration c_0 to each channel in Task 9D-1 and Task 9D-2 as

$$c_0 = \frac{\text{Injected flux}}{Nq_{\text{mean}}} \tag{A3-9}$$

The solute specific material properties are specified in Table A3-3.

Table A3-3. Solute-specific material property parameters for use in Task 9D-2.

Solute	K_d (m³/kg)	D_e (m²/s)	$t_{½}$ (yr)	λ (1/yr)
U-238	8.0×10^{-2}	1.83×10^{-13}	4.47×10^{9}	1.55×10^{-10}
U-234	8.0×10^{-2}	1.83×10^{-13}	2.45×10^{5}	2.83×10^{-6}
Th-230	8.0	5×10^{-15}	7.54×10^{4}	9.19×10^{-6}
Ra-226	6.0×10^{-2}	1.83×10^{-13}	1.6×10^{3}	4.33×10^{-4}
Pb-210	2.0	1.83×10^{-13}	22.2	3.12×10^{-2}
Po-210	2.0	1.83×10^{-13}	0.379	1.83

In Task 9D-2, there was only one injection mode: a constant flux boundary condition for U-238 with zero flux specified for daughter nuclides, as shown in Table A3-2. In Case (a), the rock matrix is homogeneous, while a heterogeneous rock matrix is assumed in Case (b).

A3.2.3 Sensitivity cases

In Task 9D-1, some factors which may have influence on the simulation results are discussed, including: the number of sub-channels in one flow-path, Beta probability distribution, Fickian dispersion, and the number of flow-paths.

In Task 9D-2, we focus on the influence of the heterogeneity of the rock matrix on the simulation results.

A3.3 Results and discussion

A3.3.1 Task 9D-1

Basic case

As introduced in the previous section, the heterogeneity of the rock matrix along the flow-path is characterized in terms of several homogeneous sub-channels, between which the distribution coefficients are different. To simplify the problem for the first attempt or basic case, we consider that the overall heterogeneity property in each flow-path is the same, including the distribution coefficient value in the sub-channel and the sequence of distribution coefficients. Notably, for the basic case we always assume that there are an infinite number of channels or flow-paths in one fracture.

Based on this assumption, numerous simulations are performed for 9D-1, as indicated in Table A3-2. The additional input parameters are shown in Table A3-4.

Table A3-4. Additional input parameters for performed simulations.

Probability distribution parameter		Value
μ_a		−6.0365
σ_a		0.2135
Beta-1	α	3
	β	6.5847
Beta-2	α	0.5
	β	1.0974

The breakthrough curves obtained in Cases (a), (b), (c) and (d) are presented below. We emphasize that the parameters in Beta-1 are applied in the simulations.

Case (a) – Homogeneous, No-Decay

In Case (a), the rock matrix is considered to be homogeneous. Therefore only the impact of the distribution coefficient is studied. Decay is not considered in this case (See Figure A3-3).

The solute concentration at the outlet of the fracture is normalized by c_0. The x-coordinate is the elapsed time in years. For non-sorbing tracers, the breakthrough time is around 8 years and the breakthrough curve reaches a plateau state at around 100 years. The solute concentrations decrease gradually after 1 000 years, due to the stop of the injection. The breakthrough times of the sorbing tracers are significantly influenced by their sorbing properties. The larger the distribution coefficients are, the more the breakthrough times are retarded. The peak concentration is also related to the sorbing property; it is found that the peak concentration decreases with the increase of distribution coefficient.

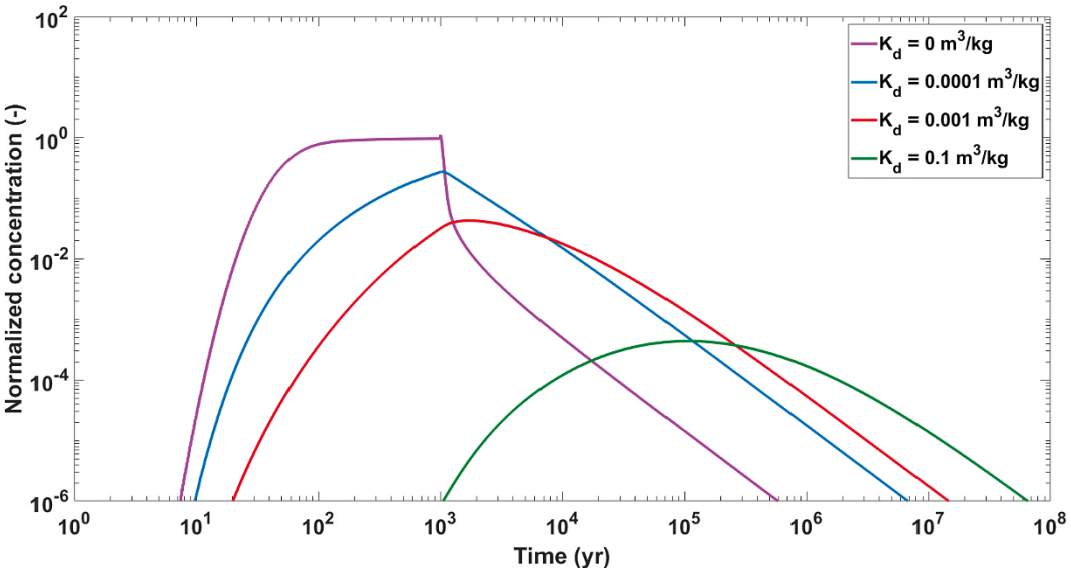

Figure A3-3. *Breakthrough curves for non-sorbing, weakly sorbing, moderately sorbing and strongly sorbing tracers with K_d = 0, 0.0001, 0.001, and 0.1 m^3/kg, respectively. The concentration is normalized by c_0, defined in Equation A3-9 for Case (a). Decay is not considered in this case.*

Case (c) – Heterogeneous, No-Decay

In this case, the rock matrix is considered to be heterogeneous so that the influence of heterogeneity on solute transport can be studied. The heterogeneity of the rock matrix is accounted for by assuming different distribution coefficients between sub-channels. Thus, we assume that there are 100 sub-channels in one flow path. K_d in each sub-channel is taken randomly from a beta probability distribution. The effect of heterogeneity on solute transport is not obvious for weakly sorbing tracers (see Figure A3-4a). By contrast, the breakthrough curves for each realization differ significantly from the reference breakthrough curve for strongly sorbing tracers (see Figure A3-4b). However, the late time performances of realizations for both weakly sorbing and strongly sorbing tracers are identical to the reference cases (homogeneous cases). It indicates that the impact of heterogeneity plays an important role at early time.

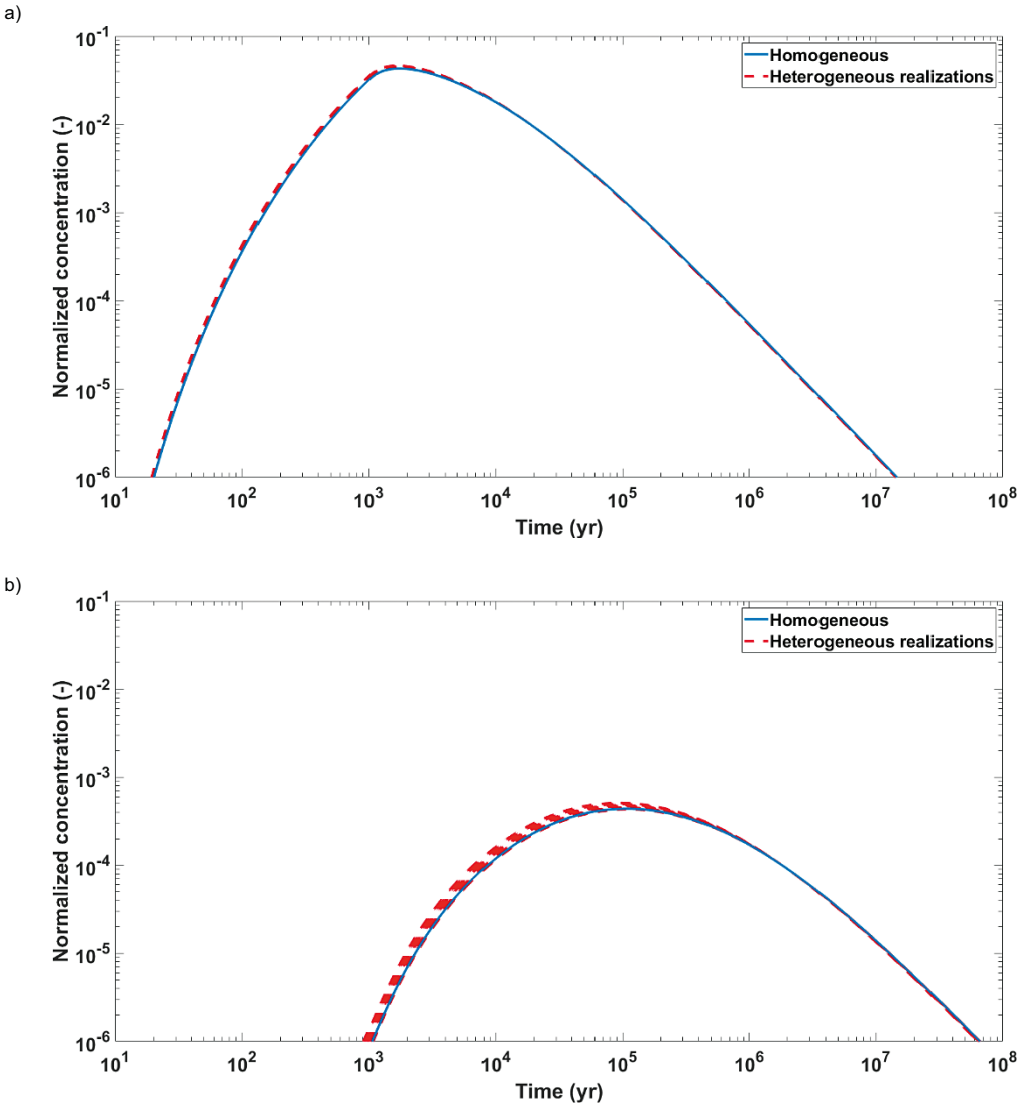

Figure A3-4. *Breakthrough curves for: a) weakly sorbing tracer (K_d = 0.0001 m^3/kg); and b) strongly sorbing tracer (K_d = 0.1 m^3/kg), assuming 100 sub-channels in each flow-path. "Homogeneous" indicates the homogeneous case in Figure A3-3; "heterogeneous realizations" refers to the different heterogeneous cases, in which K_d of each sub-channel is randomly distributed following a given distribution. The activity is normalized by c_0 in Equation A3-9 for Case (a). Decay is not considered.*

Case (b) – Homogeneous, Decay

In Case (b), the rock matrix is considered to be homogeneous and the effect of radioactive decay is accounted for. Based on the conceptualized model, the obtained breakthrough curves for four tracers are shown in Figure A3-5.

As in the analysis of Case (a), the influence of sorption makes an important contribution. The breakthrough time is strongly influenced by the distribution coefficient. For the non-sorbing tracer the arrival time is short (less than 10–20 years), while for the strongly sorbing tracer, the breakthrough time is long (more than 10 000 years in our case). The long breakthrough time indicates that the strongly sorbing tracer is more retarded than other tracers. By contrast, the behaviours of the breakthrough curves at long times are mainly affected by the half-lives of the radionuclides and their distribution coefficient. We note that the injection mode in this case is Heaviside. As a result, it can be expected that there is a plateau at late times with a value lower than the unity. The activity of the plateau (normalized) is determined by the relation between half-life and distribution coefficient. For a non-sorbing tracer with a long half-life the expected plateau is very close to one, since radioactive decay plays a very small role. On the other hand, for a strongly sorbing tracer with a short half-life, the plateau normalized activity will be very small. In order to predict the breakthrough curves of the different tracers, we need to consider the distribution coefficient and the half-life, in addition to the channel properties.

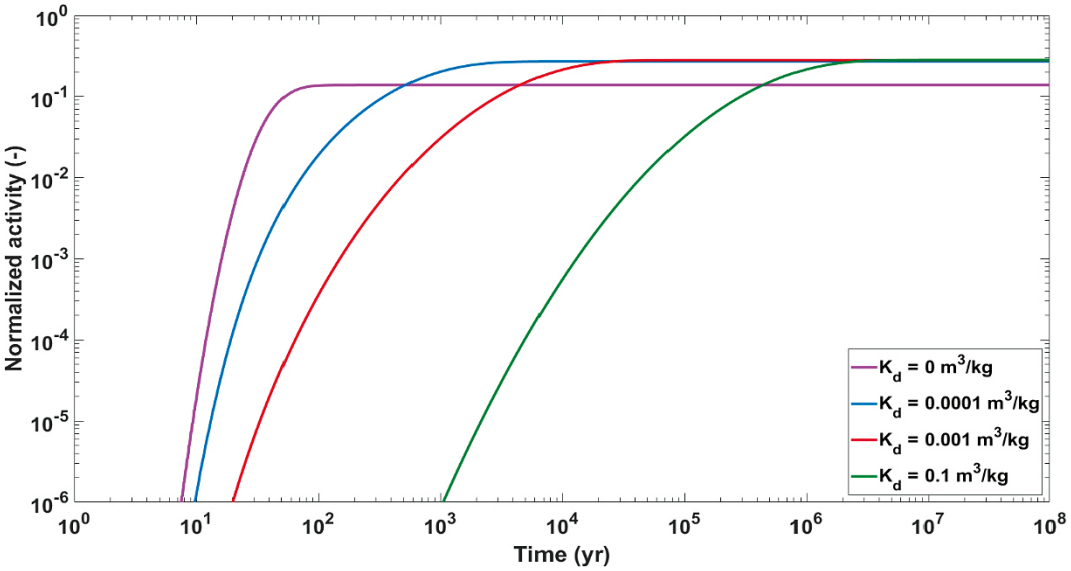

Figure A3-5. *Breakthrough curves for a homogeneous matrix for non-sorbing, weakly sorbing, moderately sorbing and strongly sorbing tracers with K_d = 0, 0.0001, 0.001, and 0.1 m^3/kg, respectively. Radioactive decay is accounted for with half-lives shown in Table A3-1. The activity is normalized by c_0 in Equation A3-9 for Case (b).*

Case (d) – Heterogeneous, Decay

In contrast to Case (b), the rock matrix is heterogeneous in Case (d). The breakthrough curves for the strongly sorbing tracer are shown in Figure A3-6 as an example.

As in the analysis of Case (c), the influence of heterogeneity is dependent on the number of sub-channels in one flow-path. The breakthrough curves of realizations in cases with fewer sub-channels show more differences at early times than those with a larger number of sub-channels. By contrast, the late time behaviours are not impacted.

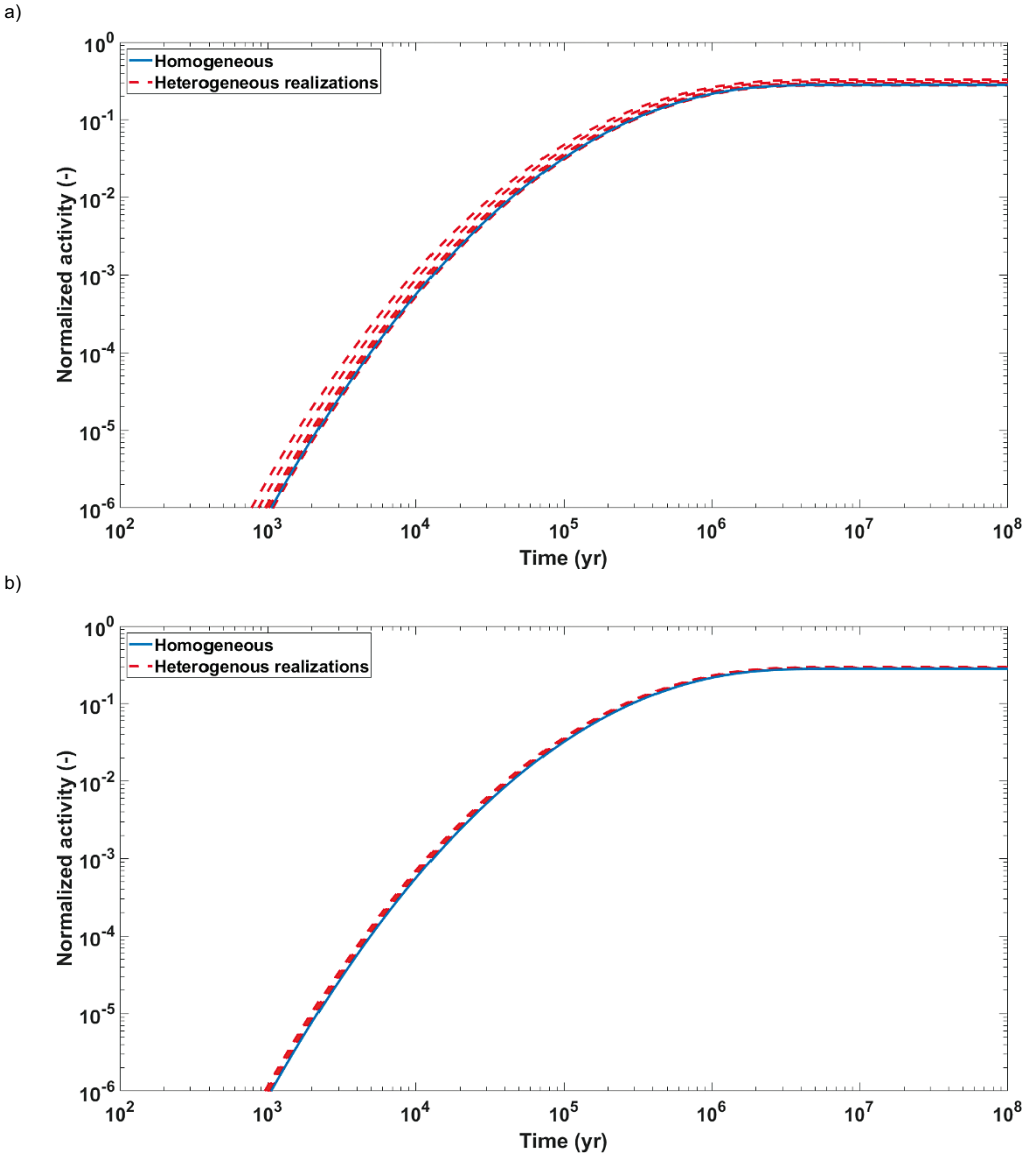

Figure A3-6. *Breakthrough curves based on the variation of number of sub-channels: a) 10; b) 1 000, for strongly sorbing tracer (K_d = 0.1 m^3/kg). The legend is defined in the Figure A3-4 caption. The activity is normalized by c_0 in Equation A3-9 for Case (b). Decay is considered.*

Further investigations

Influence of the number of sub-channels in one flow-path

To investigate the effect of the number of sub-channels on simulation results in Case (c), varying numbers of sub-channels were applied in simulations for a strongly sorbing tracer, as presented in Figure A3-7.

Figure A3-4b and Figure A3-7 show that a smaller number of sub-channels causes the realizations to deviate more strongly from the reference curve at both early and late times. This is consistent with our expectations, since the evaluated mean K_d in the lower number case is further away from the reference mean distribution coefficient. As a result, the varied sorption properties of the rock matrix affect the breakthrough curves. Consequently, the assumed number of sub-channels might influence the simulation results.

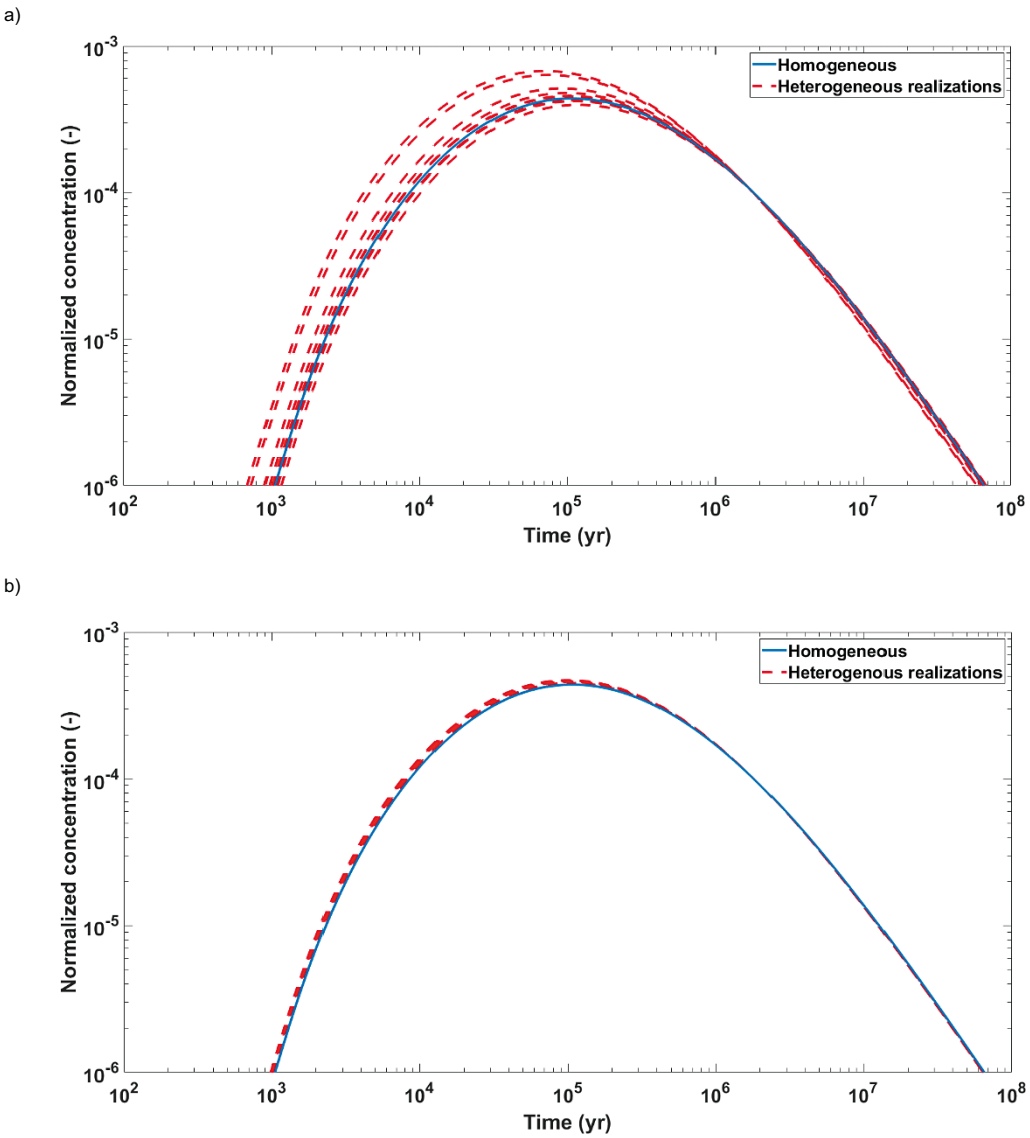

Figure A3-7. *Breakthrough curves based on the variation of number of sub-channels: a. 10; b. 1 000, for strongly sorbing tracer (K_d = 0.1 m^3/kg). The legend is defined in the Figure A3-4 caption. Decay is not considered.*

Influence of Beta probability distribution

All the presented simulation results are based on the parameters of Beta-1 set out in Table A3-4, since we assume that the local mica volume fraction is described by a certain probability distribution function. However, this assumption may not be valid in practice. To investigate the influence of this assumption on the simulation results, we applied another group of parameters for Beta probability distribution, indicated as Beta-2 in Table A3-4, in the simulations for strongly sorbing tracers like Case (c). To highlight the contribution, we consider cases in which there are only 10 sub-channels in one flow-path. The results can be shown in Figure A3-8.

The breakthrough curves using the Beta-2 probability distribution deviate significantly more from the homogeneous case at early times than the curves based on the Beta-1 probability distribution. The reason is that the calculated mean distribution coefficient from generated K_d is slightly different from the reference value. This is in line with the observation of tiny deviations between the breakthrough curve of simulated and homogeneous (i.e., reference) curves. For late time behaviour, the breakthrough curves of the realizations are almost identical to the homogeneous curve. The findings from Figure A3-8 indicate that the probability distribution of local mica content may influence the simulation results. However, the extent of the effect is limited, especially at late times.

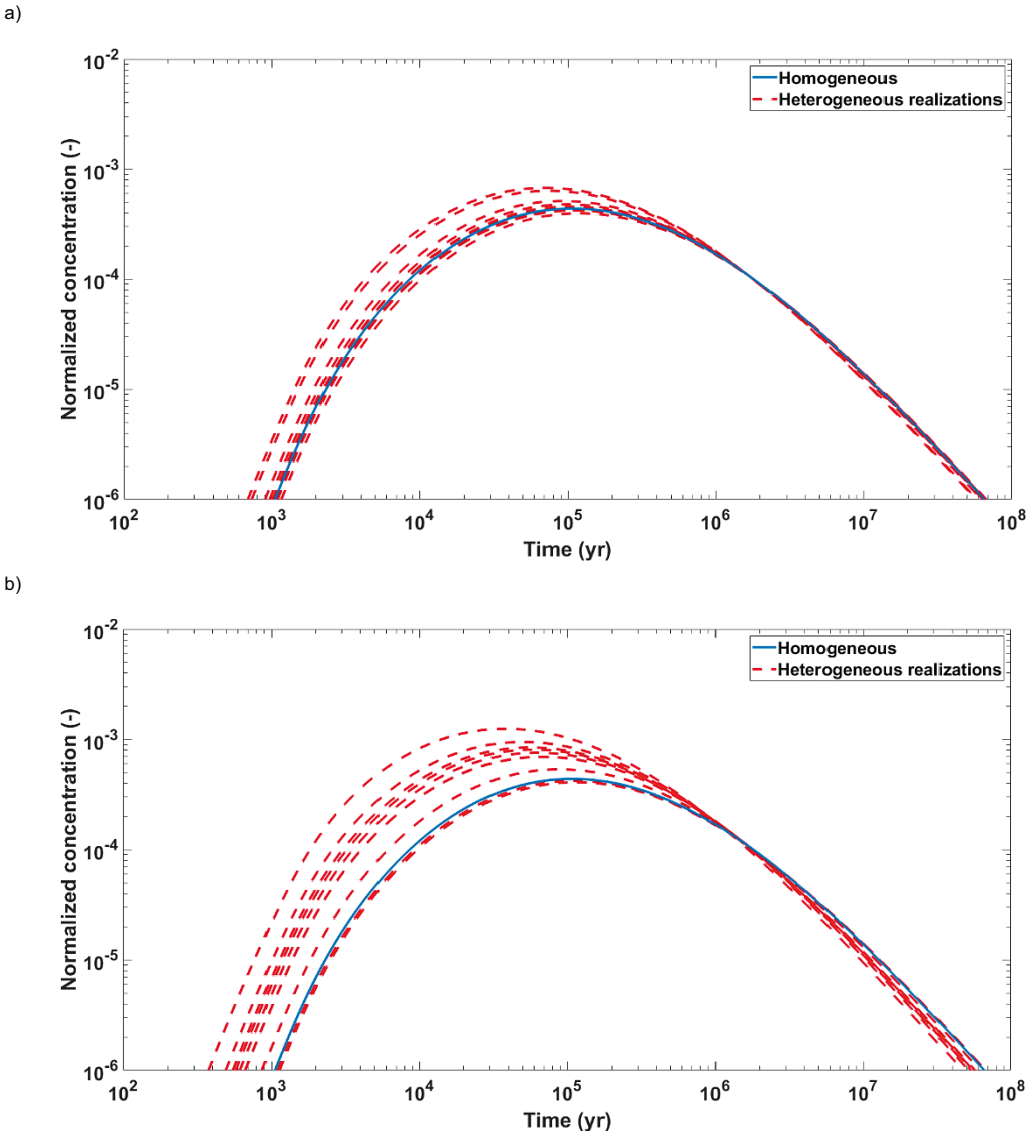

Figure A3-8. *Breakthrough curves for different parameters in the Beta probability distribution: a. Beta-1; b. Beta-2 as described in Table A3-4, for strongly sorbing tracer (K_d = 0.1 m^3/kg). The legend is defined in the Figure A3-4 caption. Decay is not considered.*

Influence of Fickian dispersion

As assumed in the conceptual model, the effect of Fickian dispersion is overshadowed by the contribution of velocity dispersion. To verify whether this assumption is reasonable, we revisited the non-sorbing tracer case in the Case (a) of Task 9D-1. It was found that Fickian dispersion only plays a more significant role than velocity dispersion in cases where channel length is very short, i.e., ≤ 1 m, or where matrix diffusion is not accounted for. Once the channel is larger than a few metres, the effect of Fickian dispersion is negligible, compared with velocity dispersion. If matrix diffusion is considered, the spreading of the breakthrough curve is dominated by matrix diffusion and the contributions of both velocity dispersion and Fickian dispersion are negligible, even though the tracer is non-sorbing. Therefore, we can expect that the effects of velocity dispersion and Fickian dispersion will be unimportant in the cases of sorbing tracers. Based on those results, the assumption used in Task 9D, i.e., neglecting the influence of Fickian dispersion, is reasonable.

Influence of number of flow-paths

In the multi-channel model, we conceptualize that there are an infinite number of flow-paths in a fracture, while in reality the number of channels in a fracture is limited. To investigate the effect of the number of flow-paths on simulation results, an additional simulation was performed, based on the assumption that there are only 10 channels in one fracture. The results are shown in Figure A3-9. The conditions were the same as those used in Case (b) of Task 9D-1, except that the number of flow-paths in the fracture were applied in the new simulation. A strongly sorbing tracer (tracer D) was adopted. 10 apertures in each realization were generated from a lognormal distribution.

We found that the late-time behaviour of the breakthrough curves is identical, since radioactive decay of the tracer dominates. However, we also found that the tailing of the breakthrough curve for the infinite number case in Figure A3-9 is different from that in Figure A3-5. This is caused by the small change of boundary conditions. In the present simulation, radioactive decay also applies to the injection condition, i.e., $c_{in}(t) = c_0 \exp(-\lambda t)$. However, in Case (b), radioactive decay starts after injection, i.e., $c_{in}(t) = c_0$. This explains why the tailing parts of the two simulations are different.

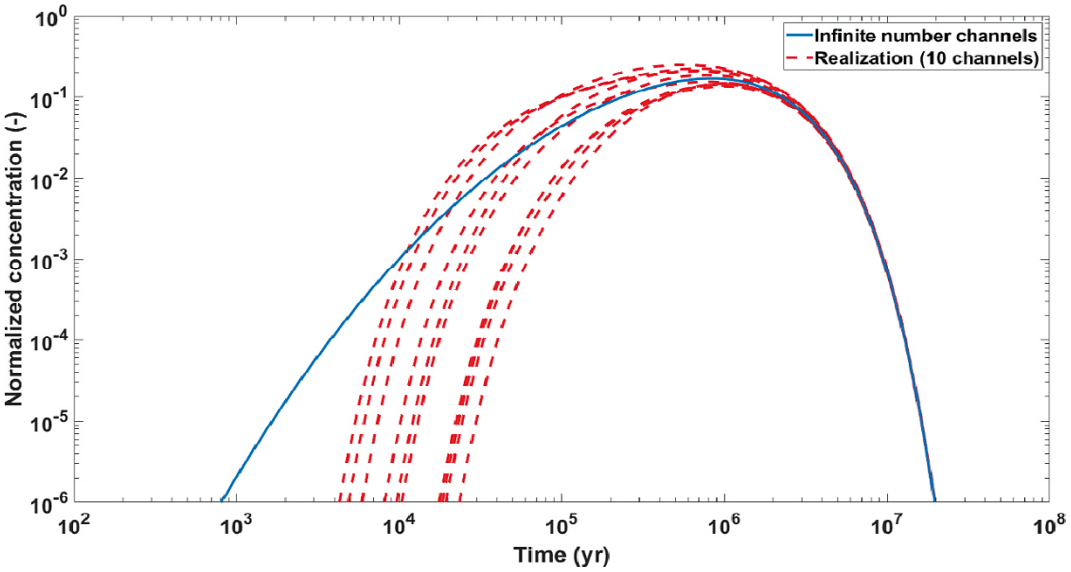

Figure A3-9. *Breakthrough curves for varying numbers of flow-paths in a fracture for strongly sorbing tracer (K_d = 0.1 m^3/kg). Decay is considered.*

Even though the tailings of breakthrough curves in Figure A3-9 are identical, the early-time performances of the breakthrough curves are different. The first-arrival time is much shorter for the infinite number of channels case than for the limited number case. This is caused by the variation of the mean flow-rate of the ensemble of channels. For an infinite number of channels, the mean flow-rate of the ensemble of channels can be estimated from the aperture distribution in a straightforward way. In other words, the mean flow-rate in this case can be denoted as statistical mean flow-rate. For the limited number case, the evaluated mean flow-rate may be different and thus deviate from the statistical mean flow-rate, even though all the apertures in the limited number channel case were generated from the same probability distribution. Therefore, the first-arrival times in different breakthrough curves are different. The same interpretation can be applied to the variation of peak concentration.

A3.3.2 Task 9D-2

Basic case

The only difference in Task 9D-2 relative to Task 9D-1 is the inclusion of the radionuclide decay chain. The basic geometrical and physical conditions from Task 9D-1 should be used as a starting point in Task 9D-2. Therefore, the same conceptual model in Task 9D-1 will be applied in the basic case of Task 9D-2.

Case (a): Homogeneous, Decay Chain

In Case (a), the rock matrix is assumed to be homogenous. The solute activity, including precursor U-238, and daughter nuclides, are shown in Figure A3-10.

In Figure A3-10, we can observe that all radionuclides perfom similarly. U-238 always has the highest activity, which is consistent with expectations. Even though equilibrium activity is determined by both sorption and radioactive decay, radioactive decay plays an insignificant role in the case of U-238, since its half-life is very long compared to the scheduled time period in simulation. Noticeably, the activity of the decay product is lower than that of its mother nuclide for the majority of tracers. However, this observation is not applicable to Th-230 and Ra-226. The activity of Ra-226 is higher than Th-230 but Ra-226 is the decay product of Th-230. This anomalous sequence is caused by the fact that the distribution coefficient of Ra-226 is much lower than the value of Th-230. The out-diffusion of decay product of Th-230 in the matrix makes a significant contribution, considering a constant flux boundary condition of 1 MBq/yr for U-238 and zero flux specified for daughter nuclides.

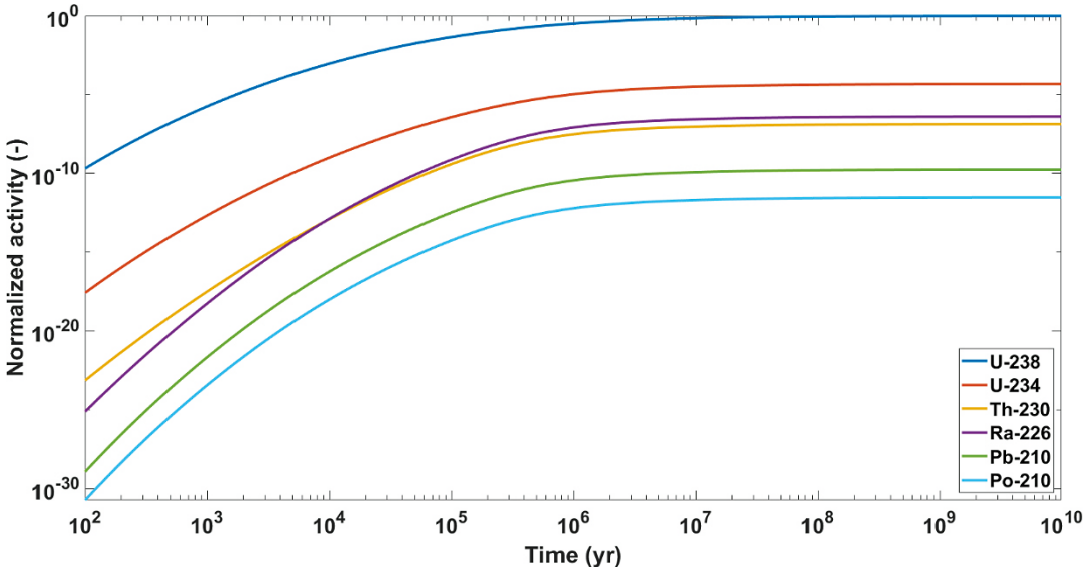

Figure A3-10. *Breakthrough curves for U-238 decay chain. Diffusion and sorption properties, as well as half-life, are shown in Table A3-3.*

Case (b): Heterogeneous, Decay Chain

Heterogeneity in the rock matrix is accounted for in Case (b), unlike in Case (a). As detailed in Task 9D-1, heterogeneous rock matrix in this system is also conceptualized in terms of small sub-channels, between which the distribution coefficient might be different. Since the breakthrough curves of U-238 and its daughter nuclides are similar, we will only present the simulation results of U-238, Th-230 and Ra-226, in this report.

As found in Figure A3-11, the consideration of heterogeneity in the rock matrix causes the breakthrough curves to deviate from the homogeneous case at early-times. By contrast, the late-time behaviours are almost identical, since the radioactive decay of nuclides also play a significant role. In addition, it is observed that the daughter nuclide is less influenced than its parent nuclide by heterogeneity. Therefore, the deviations between realizations and the homogeneous curve can apparently be found in the U-238 case.

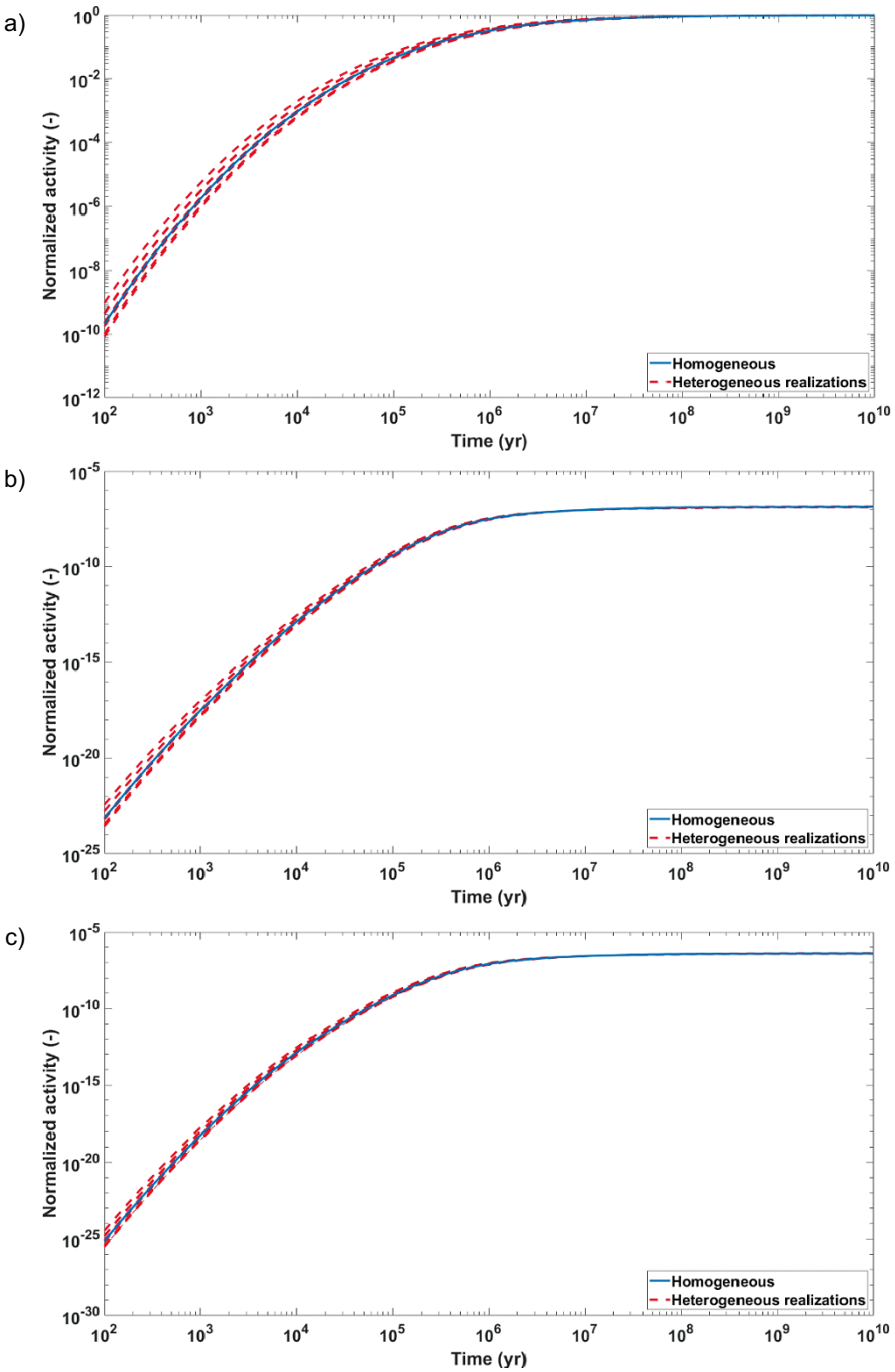

Figure A3-11. *Breakthrough curves of a) U-238; b) Th-230; c) Ra-226, assuming that there are 10 sub-channels in each flow-path.*

Further investigations

Influence of assumption in basic case

In the conceptual model, we assume that the heterogeneity of the rock matrix is described by sub-channels, between which the distribution coefficients might be different. The distribution of K_d in one flow-path is generated randomly, following a Beta distribution. In the basic case, we applied the same distribution to each flow-path. To investigate the influence of this assumption, we performed an additional simulation, in which the distribution of K_d in each flow-path is generated randomly and the distribution in different flow-paths might be distinct.

The additional simulation results of U-238 are shown in Figure A3-12. The deviations between realizations and homogeneous case are much smaller, when compared with the basic case in Figure A3-11a. This indicates that the assumption that each flow-path has an individual distribution of K_d causes the realizations to be closer to the homogenous curve. For daughter nuclides, we can expect differences to be much less significant.

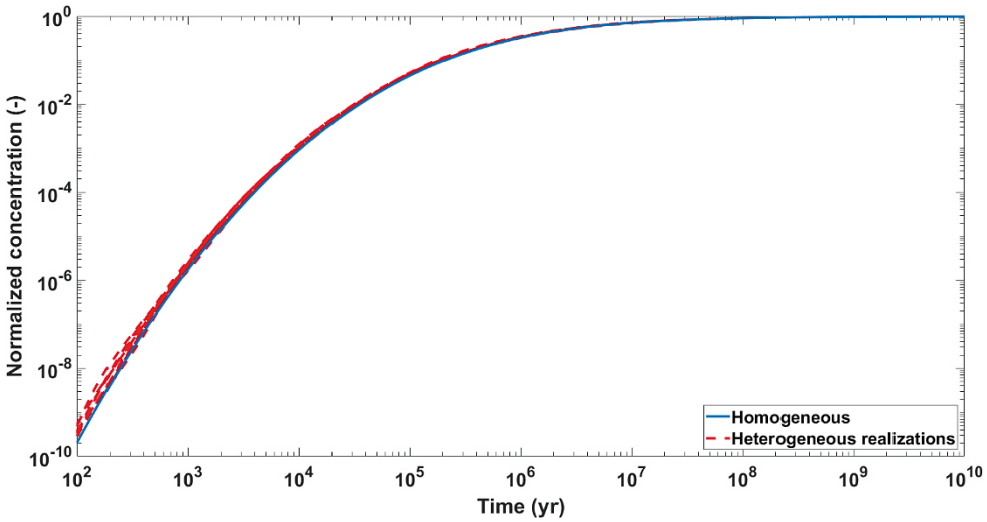

Figure A3-12. *Breakthrough curves of U-238, assuming that each flow-path has its own individual distribution of K_d.*

A3.4 Conclusions and recommendations

A3.4.1 Task 9D-1

In order to investigate the influence of rock matrix heterogeneity on solute transport, numerous simulations were performed, making use of the multi-channel model in Cases (a)–(d) for Task 9D-1. The heterogeneity in the model is considered as the spatial variation of the distribution coefficient in the matrix, while other properties of the rock matrix are assumed to be homogeneous. To implement this consideration, we assume that there are numerous sub-channels in one flow-path. In each sub-channel, the rock matrix is homogeneous while the properties might be different between adjacent sub-channels. To simplify the problem, the distribution of K_d can be described by a Beta distribution. As a result, the influence of heterogeneity can be considered in the model in a simple way.

The simulation results indicate that sorption can influence the performance of breakthrough curves. The breakthrough time, as well as the peak concentration time, will be significantly retarded for a strongly sorbing tracer. In addition, the value of peak concentration for a tracer is also partially dependent on the sorption property. The peak concentration for a strongly sorbing tracer is obviously much lower than the ones of moderately, weakly and non-sorbing tracers, provided that the half-lives of these tracers are identical. When the half-lives of the tracers are different, the above finding may not hold, since radioactive decay also makes a significant contribution to the determination of the peak value, as shown in Figure A3-5.

Heterogeneity may play an important role, especially at early times. However, this is dependent on the distribution coefficient. For a weakly sorbing tracer, the deviation between the breakthrough curves of realizations and the reference curve cannot be observed. Furthermore, it is noted that those differences are also dependent on the number of sub-channels in one flow-path; reducing the number of sub-channels causes the breakthrough curves of realizations to deviate from the reference curve, and vice versa.

The assumed probability distribution function describing the variation of distribution coefficient in the flow-path may also have an influence. However, the deviations between realizations and the reference case can only be observed at early times for cases with a strongly sorbing tracer and a low number of sub-channels.

Furthermore, it is noted that the effect of Fickian dispersion is neglected in the conceptual model in the basic case. To investigate the influence of Fickian dispersion on simulation results, a multitude of new simulations were performed, in which both Fickian dispersion and velocity dispersion were considered. It is found that Fickian dispersion plays a slightly more important role when fracture length is very short ($\leq$ 1 m) and matrix diffusion is not accounted for. As a result, it is not necessary to consider the effect of Fickian dispersion in Task 9D.

In the preliminary attempt we also assume that there are an infinite number of flow-paths in one fracture. This assumption is clearly inconsistent with the field observations. To investigate the influence of this assumption, we performed numerous simulations in which we conceptualized that there were 10 channels in each fracture. The early-time behaviours of these breakthrough curves differs from the case in which an infinite number of fractures is assumed. In particular, the first-arrival time is different, since the evaluated mean flow-rate might differ from the statistical one. By contrast, all breakthrough curves have identical late-time performances, due to the dominance of radioactive decay.

A3.4.2 Task 9D-2

The model used in Task 9D-1 was also applied in Task 9D-2. The only difference between these two tasks is that the radioactive decay chain of U-238 was considered in the new task. Simulation results for Task 9D-2-(a) in Figure A3-10 show that the breakthrough curves of six nuclides, including mother nuclide U-238 and its daughter nuclides, are similar. Their equilibrium activity is determined by both sorption and radioactive decay. Moreover, the equilibrium activity of one nuclide is generally higher than its daughter nuclide. However, this finding is not applicable to Th-230 and its decay product Ra-226, since the distribution coefficient of Th-230 is much higher than the value of Ra-226.

When the heterogeneous rock matrix was applied in Case (b), we found that the early-time performances of breakthrough curves in each realization were different from the curves obtained in the homogeneous case, as shown in Figure A3-11. By contrast, the late-time behaviours of both the homogeneous and realization cases are identical.

In addition, the heterogeneity in the rock matrix is characterized in terms of sub-channels in one flow-path. In order to carry out a preliminary attempt, we assumed that all flow-paths have the same distribution coefficients in the performed simulations. An additional simulation was performed in order to investigate the effects of this assumption on the simulation results, in which each flow-path has its own individual distribution. The simulation results, as presented in Figure A3-12, indicate that the influence on the solute transport, imposed by the heterogeneity of rock matrix, is reduced.

A3.4.3 Future work

The efforts made in Task 9D-1 and 9D-2 were relatively preliminary. In future work, heterogeneity may not only be considered in terms of sorption but also diffusion. Furthermore, the rock matrix may be heterogeneous along and perpendicular to the flow-path. These considerations can be implemented into the model in the next step.

Appendix 4

Contribution from CFE – Transport modelling of reactive tracers (Task 9D)

Rock Matrix Characterized by X-ray micro computed tomography data

Urban Svensson, CFE AB

August 2020

A4.1 Introduction

A4.1.1 Background

From the Task Description (TD) for Task 9D we quote the following sentence: "the Task 9D work may be considered to be a set of Synthetic Safety Assessment case studies" (Appendix 5). We may also infer from the TD that investigation of microstructural heterogeneity is relevant to Task 9D. Here we will focus on this latter aspect, as this will allow us to base the work on the developments from Task 9C (Svensson et al. 2019a, b).

The situation considered is shown in Figure A4-1. It is a classical channel-matrix case, where a tracer is injected at the upstream end of the channel and the breakthrough curve (BTC) at the downstream end is analysed. As indicated in the figure, we will use a particle-based method for transport and these particles may be sorbed on the channel wall and in the matrix. The matrix characterization will be based on data from X-ray micro computed tomography (X-µCT). As shown in Figure A4-2, the mineral distribution from a rock sample can be used to identity reactive minerals. The use of X-µCT data is a novel feature of the study.

A4.1.2 Objectives

The main objective of the study is to analyse the BTC for the channel-matrix system, based on a model that utilizes X-µCT data to characterize the matrix. Various processes affecting the BTC are evaluated by way of a sensitivity study.

A4.1.3 Scope and limitations

As mentioned above, the safety assessment aspect will not be considered here, which is a clear limitation. The scope is a theoretical model study without consideration of experimental data.

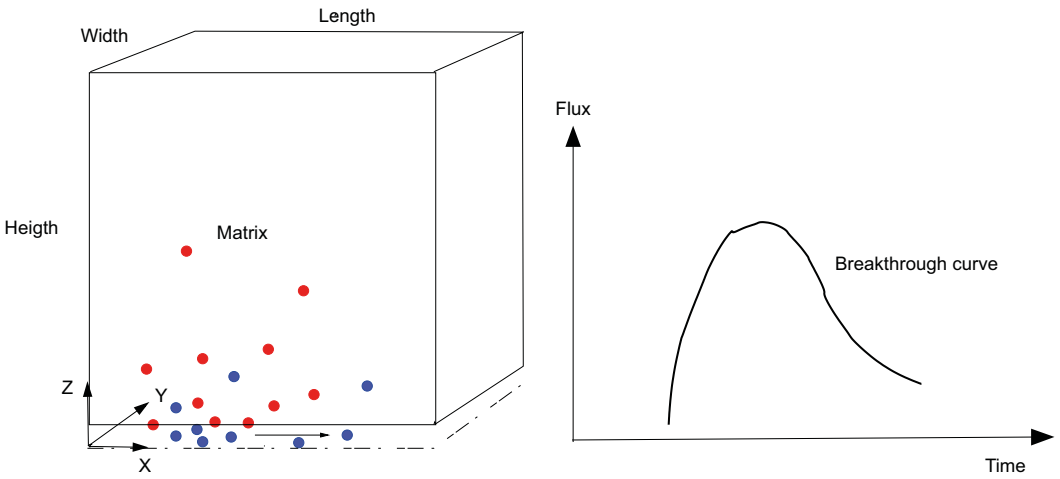

Figure A4-1. *The situation considered is a channel-matrix system, where particles are introduced at the upstream end of the channel. Particles can either be sorbed (red) or free to move (blue) by advection and diffusion. At the downstream end, the flux of particles results in a breakthrough curve.*

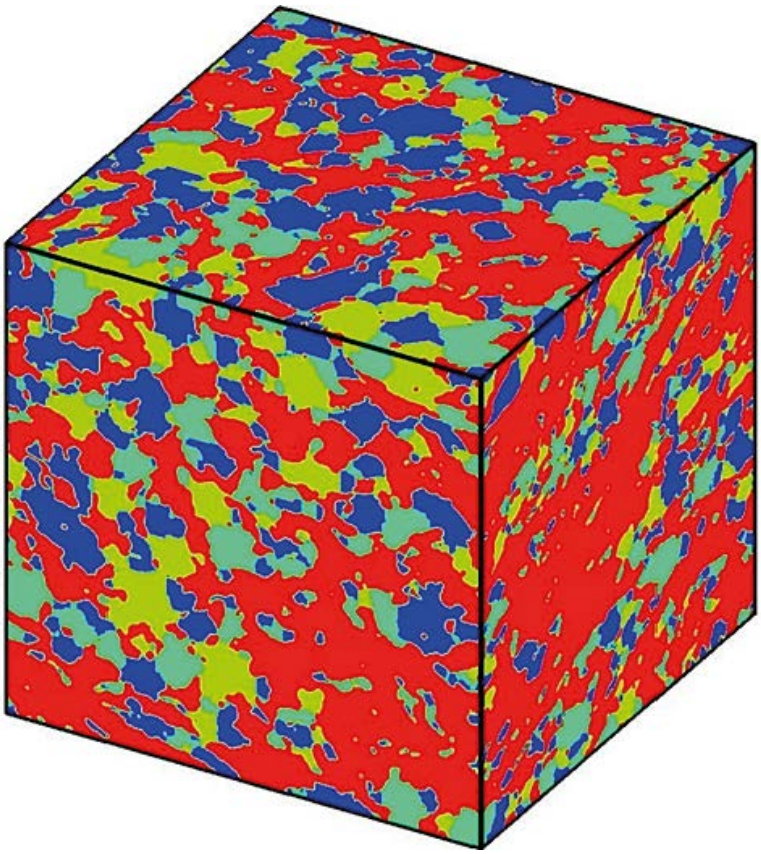

Figure A4-2. *Three-dimensional visualization of the considered veined gneiss (VGN) rock sample after mineral segmentation. The size of the sample is 1 cm^3. The mineral phases shown are quartz (blue), plagioclase (green), K- feldspar (yellow) and mica (red). Mica is considered to be the only reactive mineral.*

A4.2 Methodology and model

A4.2.1 Conceptual description of the channel-matrix system

The situation studied is shown in Figure A4-1. A number of processes and conditions may influence the shape of the BTC, the most important of which are listed below:

- Advection: particles are transported by advection from the inlet to the outlet. In the channel a velocity profile will develop, due to friction at the channel wall. Advection in the matrix can be neglected;
- Molecular diffusion: molecular diffusion will act in all three directions, both in the channel and in the matrix;
- Taylor dispersion: the combined effect of a velocity profile and molecular diffusion will result in a longitudinal dispersion, called Taylor dispersion. It can be shown that this effect is negligible for the cases under investigation;
- Sorption on the channel wall: reactive grains will be exposed to the channel and hence provide very accessible sorption sites;
- Matrix diffusion: particles will diffuse into and out of the matrix and may get sorbed on the surfaces of reactive grains;
- Mineral distribution in the matrix; different rocks have different mineral distributions (grain sizes, grain types, etc). See Figure A4-2 for an example.

The shape of the BTC is affected by all processes to a varying degree.

A4.2.2 Conceptual description of the transport model

The description of the model is taken from Svensson et al. (2019a):

Different mineral surfaces react differently to different radionuclides. This is the basic concept of the numerical model to be presented. It is then realized that the model requires, as input, a three-dimensional mineral map and information about how a certain radionuclide reacts with a range of minerals. Note that this is not information that is provided by the traditional distribution coefficients K_d and K_a.

The basic parameters of the model can now be introduced. When a particle is close to a reactive mineral surface, it has a certain probability, P_s, to get sorbed within a certain time interval, T_s. If sorbed, it will stay so for a time, T_d, before desorbed. An immediate question that arises is what "close" means in this context. We are developing a numerical method and it will be assumed that a particle may get sorbed when it is in a computational cell that has one or more cell faces in contact with a reactive grain. The cell size, Δ, is hence a model parameter.

If we consider that the events of being sorbed are distributed according to an exponential density function with parameter k_1, then:

$$\begin{aligned} F\left(X\right) &= \exp\left(-k_1 * X\right) \qquad \text{if } X \geq 0 \\ F\left(X\right) &= 0 \qquad\qquad\qquad\quad \text{if } X < 0 \end{aligned} \tag{A4-1}$$

where X is a continuous random variable.

Then the probability P_s that the particle gets sorbed before T_s is given by:

$$P_s = P\left(X \leq T_s\right) = 1 - \exp\left(-k_1 * T_s\right) \tag{A4-2}$$

which gives:

$$k_1 = -Log\left(1 - P_s\right) / T_s \,. \tag{A4-3}$$

Now consider that the events of being desorbed are distributed according to an exponential density function with parameter k_2. The mean time before release is given by:

$$T_d = E\left(X\right) = 1 / k_2 \,. \tag{A4-4}$$

This means:

$$k_2 = 1 / T_d \,. \tag{A4-5}$$

k_1 and k_2 are the numerical input parameters of the model.

When putting numbers to the four parameters (P_s, T_s, T_d and Δ) one should note that they are related (see Svensson et al. 2019a). The cell size is considered as fixed and T_d will be a calibration parameter. Hence, we need to put numbers to P_s and T_s:

- P_s: if one out of six cell walls are in contact with a sorbing mineral the probability to get sorbed is 1/6. However, more cell surfaces can be in contact with a mineral so we chose to put $P_s = 0.2$.
- T_s: the time to leave a cell by molecular diffusion is specified for $T_s \left(= (\Delta/2)^2 / D_{mol}\right)$.

It should be emphasized that the values chosen for P_s and T_s will influence T_d. It is thus not possible to interpret T_d as the time a particle actually stays sorbed.

The particle tracking method used is Time Domain Random Walk (TDRW) (Russian et al. 2016). The method is implemented for both advection and diffusion in the code used (DarcyTools, Svensson and Ferry 2014).

A4.2.3 Model Setup

The computational methods used are given in Svensson et al. (2019b). The key element is the generation of a micro-DFN (Discrete Fracture Network) in the intergranular space, i.e., the space between individual grains. Fractures in the network are given properties (aperture, diffusivity, etc) and diffusive pathways into the matrix are hence generated. The computational grid will only cover the pathways, as there is no need to consider diffusion into the grains (here assumed to be insignificant). Figure A4-3 shows a typical grid. The pathways are connected in three dimensions even though the figure may give a different impression. Areas with no grid cells represent grains. When a particle is in a cell with reactive properties, it may get sorbed. The colours in the cells indicate the grain type. The dark blue cells at the low-z coordinate represent the flow channel.

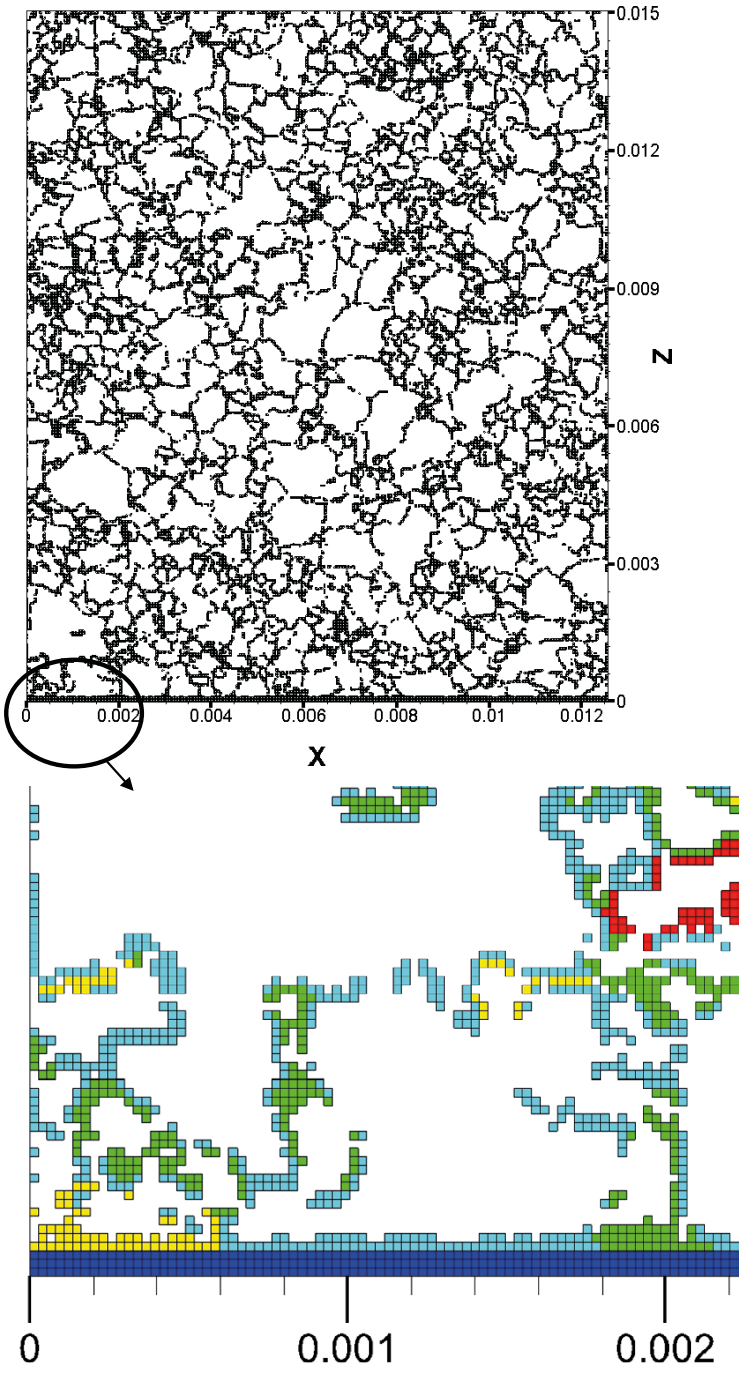

Figure A4-3. A typical computational grid. In the enlargement (bottom) the cells have been coloured according to grain type. Dark blue cells represent the channel. Coordinates in [m]. The cell size is 27.16 µm in all simulations.

A4.2.4 Input data

The X-ray data to be used are given by the file VGN323_grain_map_27.16µm_635x635x469.txt. (Input data to Task 9). The veined gneiss map, shown Figure A4-2, has a resolution of 27.16 µm.

A4.3 Results

A4.3.1 Reference Case

Results will be presented as a reference case, followed by a number of sensitivity cases. The reference case is defined by the following points (see also Figure A4-1):

- Length = 12.5 mm, Height = 15 mm, Width =10 mm.
- Half aperture = 0.108 mm.
- Velocity = 3×10^{-7} m/s (≈ 10 m/year), uniform.
- Molecular diffusion coefficient 10^{-9} m^2/s.
- Time before desorption T_d : 0 → 10 000 s. Particles introduced as a Dirac pulse. T_d = 1 000 is considered to represent a tracer with medium sorption strength; T_d = 100 represents a weakly sorbing tracer; and T_d = 10 000 represents a strongly sorbing tracer.

The VGN-block was tested separately (by solving a steady diffusion equation) to tune the micro-DFN (effective diffusion coefficient, $D_{eff} = 1.0 \times 10^{-13}$ m^2/s, Mean porosity, ε = 0.47 %).

BTCs for a range of T_d:s are shown in Figure A4-4. It is found that T_d = 1 gives a BTC that is close to the one that represents a conservative tracer. T_d = 10 000 gives a peak time of about 3×10^7 s, which is one year. One may also note that a late time slope of −3/2 is calculated for all curves; this will be further analysed in the discussion section. The distribution of particles at T_{peak} is the presented in Table A4-1. For $T_d > 10$ more than 47.2 % of the particles are sorbed on the channel wall.

The BTCs are intended to represent a case with an infinite matrix. However, in a numerical simulation a finite depth must be used. This raises the question of the boundary condition at the boundary defining the depth of the matrix. Two common types are “reflexion” and “removal” of particles. The correct boundary condition, it can be argued, is somewhere in between these two limits. In Figure A4-5 two BTCs are shown, each with a different type of boundary condition. For all the results presented in this report, we run the simulation for both boundary conditions and only present curves up to the time when there is a difference. It can then be claimed that results are independent of the upper boundary condition.

From Table A4-1 it was found that a large fraction of the particles is sorbed on the channel wall. An illustration of the particle distribution at T_{peak} is given by Figure A4-6. As expected, particles are located according to the mineral distribution at the channel wall. One may also note that the penetration depth for this case is about 2 mm and thus far from the upper boundary (at 15 mm).

Table A4-1. Reference Case. Distribution of particles at T_{peak} (in %).

T_d [s]	T_{peak} [s]	In Matrix	Sorbed on wall	Flowing	Left domain
0	2.8×10^4	3.1	-	67.1	29.8
1	3.1×10^4	4.2	11.8	55.3	28.7
10	7.8×10^4	6.5	47.2	14.7	31.6
100	5.1×10^5	7.6	65.7	2.3	24.4
1 000	5.1×10^6	7.7	65.7	0.2	26.4
10 000	4.5×10^7	7.8	71.3	0.02	20.9

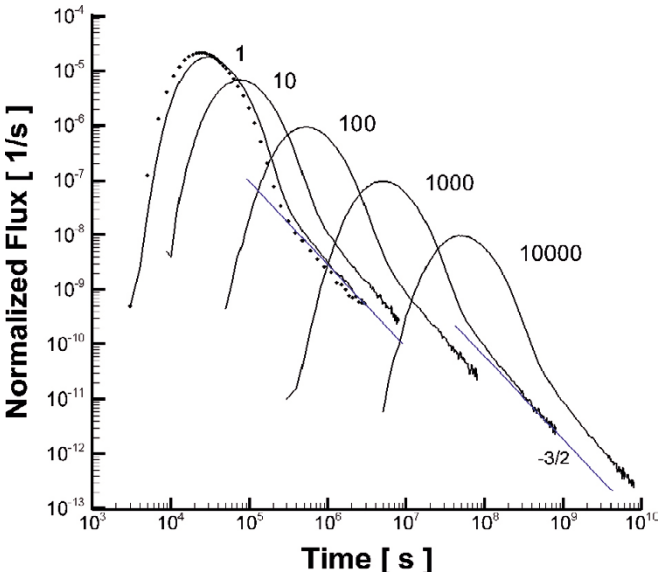

Figure A4-4. *BTCs for a range of T_d values. Dots give the BTC for a non-sorbing tracer. Blue lines indicate a late-time slope of −3/2.*

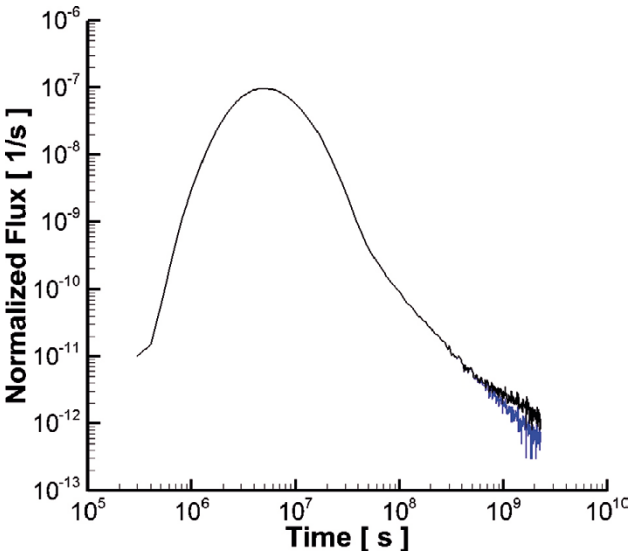

Figure A4-5. *BTCs with differing upper boundary conditions: the black curve shows the flux through the outlet plus the upper boundary (removal condition); the blue curve gives the flux for the reflexion condition.*

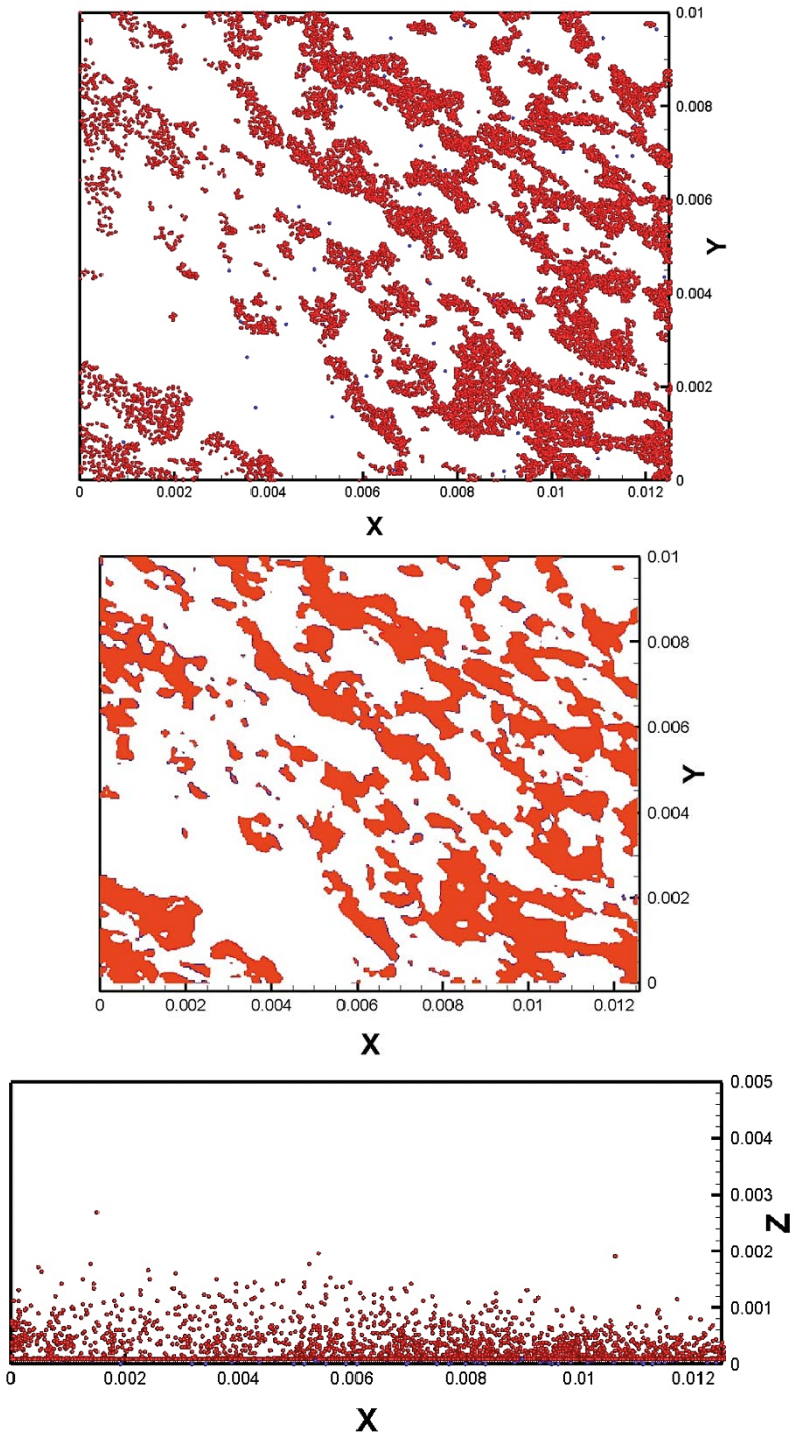

Figure A4-6. *The sorption pattern on the channel wall (top) and distribution of reactive grains (mica) on the channel wall (middle). Penetration of particles into the matrix (bottom). All plots are for the reference case at the time of the peak in the BTC.* T_d *= 1 000 s.*

A4.3.2 Sensitivity studies

E. Above in Section A4.2, a list of processes affecting the BTC was given. Next, a set of simulations that quantitatively shows the effect on the BTC will be presented. The reference case, with T_d = 1 000, is used for comparison. Six figures, A to F, are shown in

Figure A4-7. These will be commented on one by one:

A. In this simulation the mean velocity was changed. A higher velocity will result in a higher peak as there is less time to penetrate the matrix.

B. In this simulation a velocity profile was introduced, while keeping the mean velocity the same. No effect on the BTC is found. This can be understood by noting that the time needed for a particle to be transported by diffusion across the channel is about 1 s. This is actually the reason why Taylor dispersion is insignificant.

C. Sorption on the channel wall is neglected. A dramatic effect is generated. Clearly, it is the easily accessible sorption sites that give the effect.

D. The matrix is neglected. The peak is the same, but the tail will disappear. It is the matrix that generates the part with a late time slope of −3/2.

E. In this simulation we neglected $D_{mol,x}$ in the channel. This will affect the peak region, while the tail is unaffected.

F. In this simulation the domain length was increased from 12.5 to 100 mm. It is not surprising that the peak is found at a later time and is reduced; there is simply more time to penetrate the matrix. Some details are given in Table A4-2. In order to generate a longer channel, the grain map is repeated several times. The resulting grid is outlined in Figure A4-8, where the porosity field can also be studied.

Table A4-2. Table 3-2. Increasing the domain length. Distribution of particles at T_{peak} (in %).

Length [mm]	T_{peak} [s]	In Matrix	Sorbed on wall	Flowing	Left domain
12.5	5.1×10^6	7.7	65.7	0.2	26.4
25	1.4×10^7	10.7	47.5	0.2	41.6
50	2.8×10^7	15.1	43.5	0.2	41.2
100	6.2×10^7	20.4	42.0	0.2	37.4

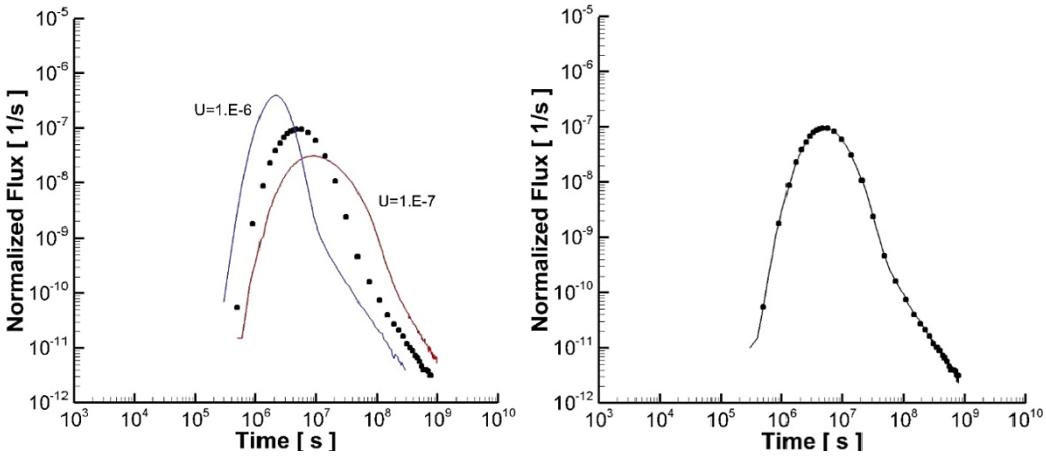

A. Changing mean velocity.

B. Introducing a velocity profile.

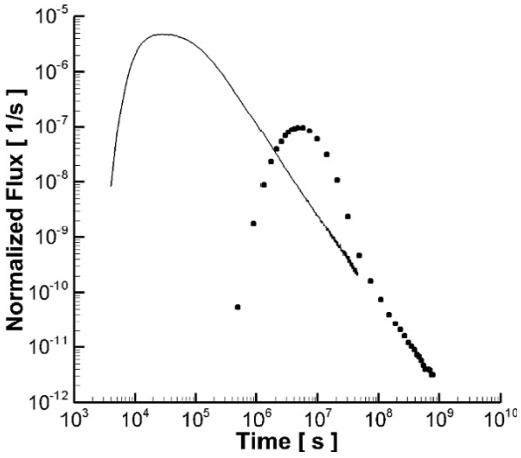

C. Neglecting sorption on the channel wall.

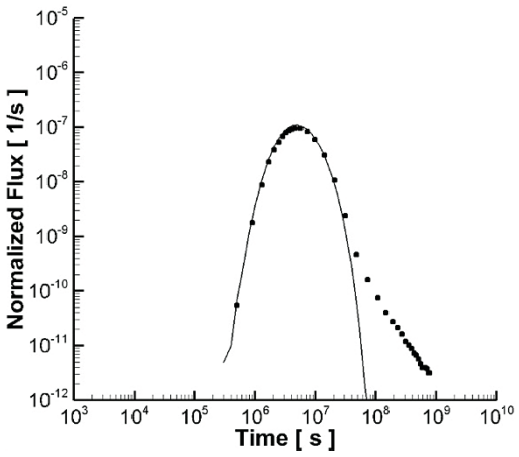

D. Neglecting the matrix (only surface sorption).

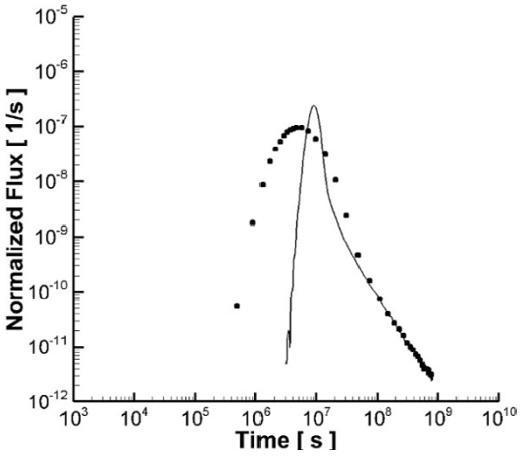

E. Neglecting $D_{mol,x}$ in the channel.

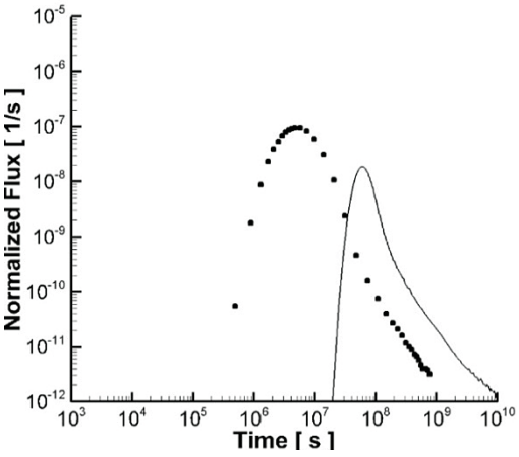

F. Increasing domain length to 100 mm.

Figure A4-7. *Sensitivity cases as described in Section A4.3.2. Dots give the reference case.*

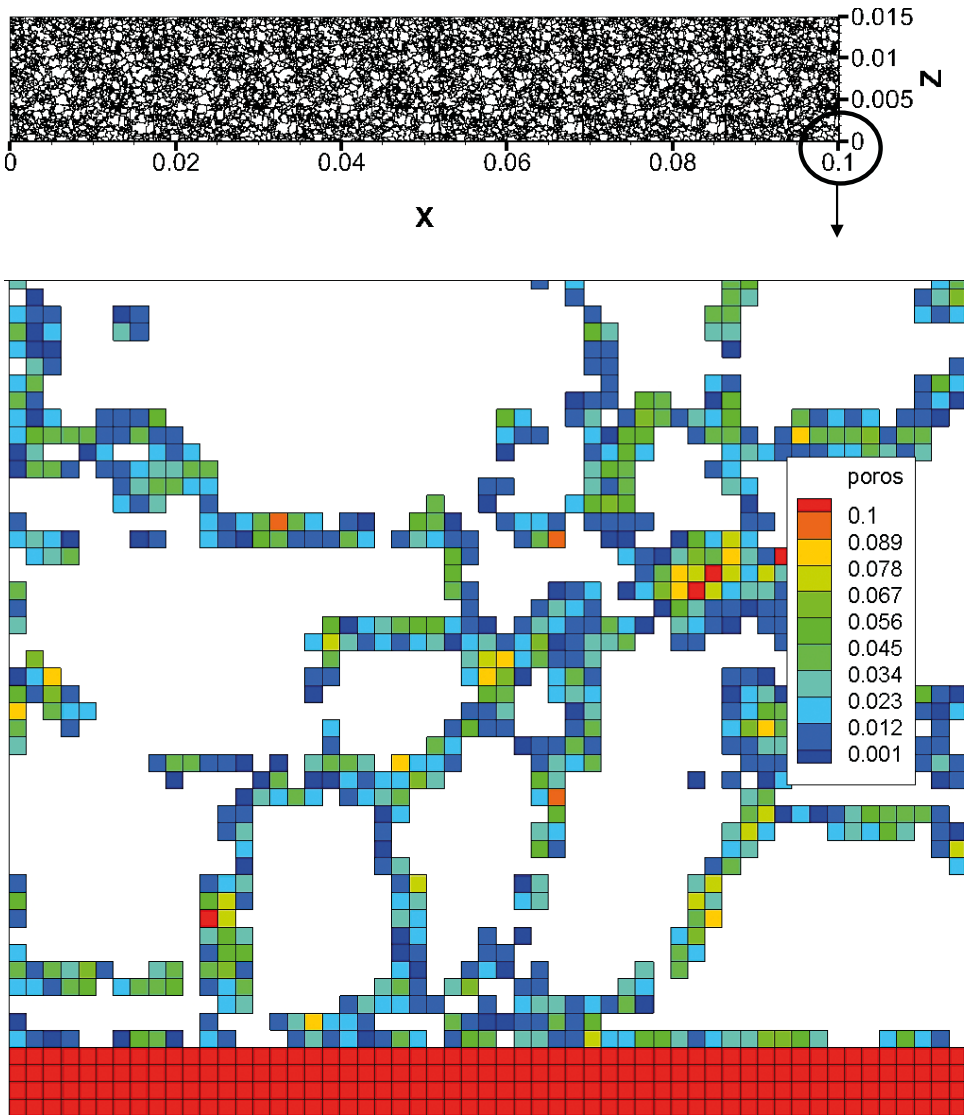

Figure A4-8. *Grid produced by increasing the domain length. Computational grid for a 100 mm long domain (top) and an enlargement (bottom). In the enlargement, cells are coloured according to their porosity.*

A4.4 Discussion

A4.4.1 Introduction

The model and the results presented can be called “a theoretical study of the BTC” as no experimental data is considered. As such, it is of interest to evaluate if analytical solutions can support the simulations. From Figure A4-4 two features of the BTC:s can be noted; the late time slope is in most cases −3/2 and the effect of sorption on the channel wall is important (Figure A4-6). In this section these features will be discussed.

A4.4.2 The infinite homogeneous matrix

The BTCs show a late time slope of −3/2. This is excepted, as the matrix is statistically homogeneous (locally heterogeneous). Next, we compare the BTCs with the analytical solution given by, for example, Cvetkovic et al. (1999) and Neretnieks (2002):

$$m = \Theta(t-\alpha)\frac{\gamma}{2\sqrt{\Pi}}(t-\alpha)^{-3/2}\exp\left(-\frac{\gamma^2}{4(t-\alpha)}\right)$$

where m is mass flux at the outlet, $\Theta(t)$ Heaviside step function and t time. The two parameters α and γ are defined as:

$$\alpha = R_m\theta_m L/q,$$

$$\gamma = L\delta_f\theta_{im}\sqrt{D_w R_{im}}/q$$

where L is the domain length, q the velocity, Θ_{im} porosity in the matrix, D_w molecular diffusivity of water, δ_f one over half aperture, R_m retention parameter in channel and R_{im} retention parameter in the matrix.

In Figure A4-9 we compare this solution with the "no molecular diffusion in the flow direction" case (Figure A4-7E), as the analytical solution makes this assumption. Two retention parameters were used for calibration; R_m = 210 and R_{im} = 15. R_m is used to fit the time of the peak. We may note that the present model also moves the peak with a factor of 200, as compared to the case without sorption (see Figure A4-4). R_{im} will control the late time region.

We conclude from this case that the late time region is in good agreement between the two models, while the peak region is different. This is not surprising, as we are comparing two models that are based on very different concepts. The analytical solution gives a sharper peak.

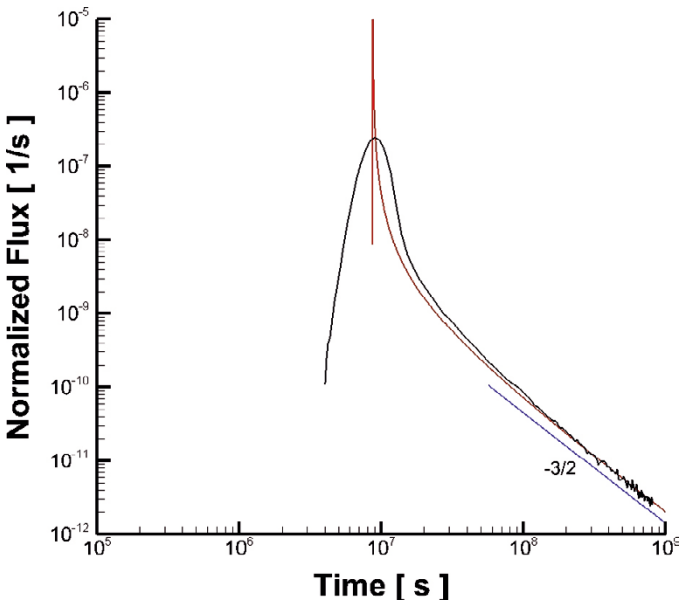

Figure A4-9. *Comparison with the analytical solution for a homogeneous matrix (red curve). In the numerical solution the molecular diffusion coefficient in the flow direction was set to zero.*

A4.4.5 The one-dimensional two rate solution

The BTCs are significantly affected by sorption on the channel wall (see Table A4-1 and Table A4-2). Next, we compare the BTCs with an analytical solution that considers only surface sorption, given by Selroos and Cvetkovic (1992) or Svensson (1994). The case is outlined below and illustrated in Figure A4-10. Particles are injected at the upstream end of a channel and are advected by a velocity u. The particles can be adsorbed and desorbed with specified rates. The BTC at the outlet is studied.

How can the BTC be characterized, based on the following parameters?

λ_a = adsorbtion rate [s^{-1}]

λ_d = desorbtion rate [s^{-1}]

t_f = travel time without adsorbtion [s]

From Appendix 1:

$$\mu_{T_{tot}} = t_f + t_f \lambda_a / \lambda_d$$
$$\sigma_{T_{tot}} = \sqrt{2\lambda_a t_f} / \lambda_d$$
$$\mu_N = \lambda_a t_f$$

where $\mu_{T_{tot}}$ is the expected value of the total travelling time and $\sigma_{T_{tot}}$ its standard deviation. μ_N is called the shape number.

We calculate the BTC for a case that is similar to the reference case (L = 12.5 mm, u = 3×10^{-7} m/s, λ_a = 2.48, λ_d = 1/1 000) (see Figure A4-11). A perfect agreement is found; $\mu_{T_{tot}}$ is 1.04×10^8 for both solutions and $\sigma_{T_{tot}}$ is 4.5×10^5 for the analytical solution and 4.7×10^5 for the numerical.

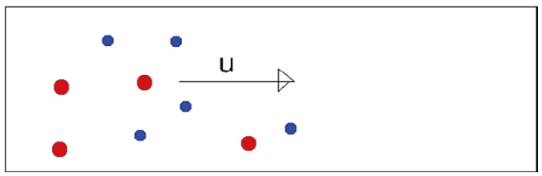

Figure A4-10. *Outline of the situation studied. Red particles are sorbed.*

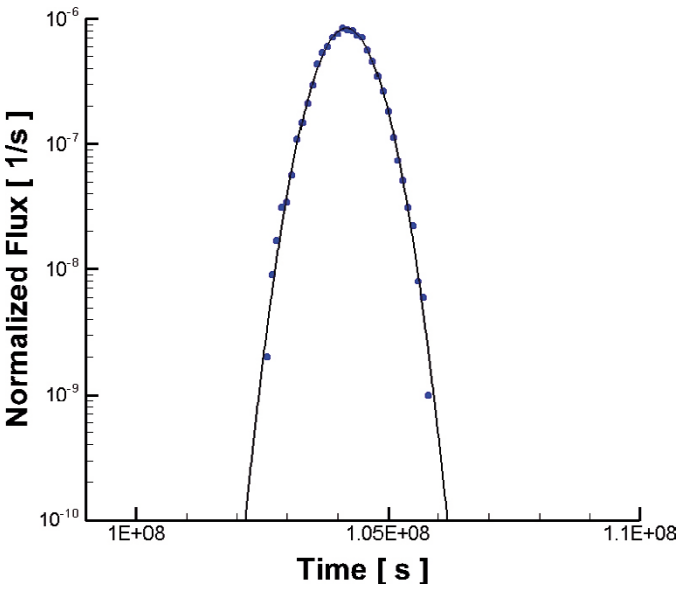

Figure A4-11*. A one-dimensional adsorption/desorption case. Calculated BTC (dots) and a Gaussian distribution with the calculated standard derivation.*

As there are no adjustable parameters in this case, we can consider it as a verification of the adsorption/desorption features of the simulation model.

A4.5 Summary and Conclusion

The reactive particle tracking method presented in Svensson et al. (2019a) has been applied to the channel-matrix system. The method is based on grain-maps and sorbing tracers are assumed to react to specific grains with two rates.

Specific results from this study:

- BTCs for a range of T_d values are shown;
- A late-time slope of −3/2 is found, for most cases;
- Surface sorption is a dominating process;
- The sensitivity to various assumptions and processes are shown;
- Increasing the domain length increases the fraction of particles in the matrix. The fraction at the channel wall is still high;
- Comparisons with analytical solutions are discussed.

As a general conclusion, one may state that the model presented in Svensson et al. (2019a, b) produces also interesting results for the channel-matrix system.

A4.6 Additional material

PARTICLE TRAVELLING TIME DISTRIBUTION IN THE FIRST ADSORPTION/ DESORPTION DISPERSION MODEL

(Derivation by Hans-Olof Kuylenstierna)

In this section we shall introduce a dispersion model with an adsorption/desorption mechanism. In particular, we shall study the probability distribution of the travelling time of a particle that moves according to the model.

In our model we assume that a particle travels from a point A to a point B. On its way the particle can get adsorbed, which means that it stops moving. After some time it will get desorbed, which means that it becomes free to move again. We assume that the adsorption and desorption processes have rates λ_a and λ_d, respectively. I.e., if the particle is free (adsorbed), the probability that it will get adsorbed (desorbed) within the infinitesimal length of time dt is $\lambda_a\, dt$ ($\lambda_d\, dt$). λ_a and λ_d are assumed to be constant and positive.

We do not specify what rules govern the motion of the particle when it is free. However, we must require that this motion is only suspended and not otherwise affected by the adsorption delays. Specifically, the portion of the total travelling time from A to B during which the particle is free must not be affected by the adsorption/desorption process. (We can note that this condition is normally not satisfied if the velocity of the particle when it is free depends explicitly on time.) Without this requirement the following analysis would not be valid.

Let T_{tot} be the total travelling time of the particle from A to B. T_{tot} is the sum of t_f and T_a, the portions of time during which the particle is free and adsorbed, respectively. Let N be the number of adsorption delays during the travel and let T_{a1}, ..., T_{aN} be the lengths of the adsorption delays, so that $T_a = T_{a1} + \mathrm{K} + T_{aN}$. T_{tot}, T_a, N and T_{a1}, K, T_{aN} are stochastic variables while t_f is an ordinary number.

Our aim during the remainder of this chapter shall be to derive expressions for the density function, expected value and standard deviation of T_{tot}.

From the assumptions made we can conclude that N has a Poisson distribution with expected value $\lambda_a t_f$, that T_{a1}, K, T_{aN} have an exponential distribution with rate λ_d, and that N and T_{a1}, ..., T_{aN} are all independent. Letting P_N denote the probability mass function of N and $f_{T_{ak}}$ the (equal) probability density functions of the T_{ak}, $1 \le k \le N$, we have

$$p_N(n) = e^{-\lambda_a t_f} \frac{(\lambda_a t_f)^n}{n!}, n \ge 0,$$

$$\mu_N = E[N] = \lambda_a t_f,$$

$$\sigma_N^2 = \mathrm{Var}(N) = \lambda_a t_f,$$

$$f_{T_{ak}}(t) = \lambda_d e^{-\lambda_d t}, t \ge 0, 1 \le k \le N,$$

$$\mu_{T_{ak}} = E[T_{ak}] = \frac{1}{\lambda_d}, \quad 1 \le k \le N,$$

$$\sigma_{T_{ak}}^2 = \mathrm{Var}(T_{ak}) = \frac{1}{\lambda_d^2}, 1 \le k \le N.$$

If N were known, $N = n$, T_a would have a gamma distribution with parameters n and λ_d, as T_a would be the sum of the n independent stochastic variables T_{a1}, ..., T_{an} each of which has an exponential distribution with rate λ_d (see Ross 1985, pp 194–195). Therefore the conditional probability density function of T_a given that $N = n$ is

$$f_{T_a|N}(t,n) = \begin{cases} \dfrac{\lambda_d (\lambda_d t)^{n-1} e^{-\lambda_d t}}{(n-1)!}, t \ge 0, n > 0 \\ \delta(t), n = 0 \ . \end{cases}$$

(Concerning the gamma distribution, see Ross (1985, pp 33–34). denotes the Dirac function, which we use to indicate that $T_a = 0$ with probability 1 if $n = 0$.)

Taking into account that N has a Poisson distribution with expected value $\lambda_a t_f$, we have

$$f_{T_a}(t) = \sum_{n=0}^{\infty} p_N(n) f_{T_a|N}(t,n) =$$

$$= e^{-\lambda_a t_f} \left[\delta(t) + \sum_{n=1}^{\infty} \frac{(\lambda_a t_f)^n}{n!} \times \frac{\lambda_d (\lambda_d t)^{n-1} e^{-\lambda_d t}}{(n-1)!} \right] =$$

$$= \lambda_a t_f e^{-\lambda_a t_f} \left[\delta(\lambda_a t_f \lambda_d t) + \sum_{n=1}^{\infty} \frac{(\lambda_a t_f \lambda_d t)^{n-1}}{(n-1)! n!} \right] \lambda_d e^{-\lambda_d t} =$$

$$= \lambda_a t_f e^{-\lambda_a t_f} q(\lambda_a t_f \lambda_d t) \lambda_d e^{-\lambda_d t}, t \ge 0,$$

if we use the relation $a\delta(ax) = \delta(x)$ and put

$$q(x) = \delta(x) + \sum_{n=1}^{\infty} \frac{x^{n-1}}{(n-1)! n!} = \delta(x) + \frac{I_1(2\sqrt{x})}{\sqrt{x}},$$

where I_1 is the modified Bessel function of the first kind and order 1 defined by

$$I_1(x) = \sum_{n=1}^{\infty} \frac{x^{2n-1}}{2^{2n-1}(n-1)! n!}$$

(see e.g. Weast 1989, p A-99).

As N and T_{a1}, K, T_{aN} are independent and T_{a1}, K, T_{aN} are equally distributed, we have

$$E\left[\sum_{k=1}^{N} T_{ak}\right] = E[N]E[T_{a1}]$$

and

$$\mathrm{Var}\left(\sum_{k=1}^{N} T_{ak}\right) = E[N]\,\mathrm{Var}(T_{a1}) + (E[T_{a1}])^2\ \mathrm{Var}(N)$$

according to two relations in Ross (1985, pp 95–96 and 98–99). Hence

$$\mu_{T_a} = E[T_a] = E\left[\sum_{k=1}^{N} T_{ak}\right] = E[N]E[T_{a1}] =$$

$$= \lambda_a t_f \times \frac{1}{\lambda_d} = \frac{\lambda_a t_f}{\lambda_d},$$

$$\sigma^2_{T_a} = \mathrm{Var}(T_a) = \mathrm{Var}\left(\sum_{k=1}^{N} T_{ak}\right) =$$

$$= E[N]\mathrm{Var}(T_{a1}) + (E[T_{a1}])^2\,\mathrm{Var}(N) =$$

$$= \lambda_a t_f \times \frac{1}{\lambda_d^2} + \left(\frac{1}{\lambda_d}\right)^2 \times \lambda_a t_f = \frac{2\lambda_a t_f}{\lambda_d^2}.$$

As $T_{tot} = t_f + T_a$ we have

$$f_{T_{tot}}(t) = f_{T_a}(t - t_f) =$$

$$= \lambda_a t_f e^{-\lambda_a t_f} q(\lambda_a t_f \lambda_d (t - t_f))\lambda_d e^{-\lambda_d (t - t_f)}, t \geq t_f,$$

$$\mu_{T_{tot}} = t_f + \mu_{T_a} = t_f + \frac{\lambda_a t_f}{\lambda_d},$$

$$\sigma^2_{T_{tot}} = \sigma^2_{T_a} = \frac{2\lambda_a t_f}{\lambda_d^2}.$$

The parameters in the expression for $f_{T_{tot}}(t)$ are t_f, λ_a and λ_d. From the expression we can see that the shape of $f_{T_{tot}}$'s graph is completely determined by the number $\mu_N = \lambda_a t_f$, except for translation and contraction along the t axis controlled by t_f and λ_d.

Appendix 5

TD Task 9D (modified Data Delivery 32) – SKB Task Force on modelling of groundwater flow and transport of solutes

Increasing the realism in solute transport modelling – Modelling the field experiments of REPRO and LTDE-SD (Task 9)

Task description – 9D1 and 9D2

J. Crawford

Technical committee of Task 9

Kersti Nilsson, Geosigma

Björn Gylling, Gylling GeoSolutions

James Crawford, Kemakta

Lasse Koskinen, Posiva

Antti Poteri, Posiva

Jan-Olof Selroos, SKB

September 2018

Updated May 2019

Updates marked with gray

A5.1 Introduction

Task 9D is the fourth subtask of Task Force GWFTS Task 9 and will focus on extrapolating results from in situ experimental conditions to something more closely resembling a typical Safety Assessment (SA) scenario. The Task 9D work may be considered to be a set of Synthetic Safety Assessment case studies. The task will be divided into several exercises of increasing complexity, ranging from a hypothetically extended version of Task 9A in Task 9D1 to more complex safety assessment calculations as later subtasks. The number of sub-tasks may be pending on the outcome in the previous sub-task, and continuing interest from the modellers/organisations to proceed.

A preliminary roadmap for the Task is:

Task 9D1 – Based on Task 9A, i.e. REPRO WPDE 1 and 2, but extruded geometry with assumed constant hydrodynamic properties as a function of flowpath length, SA conditions, and simplified source term. A single rock type (VGN) is assumed for this subtask and a set of hypothetical solutes with differing sorptive and (non-chain) decay properties.

Task 9D2 – As Task 9D1, but for the radium (4n+2) decay chain.

A summary of the proposed work for Task 9D1 and 9D2 subtasks is given in Table A5-1 and is based on the discussions in the subsequent sections.

Table A5-1. Summary of proposed Task 9D1 and 9D2 modelling cases. Orange shading indicates modelling group can choose how they derive the model parameters.

	Fracture	Matrix	Source term	Solutes	Decay
1a	Moderate dispersion	Constant average properties	Extended 1 ka pulse flux	1 non-sorbing 1 weakly sorbing 1 moderately sorbing 1 strongly sorbing	No
1b	Moderate dispersion	Constant average properties	Constant flux	1 non-sorbing 1 weakly sorbing 1 moderately sorbing 1 strongly sorbing	Yes
1c	Moderate dispersion	Variable properties	Extended 1 ka pulse flux	1 non-sorbing 1 weakly sorbing 1 moderately sorbing 1 strongly sorbing	No
1d	Moderate dispersion	Variable properties	Constant flux	1 non-sorbing 1 weakly sorbing 1 moderately sorbing 1 strongly sorbing	Yes
2a	Moderate dispersion	Constant average properties	Constant flux	U-238 (4n+2 chain)	Yes
2b	Moderate dispersion	Variable properties	Constant flux	U-238 (4n+2 chain)	Yes

A5.2 Tentative description of Task 9D1

In Task 9D1, it is proposed that the REPRO experiments (WPDE 1 and 2) be used as a basis for the work. Material property data (e.g. D_e, e_p, and K_d) should reflect the same local geological characteristics of the REPRO test site, although considering a flowpath of length on the order of 1 000 m and a range of F-factors 2-4 orders of magnitude larger than that achieved in the WPDE-1 experiment. Hydrodynamically, this can be considered to be a synthetic Safety Assessment-like setting, although with much simplified features relative to what might be expected in a real-world situation.

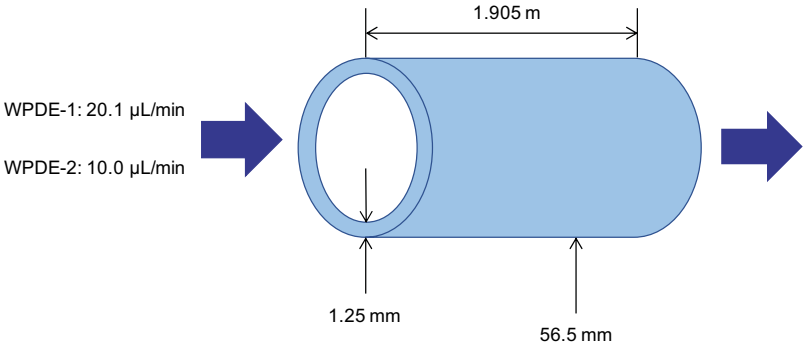

Figure A5-1. *Schematic overview of REPRO experimental setup.*

A5.2.1 Hydrodynamic conditions for Task 9D1

From the thickness of the annulus and outer diameter of the experimental section shown in Figure A5-1, the cross-sectional area of the annulus is calculated to be 2.17×10^{-4} m^2. For the specified flowrates in both experiments, the relevant hydrodynamic parameters of the WPDE experiments are as given in Table A5-2.

Table A5-2. Hydrodynamic parameters characterising the WPDE in situ experiments (note: that the F-factor is calculated considering the outer perimeter of the annulus only; the inner, inert dummy surface does not participate in matrix uptake).

	WPDE-1	WPDE-2
q (m^3/y)	1.05×10^{-2}	5.26×10^{-3}
v (m/y)	48.48	24.24
t_w (y)	0.0393	0.0786
F (y/m)	32.14	64.29

In SR-Site (SKB 2010, Table 4-3), typical flowpath F-factors associated with failing canisters varied between about 1.5×10^4 y/m and 10^5 y/m while the central corrosion case considered an F-factor just over 5.0×10^4 y/m. For Task 9D we propose the same F-factor as in the SR-Site central corrosion case as being approximately representative of SA conditions. For a 2-sided flow channel of width W_c (m) and length L (m), the F-factor (y/m) can be defined as:

$$F = \frac{2W_c L}{q} = \frac{2t_w}{\delta_t} = \frac{2L}{v\,\delta_t} \tag{A5-1}$$

Where, δ_t (m) is the transport aperture, q (m^3/y) is the flowrate, t_w (y) is the advective travel time, and v (m/y) is the superficial flow velocity. For an annular geometry where diffusion occurs radially over the outer diameter as in the WPDE experiments, the F-factor is defined as:

$$F = \frac{\pi \delta_a L}{q} \tag{A5-2}$$

When mapping a flat fracture plane (with two bounding matrix surfaces) to a radial diffusion symmetry (with a single outer surface for diffusive exchange), the following relation can be assumed between the flow-channel width, W_c and effective radial diameter of an equivalent cylinder, δ_a:

$$W_c = \frac{\pi}{2}\delta_a \tag{A5-3}$$

To preserve the same cross-sectional area, the flow channel aperture in the planar flow channel is then roughly twice that of the annulus:

$$\delta_t = \frac{1}{2}\left(\frac{d_0^2 - \left(d_0 - 2\delta_{t(\mathrm{an})}\right)^2}{d_0} \right) \approx 2\delta_{t(\mathrm{an})} \tag{A5-4}$$

Where, d_0 (m) is the outer diameter of the borehole in the WPDE test section, $\delta_{t(an)}$ (m) is the aperture of the WPDE annulus, and δ_t (m) is the transport aperture of the equivalent planar flow channel. The equivalent flow channel width corresponding to the WPDE experimental section (via Equation A5-3) is therefore equal to 8.87 cm and the transport aperture is 2.445 mm. For a 1 000 m flowpath length, flow channel width of 8.87 cm and assuming the same average transport aperture as in the WPDE experiments, the F-factor to be modelled corresponds to the flowrate, flow velocity, and advective travel time given in Table A5-3.

Table A5-3. Flowrate, velocity, and advective travel time corresponding to a typical Safety Assessment scenario for the KBS-3 system based on the central corrosion case of SR-Site (SKB 2010) assuming a flowpath of 1 000 m length and 8.87 cm average flow channel width.

Parameter	Value
F (y/m)	5×10^{4}
q (m^3/y)	3.55×10^{-3}
v (m/y)	16.36
t_w (y)	61.12

Calculations should consider a case including a moderate amount of hydrodynamic dispersion (say, Pe = 10). It is left up to the individual modelling groups to decide both the magnitude and mode of dispersion (i.e. whether it is modelled as a Fickian process, or by differences in advective travel times). Since both approaches represent very different modelling philosophies regarding the physical interpretation of dispersion, it is proposed that a case featuring low hydrodynamic dispersion (Pe ³ 100) could also be simulated by those groups that find this feasible in their numerical implementations of their transport model although is an optional subtask.

The rock matrix may be simulated as an unbounded medium, or one of limited extent. This choice is left up to the individual modelling teams to decide depending on the underlying assumptions in their model of rock matrix heterogeneity, numerical limitations of their modelling tool, and the particular hydrodynamic conditions simulated. If a bounded rock matrix is modelled, a motivation for the particular depth chosen in the modelling work should be provided.

The SA case study to be modelled should consider diffusion to the rock matrix from both flanking fracture surfaces bounding the flow channel, although symmetry may be invoked to simplify the problem. Since the aim of the task is to address aspects of heterogeneity and microstructure, diffusive uptake to the rock matrix should be modelled as a rectilinear process only and radial diffusion from the narrow flow-channel should not be considered. Rock matrix heterogeneity both parallel to and orthogonal to the flow direction may be considered. The choice as to whether the rock matrix is modelled as an isotropic or anisotropic medium is also left up to the individual modelling teams to decide. For groups that find it impractical to model a path length of 1 000 m, any path length may be modelled provided it possesses the same hydrodynamic characteristics (i.e. F and t_w) as those specified in Table A5-3.

A5.2.2 Geological setting for Task 9D1

Since the primary purpose of Task 9D is to evaluate issues related to scale-up of the rock volume sampled in the REPRO experiments to a synthetic safety assessment-like setting, the same geological features can be assumed to exist in this subtask as in Task 9A and Task 9C. Since the dominant rock type in the WPDE experimental test section is VGN (magmatic metamorphic gneiss, veined-gneiss), the same rock type can be assumed to persist along the full migration path. Based on the Task 9A description (P-17-18), the average mineralogical composition for the rock is as indicated in Figure A5-2.

Given that the volume fraction of a component mineral is a point sample averaged over a specified volume, this should be considered in the downscaling of the flowpath average to local values for variable matrix property cases. In this subtask the flowpath average mineralogical composition is arbitrarily assumed to correspond to the values indicated in Figure A5-2. Given that the rock matrix minerals are considered to be either micaceous (sorbing) or non-micaceous (effectively non-sorbing), the local volume fraction of mica, f_{mica} may be considered to be distributed with an expected value of 31.3 %. It is left up to the discretion of the modelling groups to choose how the local-scale heterogeneity is implemented in the modelling, although the average for the rock volume as a whole should be roughly 30 %. The average bulk density of the rock can be taken to be 2 741 kg/m^3 in accordance with the values reported by Kukkonen et al. (2011) for the VGN rock type.

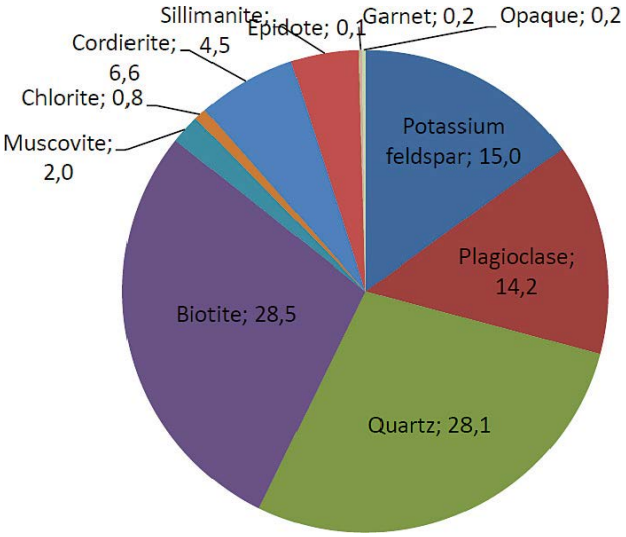

Figure A5-2. *Average mineralogical composition of veined gneiss samples (VGN) from the WPDE experimental section of ONK-PP323. Diagram reproduced from Ikonen et al. (2015).*

A5.2.3 Material properties of the rock matrix

Summary of material properties for transported solutes

The solute specific material properties for Task 9D1 are specified in Table A5-4 for the hypothetical solutes to be modelled in this subtask. The half-lives specified are for use in Task 9D1(b,d) and are arbitrary, although have been chosen in scoping calculations to impart good sensitivity of the solute recovery to the modelled transport retardation processes.

Table A5-4. Solute-specific material property parameters for use in Task 9D1(a–d).

solute	K_d (m^3/kg)	D_e (m^2/s)	$t_{½}$ (y)	λ (1/y)
A (non-sorbing)	0	5×10^{-15}	20	3.47×10^{-2}
B (weakly-sorbing)	10^{-4}	1.83×10^{-13}	10^{3}	6.93×10^{-4}
C (moderately-sorbing)	10^{-3}	1.83×10^{-13}	10^{4}	6.93×10^{-5}
D (strongly-sorbing)	0.1	1.83×10^{-13}	10^{6}	6.93×10^{-7}

Note: λ (1/y) is the radioactive decay constant given by the formula $\lambda = \ln(2)/t_{½}$

Sorption

For the Task 9D1(a–d) subtasks, four hypothetical solutes representing a broad range of differing sorptivities are to be modelled:

- Tracer A – non-sorbing ($K_d = 0$ m^3/kg)
- Tracer B – weakly sorbing ($K_d = 10^{-4}$ m^3/kg)
- Tracer C – moderately sorbing ($K_d = 10^{-3}$ m^3/kg)
- Tracer D – strongly sorbing ($K_d = 0.1$ m^3/kg)

For the purpose of these sub-tasks, a fixed groundwater/porewater composition can be assumed, although for the hypothetical tracers listed above this is of limited practical significance. If the groundwater composition is deemed to be static, the only source of K_d variability is due to the distribution of sorbing mineral phases in the rock matrix. Since sorption is a surface area mediated process, the spatial variation in K_d can be presumed to be roughly proportional to the spatial variability of reactive surface area. As discussed in Hakanen et al. (2014), the measured BET surface area of site-specific rocks at Olkiluoto is dominated by the presence of micaceous minerals (principally: biotite, chlorite, and muscovite) and therefore the K_d in the present work can be assumed to be proportional to the local mica content of the rock.

The K_d values given in the list above may be taken to represent an average value for the rock flanking the hypothetical flowpath described in previous sections (i.e. for 31.3 % average content of micaceous minerals). For Task 9D1c, the local K_d for the rock should be scaled according to the local volume fraction of mica in accordance with the assumptions outlined in the previous section. If the K_d for sorption is assumed to be roughly proportional to local mica content, we have:

$$\frac{K_d}{K_d^0} \approx \frac{\phi_{mica}}{\phi_{mica}^0} \tag{A5-5}$$

Where K_d^0 is the sorption partitioning coefficient of a given solute for the reference mica content f^0_{mica}, while f_{mica} is the local volume fraction of mica in the rock. In line with the guidance given in the previous section concerning the average mineralogy of the rock, the average K_d should be roughly equal to K_d^0 for the whole rock volume. The local K_d, however, can be assumed to vary in accordance with the specific model of mineralogical spatial heterogeneity adopted by individual modelling groups. Since the upper and lower bounds on local K_d variability is dependent on the representative elementary volume of rock under consideration and the underlying model of spatial heterogeneity, these cannot be specified a priori as part of the Task description. The maximum K_d in any given part of the matrix, however, should not exceed that for a 100 % mica volume fraction which is roughly 3 times the K_d^0 for the average reference mica content.

Porosity and Effective diffusivity

Porosities and effective diffusivities are given in the Task 9A description (P-17-18). For Task 9D1 the flowpath average porosity (water gravimetry based) and effective diffusivity is based on the average of values measured for the VGN rock type. From Table 2-8 in the Task 9A description (P-17-18), the average water gravimetric porosity is 0.65 % which for our synthetic safety assessment setting can be assumed to be a flowpath average. Similarly, from Table 2-9 in the same report, the average value of effective HTO diffusivity is calculated to be 1.83×10^{-13} m^2/s, while the corresponding value for Cl^- is 5.0×10^{-15} m^2/s.

In this subtask, the HTO effective diffusivity may be assumed to apply to all non-charged or cationic solutes (all sorbing solutes), while the Cl^- diffusivity can be assumed applicable to the non-sorbing solute which is presumed to be an anion. This implies an anion exclusion factor of 0.0273 (or, roughly 37 times reduced effective diffusivity for anions relative to non-charged, or cationic species). Enhanced diffusion of weakly sorbing cations due to concentration enrichment in the electrical double layer of micropores (EDL-diffusion) as well as multicomponent effects may be neglected in this subtask, although this choice is also left up to the individual modelling teams to decide. If multicomponent diffusivities are considered, the HTO effective diffusivity specified above may be considered representative for estimation of the bulk geometric formation factor of the rock.

As for sorption, specifics relating to how local variability in porosity and effective diffusivity is handled will be left up to the modelling teams to decide individually. It is acknowledged that the assignment of effective diffusivities based on through-diffusion measurements on drill core samples of finite (cm-scale) length may (or, may not) overestimate the true effective diffusivity due to different connectivity of the microporous network over different length scales. For this reason, it is proposed that each modelling group decides whether the effective diffusivity should represent an average for the whole rock volume, or for reference-scale samples where connectivity of the porous network may be greater when studied in a through-diffusion experiment.

A5.2.4 Source term for Task 9D1 Synthetic Safety Assessment calculations

It is proposed that the source term is relatively simplified in this exercise. The nuclide cocktail from the source is to be introduced in the flowing system as an extended pulse flux of 1 000 y duration in Task 9D1(a,c) and a constant flux release rate in Task 9D1(b,d). Radionuclide decay is to be omitted in subtasks (a) and (c), although is to be included in subtasks (b) and (d). The appropriate decay constants for the calculations are specified in Table A5-4.

Since the tracer solutes are hypothetical and are presumed to sorb linearly, the magnitude of the release is not important and can be set at an arbitrary level. For non-decay cases, 1 mol/y can be assumed, while for the decay cases, 1 MBq/y can be used. For the simulations including decay, results for far-field flux (recovery) should be made dimensionless by normalising relative to the source term activity flux. Results should not be decay corrected. For the non-decay cases, aqueous concentration fluxes should be normalised relative to the source term concentration flux.

A5.2.5 Requested performance measures for Task 9D1

The main performance measures envisaged for Task 9D1 are summary statistics for recovered solute at the end of the flow path as well as the breakthrough curves themselves. At a minimum, travel times associated with 5 %, 50 %, 95 % recovery fractions are requested for the non-decay, extended pulse boundary condition variant cases in Task 9D1(a,c).

A rock matrix diffusion profile (i.e. average pore concentration within the rock matrix including sorbed and dissolved fractions) is requested for each of the tracers at a distance exactly half-way along the flowpath at specific times corresponding to those given in Table A5-5. For the non-decay cases (a, c), the units should be mol/kg rock and Bq/kg rock for the decay cases (b, d). The requested times for the matrix diffusion profiles are arbitrary, although based on the expected transport time associated with a penetration depth of a few cm to dm into the rock matrix for each solute which should be sufficient to illustrate the most salient impacts of rock matrix heterogeneity on the uptake of solute into the rock matrix. For the constant flux cases (Task 9D1(b,d)) where decay is included, the far-field (breakthrough) flux should also be calculated at 100 ka.

Table A5-5. Breakthrough times for which a rock matrix diffusion profile is requested at a distance exactly half-way along the flowpath.

Solute	Profile time
A (non-sorbing)	500 y
B (weakly-sorbing)	5×10^3 y
C (moderately-sorbing)	5×10^4 y
D (strongly-sorbing)	5×10^5 y

In summary, the following performance measures are requested:

Task 9D1(a,c) – extended pulse flux boundary condition (no decay)

1) Breakthrough curves normalised with respect to the flux boundary condition (dimensionless);
2) Summary statistics of solute breakthrough (i.e. times associated with 5 %, 50 %, 95 % recovery fraction);
3) Rock matrix diffusion profiles (mol/kg rock, including sorbed and dissolved fractions) halfway along the flowpath and the times corresponding to those given in Table A5-5.

Task 9D1(b,d) – constant flux boundary condition (with decay)

1) Breakthrough curves normalised with respect to the flux boundary condition (dimensionless);
2) Rock matrix diffusion profiles (Bq/kg rock, including sorbed and dissolved fractions) halfway along the flowpath and the times corresponding to those given in Table A5-5;
3) Normalised solute breakthrough flux for all solutes at 100 ka (dimensionless).

A5.2.6 Concerning microstructural and material property variability of the rock matrix

In the first stage of Task 9D it is proposed that material properties along the flow path are the same as those sampled in drill hole ONK-PP323 although confined to the dominant rock type (VGN) encountered in the WPDE experimental section itself (interval 15–20 m). For Task 9D3 it is proposed that a more detailed geological variability is introduced consisting of the multiple rock types represented in the entire borehole, although fixed to the same overall proportions sampled in the borehole. In Task 9D4 it is proposed that proportions of different rock types are assigned from a probability distribution in accordance with the overall geological statistics of the Olkiluoto site. This will introduce additional variability that is of relevance for Safety Assessment modelling of individual migration paths from a repository. In a later stage, material properties representative of the rock volume in the LTDE-SD project or perhaps the Forsmark site might also be considered as a separate case study, although this will need to be decided at a later time.

Regarding material property variability along the flowpath and orthogonal to the flowpath (spanning the flowpath width and into the rock matrix), the following possibilities could be considered:

1) Constant average material properties assumed for entire flowpath;
2) Variable material properties along flowpath and within the rock matrix orthogonal to the flowpath;
3) Variable foliation (or, same for whole flowpath?);
4) Anisotropic effects possibly coupled with item (3);
5) Optional study – Upscaling of the detailed X-ray microtomography/C-14 PMMA data to larger scale. Can we preserve anything from the detailed data? For instance, is there any influence of the detailed porosity distribution, and the distribution of e.g. biotite on larger scale transport? Does it matter for SA?

For the purpose of the Task 9D1(a–d) it can be assumed that the porosities and matrix effective diffusivities given in Table 2-8 and Table 2-9 of the Task 9A description (P-17-18) for the VGN rock type are statistically representative samples of the rock distributed along the flowpath while the average mineralogical composition of the rock can be assumed to be the same as that given in Figure 2-11 of the same report. As noted in previous sections of this Task description, the K_d values for sorption of the hypothetical solutes may be considered proportional to the local mica content of the rock. It is left up the individual modelling teams to apply whatever statistical model of material property variation that they consider appropriate to describe the local state of the rock matrix. For the Task 9D1(a–d) case studies, the modellers can assume the absence of additional fracture coatings.

A5.3 Description of Task 9D2

The basic geometrical and physical conditions from Task 9D1 should be used as a starting point in Task 9D2. The main difference is the choice of nuclide cocktail and the source term which is described below.

A5.3.1 Hydrodynamic conditions for Task 9D2

The hydrodynamic conditions for Task 9D2 are the same as those for Task 9D1 as specified in Table A5-1.

A5.3.2 Material properties of the rock matrix specific to Task 9D2

The only substantial difference in the Task 9D2 subtask relative to Task 9D1 is the inclusion of radionuclides belonging to the radium series ($4n$+2) decay chain starting at U-238 as it occurs in nature. It is proposed that the straight chain of nuclides shown in Figure A5-3b is modelled in this subtask and the minor nuclides shown in Figure A5-3a are neglected.

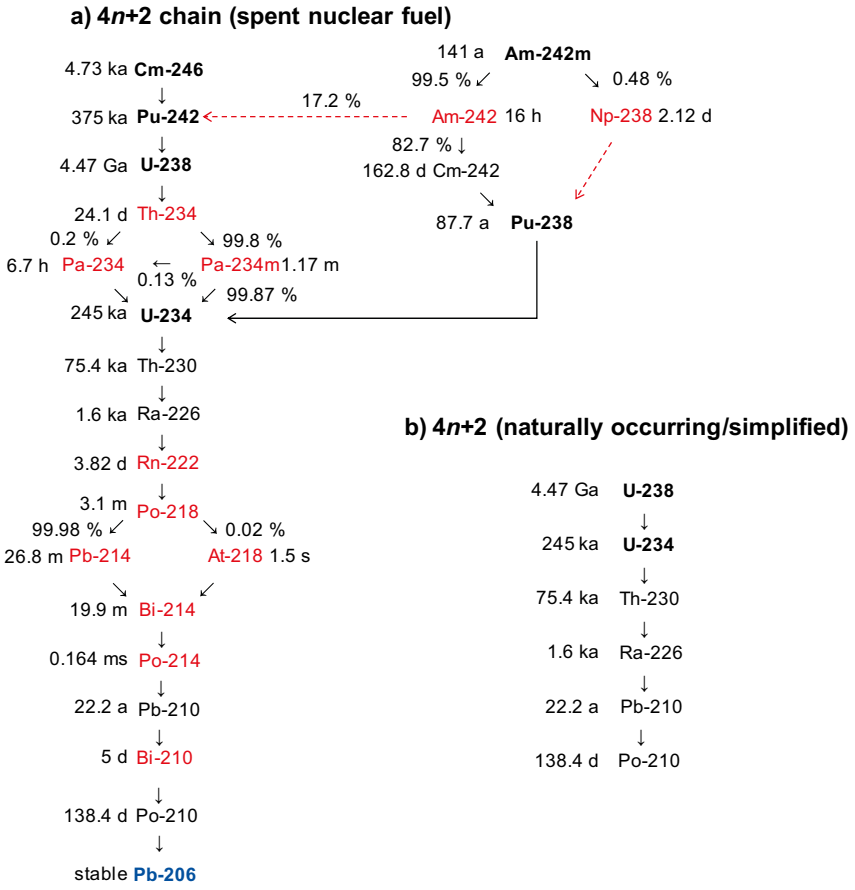

Figure A5-3. *The 4n+2 decay chain (radium series) as typical of a) spent nuclear fuel (all nuclides including minor daughters), and b) naturally occurring radionuclides belonging to the radium series (minor daughter nuclides omitted). Nuclides in bold-black text correspond to those typically specified in spent nuclear fuel inventories, while those in black non-bold text are formed by ingrowth and explicitly accounted for in transport calculations although do not typically appear in inventory specifications. Nuclides in red text have very short half-lives and do not need to be considered explicitly in transport calculations. Nuclides in blue are stable and thus not relevant for radiotoxicity calculations.*

Summary of material properties for transported solutes

The solute specific material properties for Task 9D2 are specified in Table A5-6 for the radium decay chain (4n+2) to be modelled in this subtask. Although the maximum penetration depth for both Pb-210 and Po-210 is likely to be no more than a few tenths of a mm in the rock matrix, the production of these nuclides is still interesting for understanding the systematics of isotope disequilibrium in the geosphere which is also dependent on the distribution of their parent nuclides in the rock matrix.

Table A5-6. Radioelement-specific material property parameters for use in Task 9D2. K_d values are assumed based on recommended data given in Hakanen et al. (2014) for Olkiluoto T-series mica gneiss in contact with brackish reducing, high-carbonate groundwater of designated OLBA type (Vuorinen and Snellman 1998).

Nuclide	Dominant species	K_d (m^3/kg)	D_e (m^2/s)	$t_{½}$ (y)
U-238	$Ca_2UO_2(CO_3)_3$	8.0×10^{-2}	1.83×10^{-13}	4.47×10^{9}
U-234	$Ca_2UO_2(CO_3)_3$	8.0×10^{-2}	1.83×10^{-13}	2.45×10^{5}
Th-230	$Th(OH)_2(CO_3)_2^{2-}$	8.0	5×10^{-15}	7.54×10^{4}
Ra-226	Ra^{2+}	6.0×10^{-2}	1.83×10^{-13}	1.6×10^{3}
Pb-210[(1)]	$PbCl^{+}$	2.0	1.83×10^{-13}	2.22×10^{1}
Po-210[(2)]	$PoO(OH)_2$	2.0	1.83×10^{-13}	3.79×10^{-1}

[(1)] Kd value for Pb assumes ~20 times higher Kd at pH 7.5 than nearest geochemical analogy (Ni).

[(2)] Kd value for Po assigned to achieve approximate Po-210/Pb-210 secular equilibrium.

Sorption

For the Task 9D2 calculations, a fixed groundwater/porewater composition can be assumed nominally corresponding to that given in Table 2-3 of the Task 9A description (P-17-18) and appropriate K_d values should be chosen which are consistent with this composition. Suggested K_d values for radium series members on the REPRO site specific rock and groundwater will be distributed as a data delivery at a later time, although as a first approximation the recommendation given by Hakanen et al. (2014) for Olkiluoto T-series mica gneiss (T-MGN) in contact with brackish reducing, high-carbonate water of OLBA type (carbonate-containing reducing brackish reference water as defined by Vuorinen and Snellman (1998)) can be preliminarily assumed for this exercise (see Table A5-6). For the purposes of Task 9D2, redox transitions of U and Po can be neglected as far as this relates to groundwater geochemical gradients since the groundwater composition is deemed to be spatially and temporally static along the flowpath. This, however, does not preclude the consideration of redox systematics when assigning bulk K_d values which might represent a mixed redox state for the specified groundwater chemistry.

As previously, the spatial variation in K_d can be presumed to be roughly proportional to the spatial variability of reactive surface area and thus proportional to the local mica content of the rock. The K_d values given in Table A5-6 may be taken to represent an average value for the rock flanking the hypothetical flowpath described in previous sections (i.e. for 31.3 % average content of micaceous minerals). For Task 9D2, the local K_d for the rock should be scaled according to the local volume fraction of mica as per Task 9D1(c–d). If the K_d for sorption is assumed to be roughly proportional to local mica content, we have:

$$\frac{K_d}{K_d^0} \approx \frac{\phi_{mica}}{\phi_{mica}^0} \tag{A5-6}$$

Where K_d^0 is the sorption partitioning coefficient for a given solute for the reference mica content f^0_{mica}, while f_{mica} is the local volume fraction of mica in the rock. In accordance with the guidance given in the previous section for the average mineralogy of the rock, the average K_d should be equal to K_d^0 for the whole rock volume. The local K_d, however, can be assumed to vary in accordance with the specific model of mineralogical spatial heterogeneity adopted by individual modelling groups. Since the upper and lower bounds on local K_d variability is dependent on the representative elementary volume of rock under consideration and the underlying model of spatial heterogeneity, these cannot be specified a priori as part of the Task description. As previously, the maximum K_d in any given part of the matrix should not exceed that for a 100 % mica volume fraction which is roughly 3 times the K_d^0 for the average reference mica content.

Porosity and Effective diffusivity

The same effective diffusivities can be assumed in Task 9D2 as in Task 9D1 where cations and uncharged solutes are assumed to have uniform effective diffusivity of 1.83×10^{-13} m^2/s and anions have a reduced effective diffusivity of 5×10^{-15} m^2/s due to anion exclusion effects. Enhanced diffusion of weakly sorbing cations due to up-concentration in the electrical double layer of micropores (EDL-diffusion) as well as multicomponent effects can be neglected in this subtask, although this choice is also left up to the individual modelling teams to decide. If multicomponent diffusivities are considered, the HTO effective diffusivity specified above may be considered representative for estimation of the bulk geometric formation factor of the rock.

As for sorption, specifics relating to how local variability in porosity and effective diffusivity is handled will be left up to the modelling teams to decide individually. The same caveats apply in this subtask as for Task 9D1.

A5.3.3 Source term for Task 9D2 Synthetic Safety Assessment calculations

In this subtask, the simulation should consider a decay chain. Here, the $4n+2$ decay chain starting with U-238 should be modelled as a constant release with zero flux specified for daughter nuclides (i.e. a constant flux boundary condition of 1 MBq/y).

A5.3.4 Requested performance measures for Task 9D2

For Task 9D2, the following performance measures are requested:

1) Breakthrough curves normalised with respect to the flux boundary condition (dimensionless);
2) Rock matrix diffusion profiles in units of Bq/kg rock (including sorbed and dissolved fractions) halfway along the flowpath at 100 ka.
3) Normalised solute breakthrough flux for all solutes at 100 ka (dimensionless).

Arkitektkopia AB, Bromma, 2022

SKB is responsible for managing spent nuclear fuel and radioactive waste produced by the Swedish nuclear power plants such that man and the environment are protected in the near and distant future.

skb.se